UNIVERSITÉ DE STRASBOURG

UNIVERSITE DE STRASBOURG

Institut De Physique et Chimie Des Matérieaux De Strasbourg (IPCMS)

THESE DE DOCTORAT

presenté par

Saqib Javaid

pour obtenir le titre de

Docteur en Physique

Domaine : Physique de la Matière Condensée

Magnetism and Electronic Structure at Hybrid Manganese-Phthalocyanine/Metal Interfaces

Jury :

Mébarek Alouani	*Directeur de thèse*
Eric Beaurepaire	*Directeur de thèse*
Ferdinand Evers	*Rapporteur externe*
Richard Mattana	*Examinateur externe*
Frithjof Nolting	*Rapporteur externe*
Jean Weiss	*Examinateur interne*

Acknowledgements

I have spent 3 pleasant years while working on my PhD thesis and it is high time i should thank those who have helped me accomplish this task.

It would be most appropriate to start with the directors of this thesis, Eric Beaurepaire and Mébarek Alouani. During the course of this thesis, they have always been available for the discussions and i have benefited greatly from their scientific insights and pedagogical skills. I equally appreciate them for their kind mannerism and human qualities. What i have learned from Eric and Méb is not just restricted to the confines of science! I also wish to thank members of my PhD defense Jury : Ferdinand Evers, Richard Mattana, Frithjof Nolting and Jean Weiss.

I am thankful to Martin Bowen and Samy Boukari for their help during the course of this thesis. Fabrice Sheurer, Loïc Joly, Wolfgang Weber, and Jean-Paul Kappler have also been helpful particularly during the synchrotron experiments. Their presence have contributed greatly in getting the reliable results from brief but tiresome synchrotron experiments. I would also like to thank the staff of SIM(at SLS), ID32 and ID08 (at ESRF) and CASSIOPEE (at Soliel) beamlines for their support during the experiments. In particular, Blanka Deftels (ID32) has been very helpful regarding the analysis of XSW data. I would like to acknowledge the technical support provided by Jacek Arabski (Purification of molecules) and Bernard Muller (mechanical workshop). I am thankful to my past and present colleagues in Mèb's group namely, Lamjed Debbichi, Yannick Dappe, Xi Chen, Ali Jaffar and Fatima Ibrahim. I appreciate the fruitful collaboration with Sébestian Lebègue (CRM2(CNRS), Nancy) regarding the van der Waals interactions. Calculations presented in this work are carried out at JADE-CINES in Montpelier and ENIAC in IPCMS. I wish to thank computer department for their technical support and Veronique Werhner (secretary DMONS) for taking care of the administrative matters.

Magnétisme et Structure Electronique des Interfaces Hybrides MnPc/Métal

Introduction

La spintronique organique est une discipline émergeante, dont l'objectif est d'utiliser les matériaux organiques pour véhiculer et contrôler le transport polarisé en spin [1]. Grace à son énorme potentiel d'applications technologiques, la spintronique organique est rapidement devenue un champ de recherche actif et a déjà produit des résultats majeurs [2]. Malgré ces succès, les mécanismes du transport polarisé en spin, au travers des semi-conducteurs organiques, ne sont pas encore entièrement compris. Néanmoins, un consensus émerge actuellement pour reconnaître le rôle clé joué par l'interface organique/ ferromagnétique dans le contrôle de l'injection de spin du matériau ferromagnétique vers l'espaceur organique [3, 4]. Grâce à ces nouvelles approches physiques, on peut considérer que l'interface organique/ ferromagnétique est un levier qui permet de moduler la réponse polarisée en spin des dispositifs de la spintronique [5]. Ainsi, la clé du futur développement de la spintronique organique réside dans la disponibilité d'interfaces organique/ ferromagnétique "ajustables", pour lesquelles le choix de matériaux organiques appropriés est critique. Dans ce contexte, la famille des molécules métal-phthalocyanines (MPc) constitue une candidate prometteuse, du fait que les molécules MPc offrent une grande stabilité thermique durant le dépôt, ainsi que la versatilité de leurs propriétés structurales, électroniques et magnétiques une fois déposées sur une surface métallique [6].

L'idée fondamentale de cette thèse qui combine théorie et expérience, est de promouvoir une compréhension détaillée des propriétés électroniques de l'interface entre la molécule Manganèse-phthalocyanine (MnPc) et un substrat ferromagnétique de cobalt fcc (Co(001)). Dans le but de comprendre l'influence du substrat magnétique sur les propriétés électroniques de MnPc, nous avons également étudié les interfaces entre le Cu(001) non magnétique et MnPc. Un des points principaux de ce travail concerne une étude détaillée du couplage magnétique entre la surface de cobalt et MnPc. Ce type de couplage a été aussi observé entre les métaux ferromagnétiques et les porphyrines, ce qui illustre la richesse de la physique des interfaces métal-organique/ferromagnétique [7, 8]. Dans cette thèse, nous nous intéresserons également à la polarisation en spin induite à l'interface MnPc/Co. En effet, cette polarisation d'interface peut fortement influencer l'injection de spin et le transport tunnel à travers un espaceur organique. Avant d'obtenir une description fiable des interactions d'interface, il convient tout d'abord de déterminer la distance entre la molécule et le substrat, ainsi que la position de la molécule sur le substrat [9]. L'effet des interactions faibles de van der Waals (vdW) sur l'adsorption de MnPc sur Co ou Cu constituent une part importante de ce travail.

Tous les calculs sont fondés sur la théorie de la densité fonctionnelle (DFT) implémentée dans le package "PWSCF" [10]. Le potentiel d'échange et corrélation est traité dans l'approximation du gradient généralisé (GGA) de type PBE [11]. La base des ondes planes est coupée à 30 Ry pour les énergies cinétiques et 300 Ry pour la densité de charge. Dans la mesure où nous nous intéressons à des molécules isolées sur une surface, la première zone de Brillouin n'a été échantillonnée qu'au point gamma. Les surfaces de Co(001) et Cu(001) sont modélisées en utilisant des super-cellules périodiques contenant trois plans atomiques de 8×8 atomes, séparés par une région vide. L'effet des interactions vdW est pris en compte en suivant l'approche dite GGA-D développée par Grimme [12].

D'un point de vue expérimental, des expériences de dichroïsme magnétique circulaire des RX ont été entreprises à SLS (Swiss Light Source) et l'ESRF afin de mettre en évidence le couplage magnétique. La polarisation de spin induite à l'interface MnPc/Co à été sondée en utilisant la photoémission résolue en spin sur le synchrotron Soleil. Des expériences d'ondes stationnaires des RX ont également été réalisées à l'ESRF afin

d'obtenir des informations quantitatives sur la géométrie d'adsorption de MnPc sur Cu(001).

Le manuscrit est organisé comme suit :

Le Chapitre 1 passe en revue les interactions d'interface dans les systèmes hybrides organique/ inorganique. En particulier nous discutons l'influence de la surface métallique sur le magnétisme et la structure électronique des molécules de phthalocyanines à la lumière des récents développements expérimentaux et théoriques.

Le Chapitre 2 introduit le formalisme de la DFT dans le cadre d'une approche de pseudo-potentiels d'ondes planes ; la méthode de la DFT-dispersion est également décrite, elle permet de prendre en compte les interactions de van der Waals dans le cadre de la DFT. Dans le chapitre 3, les techniques expérimentales utilisées dans ce travail (basées sur le rayonnement synchrotron) sont décrites, ainsi que les conditions expérimentales correspondantes.

Le chapitre 4 décrit les résultats obtenus concernant les liaisons chimiques et les propriétés magnétiques liées à l'interface hybride MnPc/métal. La description obtenue de l'adsorption de MnPc sur Co(001) ou Cu(001) provient à la fois des calculs DFT (GGA) et de la spectroscopie d'absorption des RX. Les propriétés magnétiques de l'interface MnPc/Co(001) sont ensuite discutées, plus particulièrement le couplage ferromagnétique entre MnPc et Co(001). Finalement, l'impact de l'hybridation entre le Co(001) et MnPc sur la polarisation de spin à l'interface est étudié.

Dans le chapitre 5, Les interactions de van der Waals sont incorporées dans la DFT (c'est le modèle GGA-D) ce qui permet de ré-examiner l'adsorption de MnPc sur Cu(001). Une optimisation de la géométrie est réalisée afin d'améliorer la description théorique. Nous étudions l'effet des interaction vdW sur les propriétés magnétiques et électroniques de MnPc sur Cu(001) et Co(001). La distance d'adsorption du MnPc est ensuite mesurée par XSW et comparée aux valeurs calculées par la méthode GGA-D.

Dans le chapitre 6, on s'intéresse aux propriétés magnétiques liées aux sites N et C de la molécule pour MnPc déposé sur Co(001). Par ailleurs, nous avons utilisé le dichroisme circulaire magnétique des RX pour étudier et discuter les propriétés magnétiques des sites d'azote. La thèse se termine par une conclusion générale et des perspectives.

Résultats

Les calculs DFT-GGA montrent que la molécule MnPc est adsorbée en position pont aussi bien sur Cu(001) que Co(001), mais les distances d'adsorption sont radicalement différentes. Dans le cas de MnPc sur Co la distance calculée est de 2.25 Å, comparée à 3.60 Å pour le Cu. Dans ce dernier cas, du fait de cette grande distance, le recouvrement des orbitales de MnPc et Cu est faible, si bien que les interactions chimiques d'interfaces sont beaucoup plus faibles que pour MnPc/Co. Cela est confirmé par une énergie d'adsorption calculée beaucoup plus grande dans le cas de MnPc/Co (2.2 eV) que MnPc/Cu (0.5 eV).

Afin de visualiser les interactions chimique à l'interface, nous avons calculé la densité de charge dans le plan (001) comme le montre la Fig. 1. Dans le cas de MnPc/Cu(001) (partie du haut), la liaison chimique est très faible puisque MnPc partage peu de charge avec les atomes de cuivre à l'interface. Par contre on observe pour l'interface MnPc/Co(001) que les contours de densité de charge se propagent depuis les atomes de surface de cobalt vers la molecule de MnPc. La présence de ces contours de densité de charge et de la localisation de charge aux interfaces est une indication claire de la présence d'une liaison covalente à l'interface MnPc/Co(001) qui est fortement réduite pour MnPc/Cu(001). Ainsi, à la fois les énergies d'adsorption calculées et la densité de charge d'interfaces, montrent que les interactions chimiques calculées sont beaucoup plus grandes dans le cas de MnPc/Co que dans le cas de MnPc/Cu. Nous concluons que MnPc est chimisorbée sur Co et physisorbée sur Cu.

Des expériences de XMCD aux seuils L du Mn et K de l'azote ont permis de sonder les interactions magnétiques d'interface. Les résultats présentés sur la Fig. 2 montrent des signaux XMCD clairs à la fois pour des monocouches de MnPc sur Co, et pour MnPc sur Cu. Néanmoins, le spectre de Mn/Cu a une structure fine provenant de multiplets, signature d'orbitales 3d localisées. Par contre, cette structure fine est passablement élargie dans le cas de MnPc/Co, ce que l'on attribue à l'hybridation des orbitales 3d de Mn et Co. Ce couplage magnétique d'interface est confirmé par les cycles d'hystérésis avec résolution chimique. Alors que le cycle du Mn pour Mn/Cu montre le comportement paramagnétique attendu, celui de MnPc/Co est carré et coïncide avec celui du Co. Cela
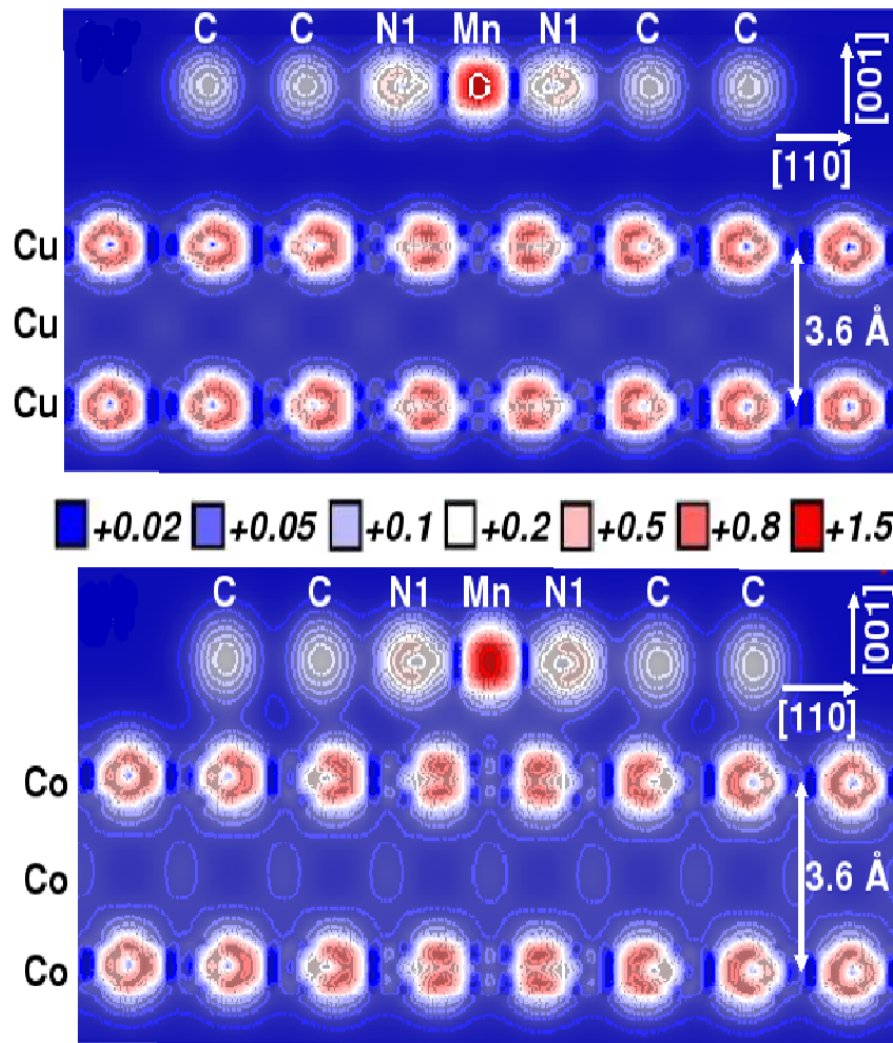
FIG. 1: Profil de densité de charge pour MnPc/Cu(001) (haut) et MnPc/Co(001) (bas), le long d'un plan (110) perpendiculaire au substrat.

démontre bien le couplage ferromagnétique entre Mn et Co.

Afin d'étudier l'impact de la liaison chimique entre MnPc et Co sur la polarisation de spin à l'interface, nous avons calculé la densité d'états locale (LDOS) au voisinage du niveau de Fermi, représenté sur la Fig. 3. Nous avons trouvé que l'hybridation diffère selon le canal de spin. Dans le cas du canal majoritaire, le Co s'hybride avec C, N, et Mn alors que pour le canal minoritaire (où la densité d'états est plus élevée d'un ordre de grandeur que le canal majoritaire), la contribution principale provient uniquement de Mn. A titre de comparaison, nous avons également étudié théoriquement H_2Pc/Co ;
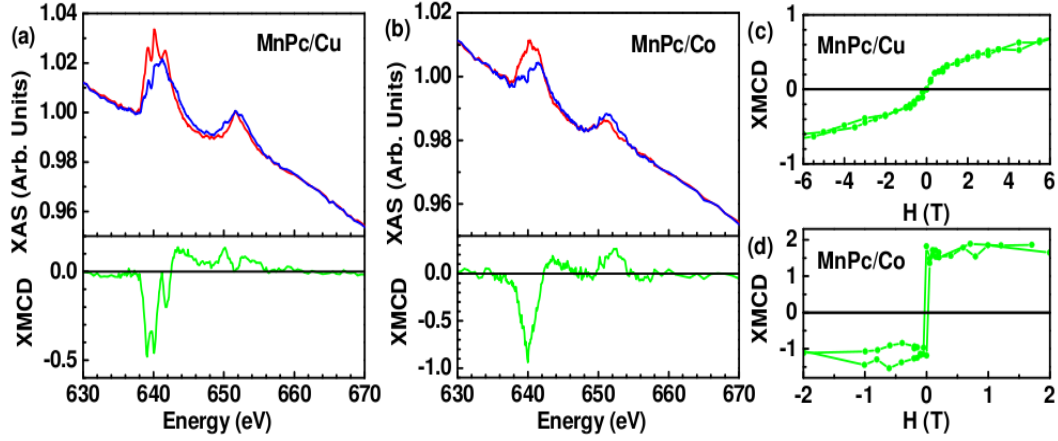
FIG. 2: Spectre XAS/XMCD pour a) 1ML MnPc/Cu(001) et b) 0.5 ML MnPc/Co(001). Les boucles hystérésis de Mn pour c) MnPc/Cu et d) MnPc/Co.

dans ce cas il y a peu d'hybridation dans le canal minoritaire et la polarisation de spin à l'interface est positive, comme anticipé. Par opposition, pour MnPc/Co il y a compétition entre les spins minoritaires (dominés par Mn) et les spins majoritaires (principalement C et N) pour définir le signe de la polarisation au niveau de Fermi. Il apparait donc clairement que la liaison chimique d'interface joue un rôle dominant pour déterminer le signe de la polarisation de spin au niveau de Fermi.

Cette polarisation de spin de l'interface ouvre une voie prometteuse pour la spintronique puisqu'elle permet d'améliorer les performances des dispositifs et de faciliter l'injection de spin dans un espaceur organique [13]. Afin d'obtenir une preuve spectroscopique confortant les densités d'états calculées (Fig. 3), nous avons réalisé des expériences de photoémission polarisées en spin pour MnPc/Co. Ces mesures montrent la très forte polarisation de spin des états électroniques et confirment que les interactions entre la molécule et le substrat induisent une polarisation de spin positive au voisinage du niveau de Fermi, localisée sur les sites N et C. Une preuve supplémentaire de ce mécanisme est apportée par des mesures de dichroïsme au seuil K de l'azote. Ce résultat montre que l'adsorption de MnPc sur Co induit une faible polarisation orbitale positive sur N, qui est absente pour MnPc/Cu.

Nous décrirons également comment l'interaction vdW influe sur les propriétés d'interface de MnPc/Co et MnPc/Cu. En plus de l'ajout d'une correction semi-empirique
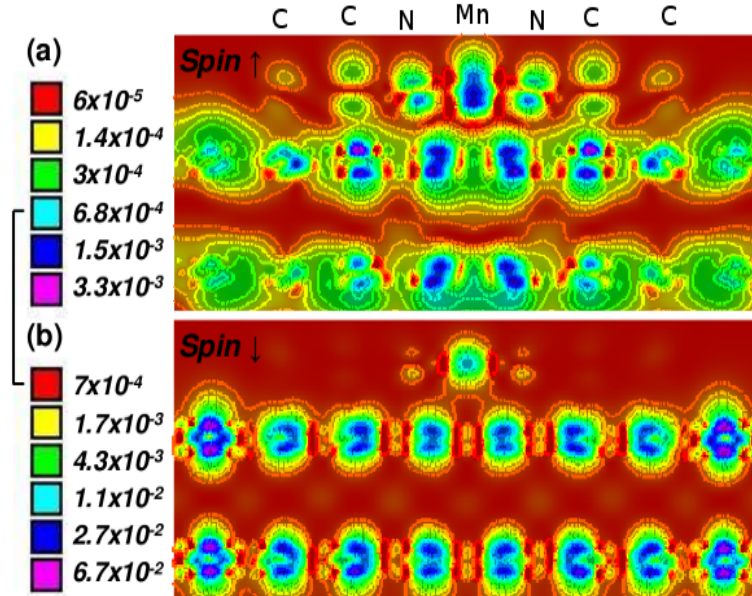
FIG. 3: Densité d' états locale de MnPc/Co pour a) spin up et b) spin down.

à l'énergie totale (méthode DFT-D), nous avons realisé l'optimisation de la géométrie (les forces de vdW sont inclues dans l'approche DFT-D) pour obtenir des positions atomiques optimisées. Lors de la relaxation, nous avons constaté que les atomes de la molécule ou du substrat qui étaient dans le même plan avant relaxation, se sont déplacés verticalement les uns par rapport aux autres. Nous définissons la distance verticale entre MnPc et le substrat comme la distance verticale entre l'atome du sommet du plan du surface du substrat et l'atom de Mn de la molécule. En suivant cette définition, nous trouvons pour les distances d'adsorption de MnPc sur Co(001) et Cu(001) respectivement ~ 1.9 Å et ~ 2.35 Å.

Fig. 4 représente le tracé de la densité de charge suivant le plan (011) (figure du haut) et la densité d'états partielle (PDOS) (figure du bas), calculées pour MnPc/Co(001) (Fig. 4a) et MnPc/Cu(001) (Fig. 4b). Le tracé de la densité de charge montre la forte hybridation chimique à l'interface MnPc/Co(001) ce qui est cohérent avec le calcul GGA. Ainsi, la PDOS de MnPc est fortement modifiée par l'hybridation avec les atoms de substrat Co du suite à l'adsorption. En particulier, la PDOS du Mn est fortement élargie comparée à celle d'une molécule isolée.

La densité de charge qui se propage de la surface de Cu à MnPc (Fig. 4b) indique

également la présence d'hybridation à l'interface MnPc/Cu(001). De façon similaire à MnPc/Co(001), la PDOS de Mn est élargie dans les deux canaux de spin si on compare à la molécule isolée de MnPc. Toutefois, la comparaison des contours de densité de charge de MnPc/Co(001) and MnPc/Cu(001) montre clairement que les interaction électronique à l'interface MnPc/Cu(001) sont beaucoup plus faibles que pour MnPc/Co(001). Par conséquent, la modification de structure électronique suite à l'adsorption est relativement plus faible pour MnPc/Cu(001) que pour MnPc/Co(001).

Ainsi, l'impact des interactions de vdW sur l'adsorption de MnPc sur Cu(001) ou Co(001) peut être résumé comme suit : la molécule MnPc qui était chimisorbée sur Co en GGA, ne montre pas de changements significatifs au regard de la distance d'adsorption ou de la structure électronique. Ceci s'explique par les fortes interactions chimiques à l'interface MnPc/Co qui seront peu modifiées par les forces faibles de dispersion de vdW. En revanche, les interactions vdW apportent un changement radical à l'adsorption de MnPc sur Cu. En effet, ces interactions réduisent la distance d'adsorption de 1 Å. Cette réduction de la distance fait que les orbitales de MnPc et Cu se recouvrent davantage, ce qui à pour effet d'augmenter l'hybridation à l'interface. La conséquence de l'ajout de l'interaction vdW change le mécanisme d'adsorption de MnPc sur Cu, de la physisorption à la chimisorption.

Nous avons réalisé des expériences de XSW pour déterminer la distance d'adsorption de MnPc sur Cu(001). La valeur expérimentale de la distance d'adsorption de MnPc est en bon accord avec la valeur calculée par l'approche GGA-D. De façon évidente l'approche GGA-D permet une bien meilleure description de l'adsorption de MnPc sur Cu(001) si on compare avec la méthode GGA. Ces résultats soulignent la nécessité d'inclure les interactions vdW dans les calculs ab initio, en particulier pour les systèmes (MnPc/Cu).
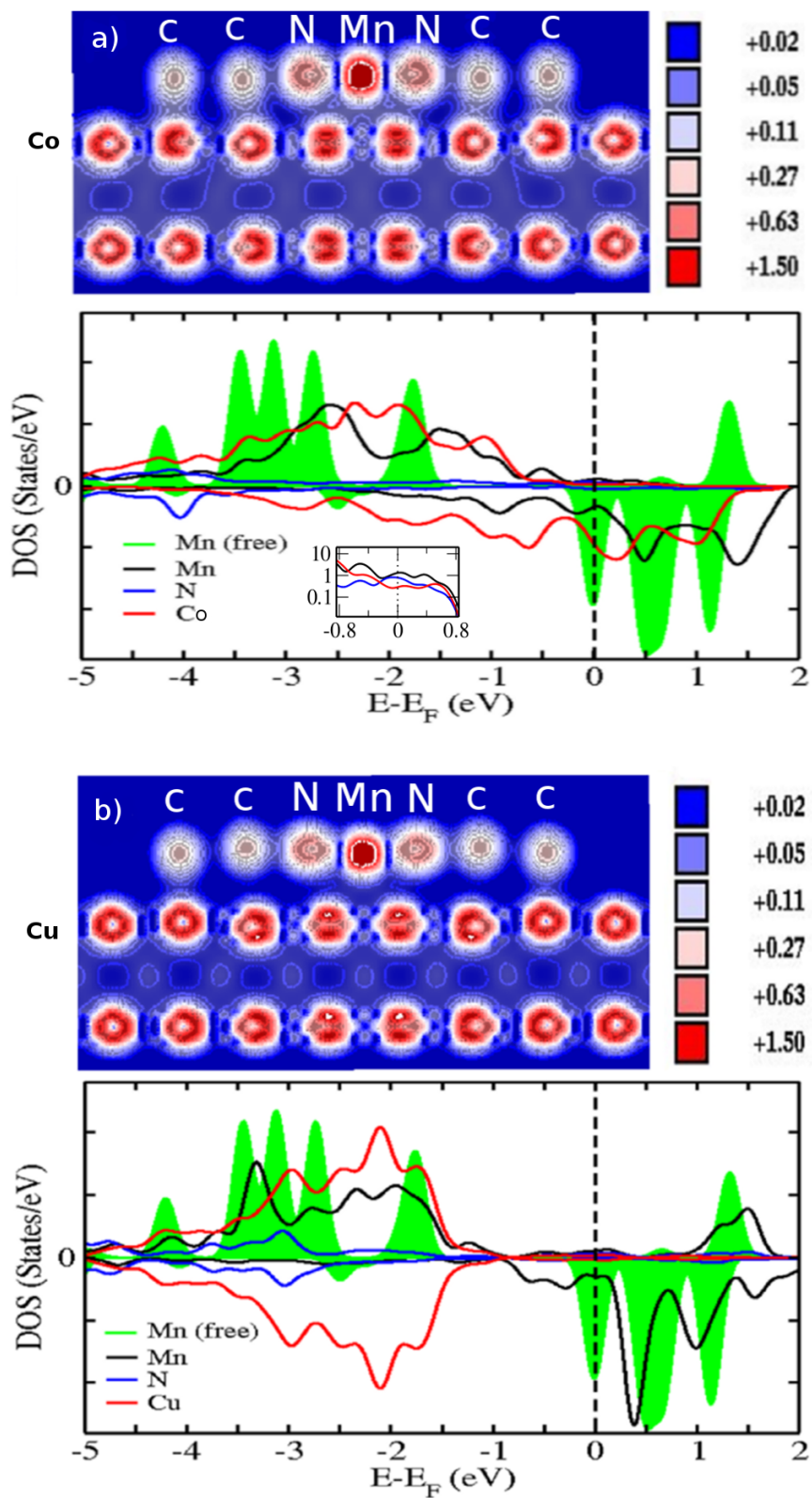
FIG. 4: Contour de densité de charge selon le plan (110) (haut) et PDOS de Mn, N et plan de cobalt de surface (bas) pour la structure relaxée obtenue par la méthode DFT-D pour (a) MnPc/Co(001) et (b) MnPc/Cu(001). La PDOS de Mn pour la molécule isolée est reportée pour comparaison.

Conclusions

Nous avons étudié le mécanisme d'adsorption de la molécule MnPc sur le Co(001) ou le Cu (001) et les interactions d'interface qui en découlent. Nos calculs GGA montrent que la molécule MnPc est chimisorbée sur Co ce qui conduit à de fortes interactions magnétiques à l'interface, notamment au couplage magnétique entre la molécule MnPc et le substrat de Co, et à une polarisation magnétique induite au niveau de Fermi sur les sites N et C. En raison de la chimisorption de MnPc sur Co, l'introduction des interactions faibles de vdW n'apporte aucun changement significatif à la structure électronique d'interface. Toutefois, dans le cadre d'un calcul GGA, on trouve que la molécule MnPc sur Cu est physisorbée en raison des interactions chimiques très faibles. Nos calculs montrent qu'à l'opposé de MnPc sur Co, les interactions vdW modifient fortement la structure électronique d'interface de MnPc/Cu. Cela conduit à un changement significatif du mécanisme d'adsorption de MnPc sur Cu (de la physisorption à une faible chimisorption). La valeur expérimentale de la distance d'adsorption de MnPc/Cu(001) déterminée par des expériences de XSW, est en bon accord avec celle déterminée par notre calcul GGA-D. Du point de vue de la spintronique, la polarisation de spin sur MnPc que nous avons calculé et mesurée, induite et modulée par des substrats ferromagnétiques souligne la pertinence des interfaces hybrides MPc/métal-ferromagnétique pour l'injection de spin et le transport de spins.

Bibliographie

[1] W. J. Naber, S. Faez, and W. G. van der Wiel. Organic spintronics. *J. Phys. D : Appl. Phys.*, 40 :R205–R228, 2007.

[2] V. A. Dediu, L. E. Hueso, I. Bergenti, and C. Taliani. Spin routes in oranic semiconductors. *Nat. Mater.*, 8 :707, 2009.

[3] S. Santivo. The rise of spinterface science. *Nat. Phys.*, 6 :562, 2010.

[4] P. Ruden. Interfaces are critical. *Nat. Phys.*, 10 :8, 2011.

[5] C. Barraud, P. Seneor, R. Mattana, S. Fusil, K. Bouzehouane, C. Deranlot, P. Graziosi, L. Hueso, I. Bergenti, V. Dediu, F. Petroff, and A. Fert. Unravelling the role of the interface for spin injection into organic semiconductors. *Nat. Phys.*, 6 :615, 2010.

[6] X. Chen and M. Alouani. Effect of metallic surfaces on the electronic structure, magnetism, and transport properties of Co-phthalocyanine molecules. *Phys. Rev. B*, 82 :094443, 2010.

[7] A. Scheybal, T. Ramsvik, R. Bertschinger, M. Putero, F. Nolting, and T.A. Jung. Induced magnetic ordering in a molecular monolayer. *Chem. Phys. Lett.*, 214 :411, 2005.

[8] H. Wende, M. Bernien, J. Luo, C. Sorg, N. Ponpandian, J. Kurde, J. Miguel, M. Piantek, X. Xu, Ph. Eckhold, W. Kuch, K. Baberschke, P. M. Panchmatia, B. Sanyal, P. M. Oppeneer, and O.Eriksson. Substrate-induced magnetic ordering and switching of iron porphyrin molecules. *Nat. Mater.*, 6 :516, 2007.

[9] N. Atodiresei, V. Caciuc, P. Lazic, and S. Blügel. Chemical versus van der Waals interaction : The role of the heteroatom in the flat absorption of aromatic molecules C_6H_6,C_5NH_5 , and $C_4N_2H_4$ on the Cu(110) surface. *Phys. Rev. Lett.*, 102 :136809, 2009.

[10] P. Gianozzi *et. al.* . QUANTUM ESPRESSO : a modular and open-source software project for quantum simulations of materials. *J. Phys. : Condens. Matt*, 21 :395502, 2009.

[11] John P. Perdew, Kieron Burke, and Matthias Ernzerhof. Generalized gradient approximation made simple. *Phys. Rev. Lett*, 77 :3865, 1996.

[12] S. Grimme. Semiempirical GGA-type density functional constructed with a long-range dispersion correction. *J. Comput. Chem.*, 27 :1787, 2006.

[13] Y. Zhan, E. Holmstrom, R. Lizarraga, O. Eriksson, X. Liu, E. Carlegrim F. Li, S. Stafstrom, and M. Fahlman. Efficient spin injection through exchange coupling at organic semiconductor/ferromagnet heterojunctions. *Adv. Mater.*, 22 :1626, 2009.

Contents

List of Figures

theoretical description of interfacial interactions, one should first determine the distance between the MPc molecule and the substrate as well as the position of the molecule on the substrate [9]. Therefore the effect of weak van der Waals (vdW) interactions on the adsorption of MnPc on Co(001) or Cu(001) constitutes an important part of this work.

All the calculations are based on density functional theory (DFT) as implemented in the PWSCF package [10]. For the exchange-correlation potential we used the generalized gradient approximation (GGA) in its PBE flavor [11]. A kinetic energy cutoff of 30 Ry (300 Ry for charge density) has been used for the plane-wave basis set. Because the aim is to study a single molecule on metallic surfaces we used only the gamma point to sample the first Brillouin zone. The surfaces of Co(001) and Cu(001) have been modeled by using periodic supercells of three atomic layers of (8×8) atoms separated by a vacuum region. The effect of vdW interactions has been taken into account by following GGA-D approach (in DFT-D2 version) developed by Grimme [12].

For the experimental work, mainly synchrotron radiation techniques have been used. To find magnetic coupling at MnPc/Co interface, x-ray magnetic circular dichroism (XMCD) spectroscopy has been performed at SLS and ESRF synchrotron facilities. Induced spin polarization at MnPc/Co interface has been probed by spin-polarized photoemission experiments carried out at Soleil synchrotron source. X-ray standing waves (XSW) experiments have been performed at ESRF to determine the adsorption distance of MnPc on Cu(001).

This manuscript is organized as follows. Chapter 1 provides an overview of organic/metal hybrid interfacial interactions. In particular, we discuss the impact of the metallic surfaces on the magnetism and the electronic structure of phthalocyanine molecules in the light of the recent experimental and theoretical results. Chapter 2 introduces the formalism of DFT within the framework of plane wave pseudopotential approach and also describes the DFT-dispersion (DFT-D) method which includes the vdW interactions within DFT. Chapter 3 provides a basic introduction to the experimental (synchrotron) technique used in this work along with an account of the conditions in which the experimental measurements were performed.

Chapter 4 describes the chemical and magnetic properties of hybrid MnPc/metal Interfaces. The adsorption of MnPc on Co(001) or Cu(001) is described through DFT (GGA) calculations and x-ray absorption spectroscopy. Then the magnetic properties at MnPc/Co(001) interface are discussed, namely the ferromagnetic coupling between MnPc and Co(001). Finally, the impact of hybridization between Co(001) and MnPc

on the interfacial spin polarization is studied. Chapter 5 includes the vdW interactions within DFT (i.e. GGA-D method) and re-examines the adsorption of MnPc on Cu(001) or Co(001). To improve the theoretical description further, the geometry optimization is performed. The effect of the vdW interactions on the electronic and magnetic properties of MnPc/Cu(001) and MnPc/Co(001) interfaces is studied. The adsorption distance of MnPc is determined by XSW experiments and compared to that calculated using GGA-D approach. Chapter 6 deals with the magnetic properties of N and C atoms (i.e. Pc ring) of MnPc on Co(001) surface. The spin polarization at MnPc/Co(001) interface is studied by spin-resolved photoemission experiments. Then the magnetic properties of N sites, probed by N K-edge XMCD experiments are discussed. The thesis ends with a general conclusion and perspectives.

Chapter 1

Mn(II)-Phthalocyanine/Metal Interface

This chapter provides the conceptual background regarding the main objectives of this thesis, i.e., understanding the physics of Mn(II)-phthalocyanine/metal interface. Such interfaces are expected to play an important role in the spin polarized transport across organic spacer in an organic spintronics device. The organization of this chapter is as follows. In section 1.1 we review the fundamental concepts of spintronics and also discuss the advantages of using organic materials as spacers, i.e., organic spintronics. For the general discussion, we have chosen a molecule from the metal(II)-phthalocyanine family i.e. Mn(II)-phthalocyanine (MnPc). In Section 1.2 we describe the fundamental electronic and mangetic properties of phthalocyanine molecules. In section 1.3 we provide an overview of organic/metal interfacial interactions and their impact on the spin transport. In section 1.4 we discuss the impact of metallic substrates on the structural, electronic and magnetic porperties of phthalocyanine molecules in the light of recent experimental and theoretical results. Finaly, in section 1.5 we present the motivation of this thesis.

1.1 Spintronics

1.1.1 Fundamental concepts

Spintronics is a field of research in which the electron spin instead of its charge is used to encode information in electronic devices. The concept of magnetoresistance (MR) lies at the heart of a spintronics device. We focus here on the spin-polarized transport across a given material (hereafter called a spacer). Depending upon the transport

mechanism across this spacer, the magnetoresistance can be divided into two types, namely giant magnetoresistance (GMR) and tunneling magnetoresistance (TMR). In this section, we explain the physical mechanisms associated with GMR and TMR.

1.1.1.1   Giant magnetoresistance

We provide here a brief, qualitative discussion on the concept of giant magnetoresistance. For additional information, the reader may refer to the review of Zutic and coworkers [13]. The Physical mechanisms associated with GMR may be explained in terms of the two-current model [14]. In a ferromagnet, bands are split due to exchange interactions, such that there is a spin asymmetry of the density of states (DOS) and of the Fermi velocities at the Fermi level E_F. Due to this asymmetry, spin up electrons don't experience the same resistance as spin down electrons within a ferromagnet. It is in this sense that we may consider different transport channels for spin up and spin down electrons.
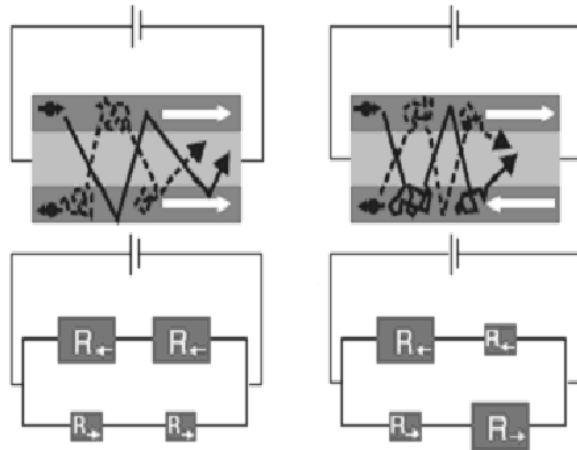
Figure 1.1: Schematic of a GMR device. Dark grey represents ferromagnets while light grey represents the metallic spacer. When the magnetization of both electrodes is parallel (top left), the resistivity of spin up channel (solid line) is smaller than that of spin down channel (dashed line). For the antiparallel configuration of the electrodes (top right), the resistivity of both spin channels is higher. Thus the overall resistance of the parallel configuration is lower (bottom left) than that of the antiparallel configuration (bottom right) as schematized by a resistor model in the bottom half (taken from [1]).

Fig. 1.1 shows schematically the GMR device mechanism, which comprises two ferromagnetic layers separated by a metallic spacer layer with a thickness between 1 and up to 4 nm. At the top half of the figure, the spin transport of electrons through a GMR device is shown. Dark grey represents the ferromagnetic electrodes while light grey represents the metallic spacer. The electrons with spin up are weakly scattered as

compared to those with spin down. Hence when the magnetizations of the electrodes are parallel, the resistivity for the spin up channel is smaller than that of spin down channel, resulting in an overall low resistance. However, if both magnetizations are antiparallel, both spin channels experience considerable scattering since each channel is comprised (in the local spin frame) of a spin down segment with a large resistance, resulting in an increase of the device resistance. The bottom half of Fig. 1.1 represents an equivalent resistor model that describes phenomenologically the GMR effect.

1.1.1.2   Tunnel magnetoresistance

In a TMR device, an ultrathin insulating layer (up to 3nm thick) is used as a spacer. In the absence of states in the energy gap (due to impurities, defects, etc.), transport occurs through elastic tunnelling. This process is schematically shown in Fig. 1.2.
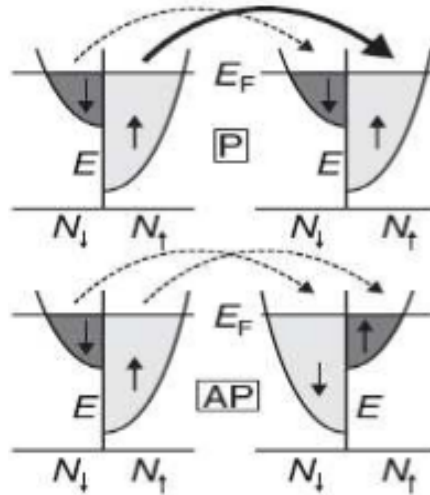
Figure 1.2: Spin-polarized tunnelling process in a TMR device. The solid (dashed) arrow represents high (low) spin current (taken from [1]).

The tunnelling rate depends qualitatively on the electrode DOS at the Fermi level (E_F), as well as on a tunnelling transmission matrix that reflects the band structure conjunction of the ferromagnet with the tunnel barrier. If we assume spin conservation during the electron tunnelling process, the tunnelling rate between identical electrodes is greater in the case of the parallel magnetization alignment of the two electrodes (shown in the top part of Fig. 1.2) as compared to the antiparallel alignment (shown at the bottom part). According to the Jullière model [15], the resulting TMR may be

expressed as:

$$TMR = \frac{2P_1P_2}{1 - P_1P_2} \,, \tag{1.1}$$

where P_i (i=1,2) are the spin polarization (SP) of the electrodes and are given by

$$P_i = \frac{\rho_i^{\uparrow}(E_f) - \rho_i^{\downarrow}(E_f)}{\rho_i^{\uparrow}(E_f) + \rho_i^{\downarrow}(E_f)} \,, \tag{1.2}$$

where $\rho_i^{\uparrow(\downarrow)}(E_F)$ represent the spin up(down) density of states at E_F of the electrode i.

1.1.2 Organic spintronics

We have just seen that the nature of spin polarized transport depends strongly on the type of spacer used, namely GMR and TMR for metallic and insulating spacers respectively. A recent trend is to use organic materials as spacers in spintronics devices, a field of research known as organic spintronics.

Organic materials possess properties such as the chemical tuning of electronic functionality, self-assembly and the mechanical flexibility [1]. These desirable properties have been exploited in conventional electronics, (i.e. organic/molecular electronics) which is already an active field of research. From the point of view of spin electronics, organic spacers are attractive due to the low atomic number of their constituent elements, which reduces considerably the amplitude of spin-orbit coupling in possible spin decoherence mechanisms. Thus organic spintronics may be seen as the fusion of organic electronics and spintronics.

Despite being a relatively new field of research, there are already some encouraging experimental results (see reviews [1, 2]). Even though, the physical mechanism behind spin polarized transport across organic semiconductors is not very well understood, a consensus is beginning to emerge that organic/ferromagnetic interfaces play a crucial role in controlling the spin injection from ferromagnet to organic spacers [3]. The interaction of an organic molecule with a metallic substrate and its possible impact on electronic and spin transport will be discussed in section 1.3.

1.2 Phthalocyanine molecules

Phthalocyanine molecules have received considerable attention due to their potential use for industrial applications [16]. These molecules are represented by the abbreviation "MPc" where "M" stands for the metal(II) site of the molecule (or H_2 in case of metal free Phthalocyanine) and $Pc=C_{32}H_{16}N_8$. MPc molecules are square planar with d_{4h}

symmetry (with the exception of PbPc and SnPc) as shown in Fig. 1.3.
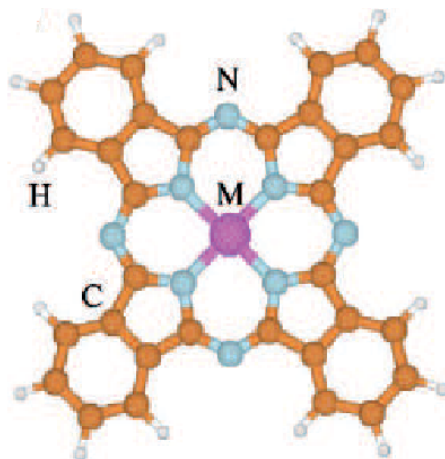
Figure 1.3: MPc molecule

MPc can be grown in the form of well ordered thin films having two structural phases, i.e., α and β [18]. The difference between these two phases is the stacking angle between MPc molecules along the b axis which is 65° and 45° for α and β phase respectively as shown in the Fig. 1.4. The presence of a given phase strongly depends on the temperature of the substrate. It has been shown that MPc films grow in the α phase when the substrate is at room temperature and in the β phase when the substrate is at temperature higher than 200° C. A phase transition from α to β phase can be obtained by the process of annealing [18].

The recent drive towards nanotechnology has brought the spotlight onto the electric properties of MPc. Indeed, they are now considered to be the prototype organic semi-conductors with potential nanoscale applications such as field effect transistors, light emitting diodes or single-molecule devices [19]. Ordered growth of MPc thin films and their thermal stability during deposition provide an additional advantage over other molecular systems. From spintronics perspective, MPc is made of low atomic number atoms (C, N, H) which reduces considerably the spin-orbit coupling. Furthermore, the possibility of substituting various elements in the central molecular site provides an additional way of controlling atomic number and thus spin-orbit coupling. Finally, the presence of localized spin at the central molecular site may lead to applications such as spin filtering [20] and quantum computing [21].
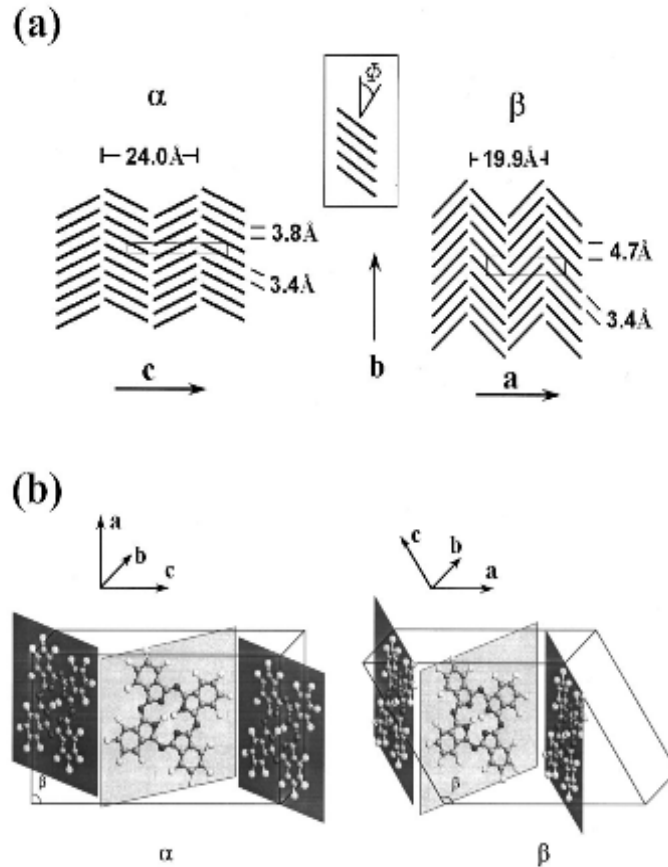
Figure 1.4: a) The stacking of H_2Pc molecules along the b-axis of monoclinic α (left) and β (right) phases. The stacking angle for α and β phases are 65° and 45° respectively. b) schematic of the unit cells of α and β configuration. MPc molecules grow in α phase at room temperature. β phase is obtaind when the substrate temperature is higher than 200° or by annealing the α phase crystal (taken from [17]).

1.2.1   Electronic structure of MPc

In order to understand the interfacial interactions between MPc and the substrate and charge transport through these molecules, it is necessary to understand the arrangement of the outer molecular orbitals. Since MPc has d_{4h} symmetry, the 3d orbitals of the central molecular site are represented according to d_{4h} point-group representations, i.e., $b_{1g}(d_{x^2-y^2})$, $a_{1g}(d_{z^2})$, $b_{2g}(d_{xy})$ and $e_g(d_{xz,yz})$.

Fig. 1.5 describes the outer orbital arrangements of various MPc calculated by DFT [16]. Here we briefly summarize the results. Generally, $a_{1u}(\pi)$ and $2e_g(\pi^*)$ orbitals are the highest occupied molecular orbital (HOMO) and the lowest unoccupied molecular orbital (LUMO) respectively, for Pc ring. As for a MPc molecule, the location and
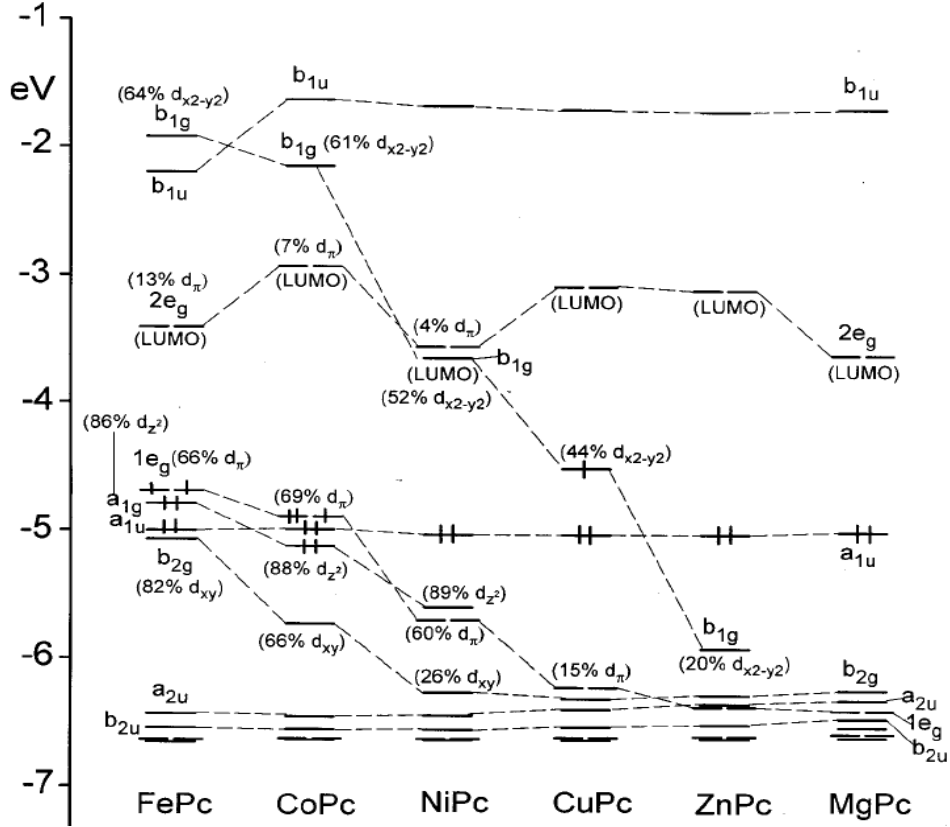
Figure 1.5: Orbital energy levels of various phthalocyanine molecules. For FePc and CoPc, the HOMO has strong d character. From NiPc to ZnPc, the d orbitals are lowered in energy so that HOMO is determined by Pc (a_{1u} orbital). The LUMO is dominated by Pc contribution ($2e_g$ orbital) (taken from [16]).

the nature of the HOMO and the LUMO are very sensitive to the central molecular site. For Fe and Co, the HOMO is primarily consituted of d_π orbitals, i.e., with e_g symmetry and the LUMO has the same character as that of Pc ring, namely $2e_g$. The situation changes as one substitutes metals with higher atomic number. In this case, the HOMO is determined by Pc ring, i.e., the a_{1u} and the 3d orbitals are pushed below considerably as compared to the a_{1u} orbital.

In the case of MnPc (with Mn 3d^5 configuration), similar molecular orbital arrangements are found as that of FePc and CoPc. Fig. 1.6 shows the total DOS of MnPc with contributions from Mn shown in the shaded area [19]. In the spin up channel, the HOMO and LUMO are a_{1u} and $2e_g$ orbitals respectively, coming from Pc ring. However for the spin down channel, the HOMO and LUMO consist of almost degenerate e_g orbitals. The a_{1g} and b_{2g} orbitals are partially filled (mainly in spin up channel) whereas b_{1g} is completely empty in both spin channels. This imbalance of occupation

in the two spin channels gives rise to a net magnetic moment of 3.0 μ_B for MnPc.
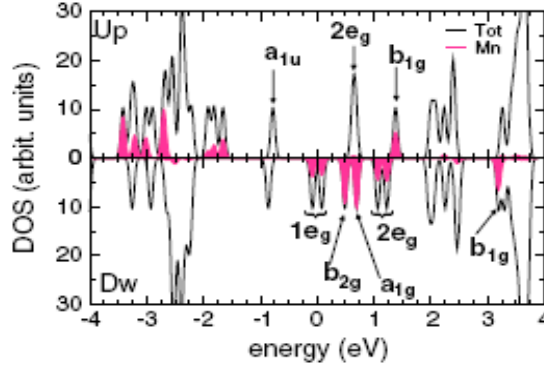
Figure 1.6: Calculated density of states for free MnPc molecule within the generalized gradient approxiation (GGA). The shaded area represents the Mn 3d contributions. In the spin-up channel, the HOMO and LUMO are a_{1u} and $2e_g$ orbitals respectively, coming from Pc ring. For the spin-down channel, the HOMO and LUMO consist of almost degenerate e_g orbitals. The Mn d orbitals are presented in d_{4h} representations i.e. $b_{1g}(d_{x^2-y^2})$, $a_{1g}(d_{z^2})$, $b_{2g}(d_{xy})$ and $e_g(d_{xz,yz})$ (taken from [19]).

1.2.2   Magnetic properties of MPc

Organic crystals of MPc molecules may have magnetic order due to the presence of a transition metal atom (Mn, Co, Fe) at the center of the molecule. Typically magnetic interactions arise due to interactions of MPc molecules within stacks along the b axis shown in Fig. 1.4. Since the distance between the molecules within a stack is more than 3 Å, superexchange interactions are responsible for the magnetism in the MPc crystals. Magnetic interactions could change from ferromagnetic to antiferromagnetic (and vice versa) depending upon the overlap of the orbitals involved in the superexchange interactions. MnPc has been studied widely for its magnetism and here we summarize its magnetic properties as a representative case.

MnPc crystal in its β phase is intrinsically ferromagnetic with intermediate spin state S= 3/2 [22]. The origin of this ferromagnetism can be explained with the help of Fig. 1.7, where the stacking arrangement of MnPc molecules along the b-axis in the β phase is shown. Mn atoms within a stack are placed right above or below a N atom of the adjacent parallel MnPc molecules [22]. This allows for weak ferromagnetic interactions mediated by π orbitals of the Pc ring. For example, a_{1g}–a_{1g} interactions mediated by Pc e_g orbital would lead to weak ferromagnetic interactions [23]. Consequently the Curie temperature of MnPc is very low (8.6 K).

Evidently, the sensitivity of the magnetic order in MPc crystals on the stacking
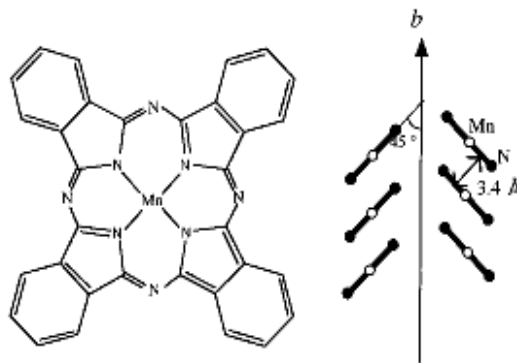
Figure 1.7: Structure of MnPc molecule (left) and its stacking along b-axis in β phase (right). Mn atom within stack lies directly above or below N atoms thus promoting superexchange ferromagnetic interactions between Mn atoms of adjacent molecules mediated by π orbitals of the Pc (taken from [22]).

angle of the molecules could be exploited to tailer magnetic interactions. For example it has been shown that a change of the substrate or templating could lead to a change of the stacking angle [21, 22]. As a consequence, the magnetic interactions are changed from ferromagnetic to anti-ferromagnetic.

1.3   Hybrid organic/metal interfacial interactions

1.3.1   Overview

We review here the adsorption of organic molecules on metallic surfaces and ensuing interfacial interactions. The main focus of the discussion will be ultrathin film adsorption on metallic surfaces that is relevant to this work.

Adsorption of organic molecules on metallic substrates is divided into two types according to the nature of interactions at the interface [24]. The adsorbate is said to be physisorbed in the case where there is almost no chemical interaction (such as chemical bonding) at the organic/metal interface. Thus weak van der Waals forces are responsible for the molecular adsorption. In this case, there is no change in the electronic structure of organic molecules, and thus the properties of a molecule on surface are similar to that of a free molecule. In contrast, if chemical interactions are responsible for molecular adsorption, the molecule is said to be chemisorbed. In the case of chemisorption (both in plane and out of plane) orbitals of adsorbing molecules can be strongly modified and the chemical properties of the molecule on a surface are very different from those of the free molecule. Strong chemical interactions may even

lead to the distortion of the molecular geometry.

As the molecule comes into contact with the substrate, interfacial vacuum level alignment takes place, i.e., surface vacuum levels at the interface are the same for the metal and the adsorbing molecules (Fig .1.8a) [25]. This alignment is further modified in the case where the adsorption of molecules leads to the formation of an interfacial dipolar layer (Fig .1.8b). This interface dipole impacts the metallic substrate by changing its work function. Crucial from the view point of charge transport, the magnitude of charge injection barrier can increase or decrease depending upon the direction and magnitude of the interface dipole. For example, a net charge transfer from the adsorbate to the metal surface would create a negative interface dipole (i.e. accumulation of positive (negative) charge on molecule(metal)) and consequently barrier for electron injection from the metal to the organic layer would also be reduced. This scenario is schematically depicted in Fig. 1.8 where the creation of a negative dipole shifts the vacuum level (VL) at the interface by Δ leading to the reduction of electron injection barrier (ϕ_B^n)
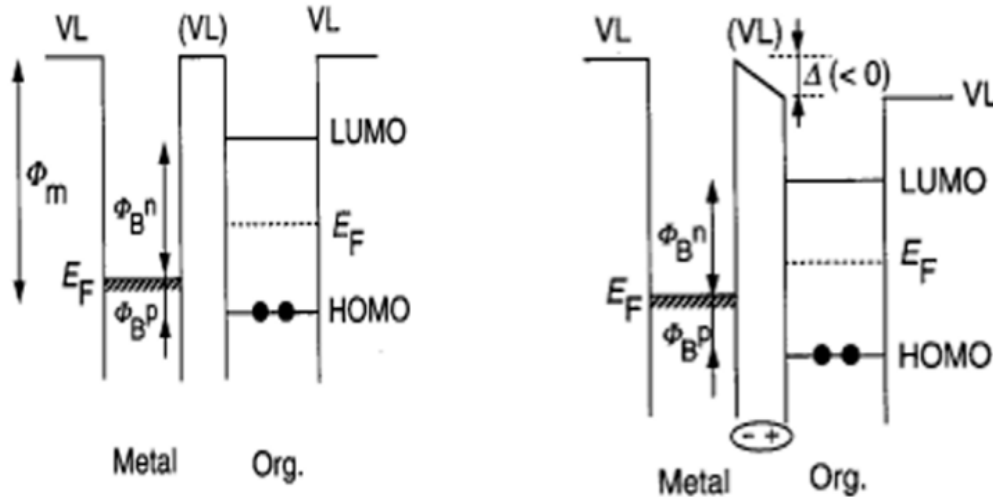
Figure 1.8: Interfacial energy diagram representing the vacuum level (VL) alignment without (left) and with (right) dipolar layer at organic/metal interface. The interface dipole shift the vaccuum level by Δ . Φ_m is the metal workfunction and ϕ_B^n and ϕ_B^P are the electron and the hole injection barriers respectively (taken from [25]).

Intuitively, the origin of the dipolar layer can be attributed to charge transfer at the interface. However, it has been found that charge transfer is not the only source of the interface dipole. For example, chemical bonding between adsorbate and substrate may also induce an interface dipole [26]. There are also purely physical mechanisms

that could account for the creation of electrical dipole at the interface. For example, it has been shown that Pauli repulsion between orbitals of adsorbate molecule and underlying metal can push back spilled out electrons of metallic surface [27]. This effect is equivalent to the creation of an interface dipole directed towards the vacuum which reduces the work function of the metal. Push-back effect has been shown to be present also for organic adsorbates [28, 29]. Image forces are also known to create an interface dipole at organic/metal interface reducing the barrier height [30].

For a thick organic layer, band bending can also take place so that the organic layer and metal have a common chemical potential [25]. However this is only possible if the organic layer has sufficient mobile carriers. Consequently, bands are flat for ultrathin organic films.

1.3.2   Organic/ferromagnetic interface

The description of interfacial interactions just discussed is also valid in the case where the metallic substrate is ferromagnetic. However, there is an additional magnetic interaction between the ferromagnetic substrate and the adsorbing molecules.

The impact of magnetic interactions at organic/ferromagnetic interface is most telling in the case of metal-organic adsorbate. It has been shown that the transition metal porphyrin molecules ferromagnetically couple to ferromagnetic substrates [7, 8]. The experimental evidence of this magnetic coupling is summarized in Fig. 1.9. Manganese(III)tetra-phenylporphyrin chloride (MnTPPCl) is a paramagnetic metal-organic molecule. However, on ferromagnetic Co/Al(111) substrate, Mn site in MnTP-PCl becomes ferromagnetic as indicated by the x-ray magnetic circular dichrosim (XMCD) spectra in Fig. 1.9b, with its magnetization in the same direction as that of Co surface (Fig. 1.9a). Finally, the hysteresis loops of Co and Mn coincide nicely (Fig. 1.9 c,d) indicating that Mn spin switches in the same way as the spin of Co film thus confirming the ferromagnetic coupling between MnTPPCl and the ferromagnetic substrate. Later experiments revealed that similar interfacial magnetic coupling also exists for Fe-octaethylporphyrin (OEP) and Ni surface [8]. This magnetic coupling was attributed to the superexchange interactions between Ni and Fe 3d orbitals mediated by N sites of Fe OEP as the distance between the Fe OEP molecule and substrate was too large for the direct exchange.

Magnetic substrate can also impact non-magnetic atoms of the adsorbate. For example it was found that substrate Fe atoms induces spin polarization on π-conjugated orbitals of Alq$_3$ molecules which are otherwise non-magnetic [31]. Conversely, spin-polarization can be induced on organic adsorbate even with non-magnetic substrates.
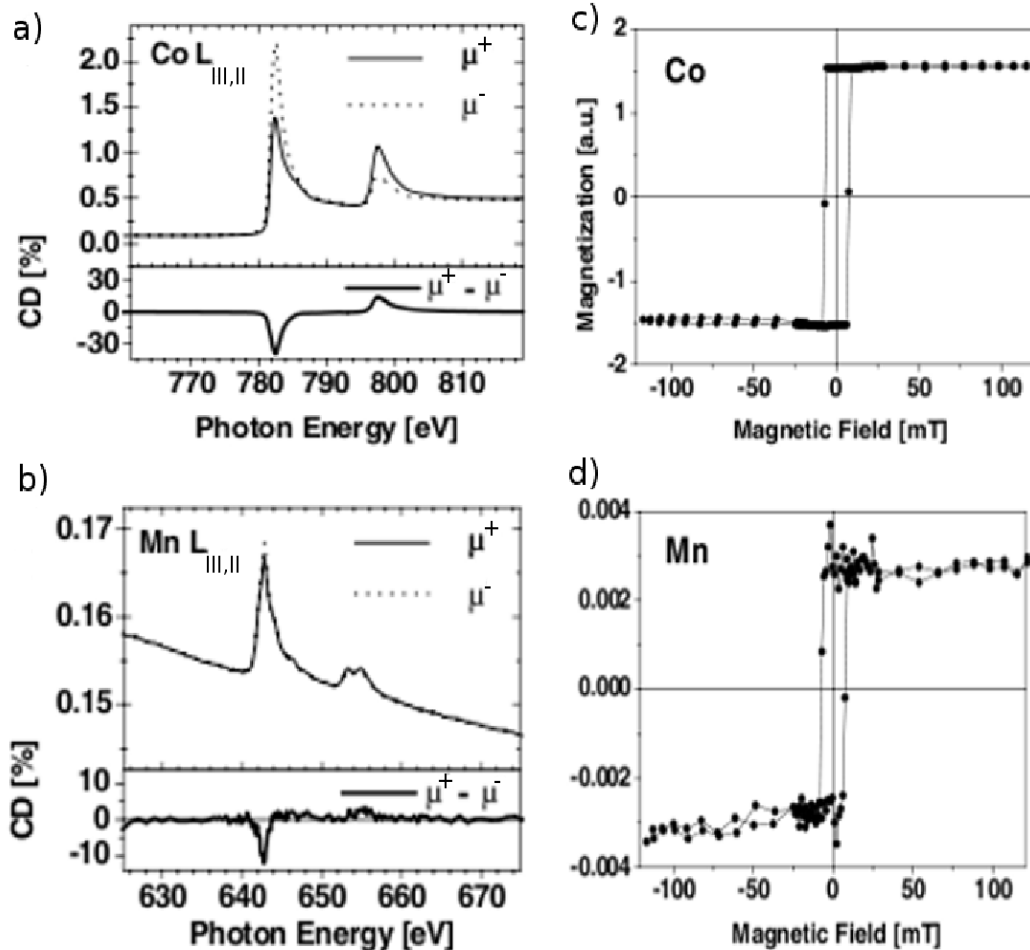
Figure 1.9: Magnetic coupling at MnTPPCl/Co/Au(111) interface. L-edge XAS and XMCD spectra of a) Co and b) Mn for MnTPPCl on Co/Au(111). Element specific hysteresis loops recorded at L-edge for c) Co and d) Mn (taken from [7]).

It has been shown recently that the interfacial spin polarized charge transfer between Cu(111) and TBrPP-Co(III) molecule induces a spin polarization on (otherwise non-magnetic) organic ligands [32]. Such induced spin polarization may in turn be useful for efficient spin injection into molecules.

We address now the question of how interactions at organic/ferromagnetic interface would modify the spin polarized transport. A clue can be found from the case of magnetic tunnel junctions (MTJs) having inorganic oxides as spacers. Magnetoresistance (MR) measurements for certain MTJs were shown to be in contradiction with Jullière model. For example $Co/Al_2O_3/La_{0.37}Sr_{0.67}MnO_3$ MJT showed positive MR despite Co and $La_{0.37}Sr_{0.67}MnO_3$ having spin polarization (SP) in opposite directions [33]. The

reason for negative SP was attributed to interfacial $d-sp$ bonding that created positive SP on interface Al_2O_3 layer. Ab-initio calculations have played a key role in elucidating the impact of interfacial magnetic interactions on spin-dependent tunnelling. For instance, a first principles study [34] carried out on the $Co/SrTiO_3/Co$ system revealed the presence of a small magnetic moment on the Ti site at the interface, opposite in direction to that of Co. This small negative polarization was identified as the possible reason for the spin polarization inversion observed in experiments [34]. A similar result was also found for $Co/Al_2O_3/Co$ MJT [35]. For completeness it is mentioned that apart from interfacial magnetic interactions, others factors such as the symmetry of Bloch states and the decay rates of evanescent wave within barrier thickness play a key role in determining the amplitude and sign of MR [36].

Of course spin polarized response of an organic spintronics device would depend upon the quality of organic/ferromagnetic interface [37, 38]. However organic/ferromagnetic interface may have more profound impact on the amplitude and the sign of MR due to possible interfacial hybridization similar to the case of inorganic MTJs. Indeed a theoretical study of organic Ni/octane/Ni tunnel junction has shown that the effective spin polarization is determined by the surface states present at the interface [39]. From the experimental point of view, $La_{0.37}Sr_{0.67}MnO_3/Alq_3/Co$ is considered to be the archetypal organic spintronics device [2]. Despite numerous reports of spin valve effect in Alq_3 based devices, the process of spin injection from ferromagnet to the organic semiconducting Alq_3 is not very well understood. Recently, a model has been proposed that explains the spin injection into the organic semiconductor in terms of spin-hybridization-induced polarized states (SHIPS) at the interface. [5].

The concept of SHIPS is explained in Fig. 1.10 [3]. As the organic molecule comes into contact with a ferromagnetic electrode, the DOS of the molecule can be modified in two ways. First, the DOS of the molecule is broadened by an amount that depends upon the degrees of interaction with the electrode. It is possible that the DOS in the two spin channels is broadened differently (e.g. due to offset of spin-up and spin-down bands in a ferromagnet). This spin dependant broadening may lead to a spin polarization at the interfacial molecular layer at E_F, that is opposite to that of magnetic electrodes (Fig. 1.10b). Second, the molecular orbitals are shifted due to the hybridization with the electrode. This shift is spin dependent and thus may lead to the creation of new spin-polarized states at E_F (Fig. 1.10c). The new electronic states created at E_F due to SHIPS at organic/ferromagnetic interface act as spin filter, which not only change the magnitude but may even reverse the sign of spin polarization of the injected current as compared to that of ferromagnetic electrode. The local nature of SHIPS also helps
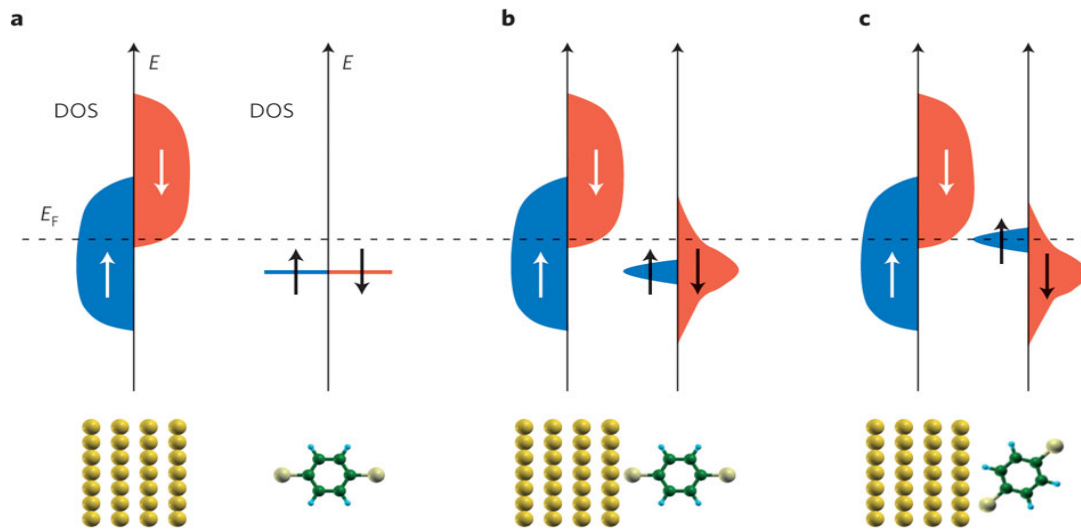
Figure 1.10: Spin-hybridization induced polarized states at the interface. a) Molecule and ferromagnetic electrode are well separated. The hybridization between the electrode and the molecule leads to spin dependent b) broadening of molecular DOS and c) shifting of the molecular orbitals. Both of these mechanism lead to the creation of new spin-polarized states at E_F which act as spin filter at organic/metal hybrid interface (taken from [3]).

explain the anomalies observed for $La_{0.37}Sr_{0.67}MnO_3/Alq_3/Co$ tunnel junctions, e.g. the change of sign of the TMR with the device size and the applied bias [5].

The results discussed above thus identify organic/ferromagnetic interfacial interactions as a key factor in determining the spin polarized response of an organic spintronics device. Indeed, the understanding of "spinterface" is now considered to be a crucial step in the future development of organic spintronics [3, 4]. From the fundamental perspective, such interfaces are shown to be rich in physics as epitomized by the observation of interfacial magnetic coupling [7, 8]. Thus a thorough study of a technologically relevant organic/ferromagnetic interface would also be valuable for the progress of fundamental interface science.

1.4 MPc molecules on metallic surfaces

The main aim of this section is to provide a general overview of the structural, electronic and magnetic properties of MPc molecules upon adsorption on metallic surfaces. While the study of MPc/metal interfacial interactions is a relatively new field of research, given the promise of technological applications, the interest in this subject has grown tremendously in the last few years. This review is not meant to be exhaustive but to

highlight the scope of this field.

1.4.1   Adsorption

A combination of experimental and theoretical (mainly DFT) techniques have been
employed in the past to study the MPc adsorption on metallic surfaces. An important
studied aspect is the orientation of molecules upon adsorption. Results from the Near
edge x-ray absorption fine structure (NEXAFS) spectroscopy have shown that for ul-
trathin films ($\sim$ 1ML), MPc molecules lie flat on the metallic substrates [40–43]. The
flat lying orientation is favorable for ultrathin films due to strong substrate-molecule
interactions. For thicker films, molecule-molecule interactions dominate the substrate-
molecule interactions, leading to bulk like structures [41, 44]. The flat-lying orientation
of the MPc molecules on metallic substrates has also been confirmed by scanning tun-
neling microscopy (STM) [45, 46].

Besides orientational order, MPc ultrathin films may also possess long-rang struc-
tural order (for example see review [47]). From a technological perspective, the control
of the growth of molecular thin films is necessary for obtaining interfaces of high qual-
ity. A recent study has highlighted the possibility of tuning the structural properties
of MPc ultrathin film on metallic surfaces. It was shown that the planar CuPc and
non-planar SnPc can be grown into well ordered films on Ag(111) [48]. The underlying
forces responsible for the structural order of SnPc or CuPc on Ag(111) were also identi-
fied, namely attractive substrate-molecule interactions and repulsive molecule-molecule
interactions. Furthermore, it was shown that the phase of MPc superstructures can be
controlled simply by a change of either the temperature or the molecular coverage.

The adsorption distances of MPc molecules on metallic substrates have been ex-
perimentally determined by x-ray standing wave (XSW) technique [48–51]. A XSW
study [50] has shown that the adsorption distance of MPc on Ag(111) depends upon
the central metal atom of the MPc molecule. DFT calculations confirmed this exper-
imental results and also highlighted that besides the adsorption distance, the central
metal may also influence the adsorption site [50]. Similar results were also found for
MnPc, FePc, NiPc and CuPc on Au(111) by a DFT study [52]. The adsorption distance
was found to be different for each molecule (generally, increasing with the increase in
the occupation of d orbital of the metal in the molecule). Also the adsorption site
of MnPc (top) was different from other molecules (HCP) on Au(111). While a direct
experimental observation of the adsorption site is difficult with STM, a combination
of various STM techniques was exploited to find out the adsorption site of CoPc on
Cu(111) [53]. These STM experiments showed that CoPc are adsorbed at the bridge
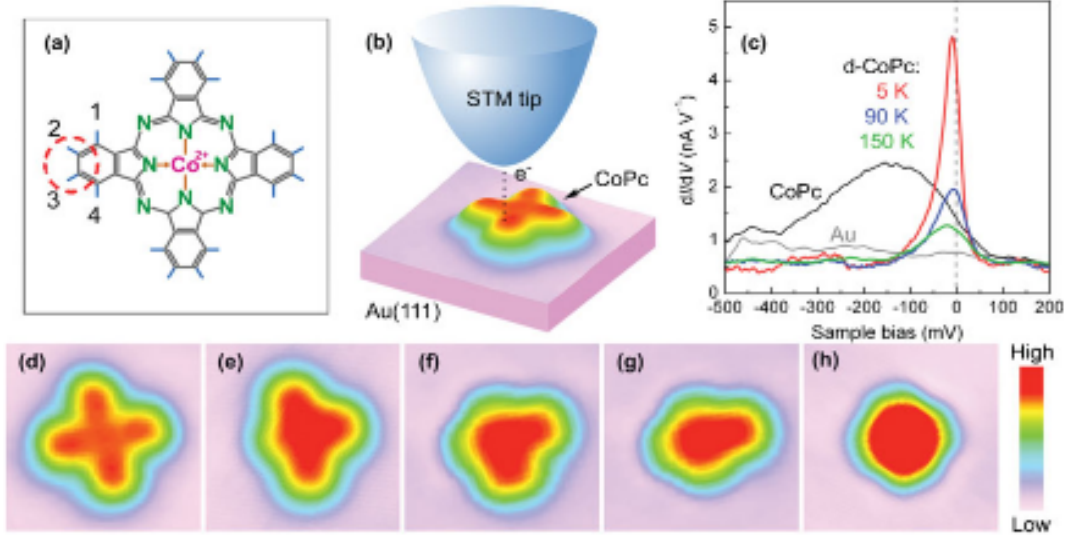
Figure 1.11: Kondo effect in dehydrogenated CoPc (d-CoPc). a) Structure of CoPc molecule. b) Process of dehydrogenation of CoPc by STM current pulse. c) dI/dV spectra of CoPc and d-CoPc. While CoPc shows a d_{z^2} resonance (black line), d-CoPc has a Kondo resonance at Fermi level shown for various temperatures. d-h) STM images during each step of dehydrogenation. d) and h) are STM images of the CoPc molecule and completely dehydrogenated CoPc molecule, respectively (taken from [56]).

position on Cu(111), consistent with DFT calculations [6, 53].

1.4.2 Electronic and magnetic properties

The electronic and magnetic properties of MPc molecules can be modified due to interaction with metallic substrates [52]. The impact of MPc/metal interactions on the molecular electronic structure and magnetism is emphasized by recent STM experiments revealing the presence of Kondo effect in the MPc molecules adsorbed on metallic surfaces [46, 54, 55]. Fig. 1.11 explains the process of obtaining Kondo resonance in CoPc on Au(111) through STM. CoPc on Au(111) exhibit no Kondo effect while DFT calculations show that the local magnetic moment of Co is quenched. Dehydrogenation of CoPc (d-CoPc) (Fig. 1.11b, d-h) distorts the molecule as the benzene rings bend towards Au(111). However Co atom shifts upwards and as a result its magnetic moment is recovered. Most crucially, due to the change of chemical environment, Kondo resonance is observed at the center of the d-CoPc (Fig. 1.11c). Kondo effect has also been observed for FePc on Au(111) [46]. Two possible adsorption sites for FePc on Au(111) were found. Interestingly, the strength of Kondo interactions changed with the change of adsorption configuration of FePc .

DFT calculations have shown that the interaction with metallic substrates generally reduces the local magnetic moment of the central atom of MPc molecules (i.e. when central atom is also magnetic) [6, 52–54, 57, 58]. In some cases, the magnetic moment is completely quenched [6, 53, 54]. The main reason for this reduction of the magnetic moment is the hybridization and the spin polarized charge transfer at the MPc/metal interface [53, 57, 58]. It is therefore evident that a smaller adsorption distance leads to stronger MPc/metal interfacial interactions and thus the reduction of the local magnetic moment of the metal atom is also stronger. Due to the similarity of MPc with porphyrin molecules, the existence of magnetic coupling between the transition metal-phthalocyanine molecules and ferromagnetic substrates can be anticipated. A spin-polarized (SP)-STM study of CoPc/Co(111) interface has addressed this issue [57]. The differential conductance (dI/dV) of the Co/CoPc/tip tunnel junction showed two distinct resonances which were attributed to two spin orientations of Co in CoPc. Furthermore, it was shown that two spin orientations of CoPc arise due to magnetic coupling with the substrate Co islands, magnetized in the opposite directions. The DFT calculations confirmed the presence of magnetic coupling between Co substrate and CoPc though the exchange mechanism responsible for magnetic coupling remained unclear.

Besides the magnetic ground state, the electronic and transport properties of MPc molecules are also strongly affected by the interfacial interactions. Adsorption and transport properties of H_2Pc and CoPc were studied on Cu(111) and Co(111) by STM and scanning tunneling spectroscopy (STS). Both molecules were found to be chemisorbed on Co(111) and physisorbed on Cu(111). The impact of interfacial hybridization on the electronic structure is shown in Fig. 1.12. The local density of states (LDOS) of CoPc (1.12a) and H_2Pc (1.12b) on Cu(111) (black dashed line) exhibit free molecular semiconducting behavior with the Fermi level lying in the energy gap. In sharp contrast to Cu(111), the strong chemical interfacial interactions with Co(111) (solid red line) modifies the local density of states (LDOS) of CoPc and H_2Pc such that both molecules exhibit metallic behavior on Co(111) as indicated by a peak at the Fermi level.

From a theoretical point of view, a precise description of the electronic and magnetic properties of MPc molecules on the metallic surfaces requires a correct estimation of the distance between MPc molecule and the substrate. However, currently available DFT functionals fail to properly describe the weak attractive vdW interactions. This limitation has been highlighted by a recent combined DFT and STM study [58]. The adsorption distance of CoPc on Cu(111) was found to be ~ 3.10 Å by a DFT study
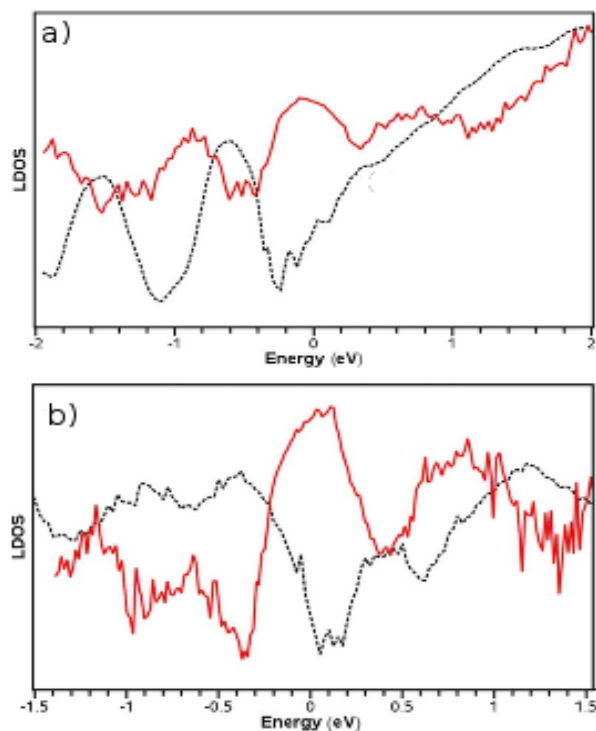
Figure 1.12: LDOS of a) CoPc and b) H_2Pc on Cu(111) (black dashed line) and Co(111) (red solid line). LDOS at E_F (corresponding to E=0 in the plot) indicates that H_2Pc and CoPc are physisorbed on Cu(111) but chemisorbed on Co(111) (taken from [45]).

based upon the generalized gradient approximation (GGA). However, simulated STM images by GGA showed poor agreement with the experimental results. The inclusion of vdW interactions reduced the adsorption distance by ~ 0.5 Å. More importantly, the electronic structure obtained with vdW correction agreed nicely with experiments.

1.5   Motivation of this thesis

The main focus of this thesis is to study MnPc/metal interfacial interactions. Ferromagnetic Co(001) and non-magnetic Cu(001) have been used as metallic substrates thus allowing for a comparative study of MnPc/ferromagnetic and MnPc/non-magnetic interfaces. The suitability of MPc molecules for such an experimental study and possible utilization in an organic spintronics device have already been discussed in section 1.2. Experimentally, synchrotron bases techniques (XMCD, XPS etc.) along with scanning tunneling microscopy (STM) are key in understanding the metal-organic/metal interfaces. From a theoretical point of view, DFT is amongst the most widely used methods to unravel the physical and chemical interactions at such interfaces. In this work, both synchrotron experiments and DFT calculations have been performed to provide a detailed and reliable description of the MnPc/metal interface. This study has also been helped by STM measurements performed in the Wulfhekel group at the Karlsruhe Institute of Technology (KIT). Here we outline some of the main questions addressed in this thesis.

One of the main goals of this work is to identify the nature of interactions responsible for MnPc adsorption on Cu(001) and Co(001), i.e., *adsorption mechanism*. In the case of chemisorption, molecular orbitals are modified very strongly which can also modify the transport properties of the adsorbed molecule. For example, a recent STM study [45] (see section 1.4 for more detailed discussion) showed that the transport properties of both CoPc and H_2Pc molecules depend strongly on the adsorption mechanism. For ferromagnetic Co(111) substrate, both molecules were found to be chemisorbed and consequently metallic, while on Cu(111) substrate, molecules were physisorbed thus exhibiting the semiconducting behavior similar to that of an isolated molecule. From the theoretical standpoint, the correct estimation of the adsorbate/substrate distance is key for the accurate determination of the adsorption mechanism. However, the determination of the adsorbate/substrate distance is a well known failure of DFT particularly for physisorbed systems since the standard density functionals fail to properly describe the *van der Waals (vdW) interactions*. The impact of vdW interactions on the adsorption of MnPc molecule constitutes an important aspect of our work.

Magnetic interactions at the MnPc/Co interface have also been studied in detail. This allows us to explore the possibility for *magnetic coupling at MnPc/Co interface*. Considering the structural similarity with Porphyrin molecules, MPc may also be expected to couple magnetically to ferromagnetic substrate. As discussed in section 1.4, Spin polarized STM study has revealed the presence of such magnetic interactions at

CoPc/Co(111) interface [57]. However the exchange mechanism responsible for such magnetic interactions is not clear.

A combination of XMCD experiments and DFT calculations have allowed us not only to confirm the presence of magnetic coupling but also to point out the physical mechanism responsible for magnetic order at the interface [59].

Finally, as already discussed, the determination of induced spin polarizations on the interfacial electronics states is critical from the perspective of organic spintronics. A detailed study of MnPc/Co interfacial chemical and magnetic properties should help understand the *"spinterface"* which is necessary for the elucidation of the underlying physics of MPc based organic spintronics devices.

Chapter 2

Ab-initio Electronic Structure Calculations

In this chapter, we briefly review the theoretical method used in this work i.e. density functional theory (DFT). In section 2.1, we describe the fundamental theorems of DFT along with a discussion on the exchange correlation functionals. In section 2.2, we introduce the plane wave pseudopotential approach within DFT which is used in this work to calculate the electronic structure. In section 2.3, we discuss the inclusion of van der Waals (vdW) interactions in DFT calculations. In section 2.4, we provide the computational details.

2.1 Density functional theory

One of the main challenges of condensed matter physics is to accurately describe the interacting many-electron systems [60]. In this respect, DFT seems to be the most promising approach as it takes electron correlation into account in a numerically feasible way. In this section, we provide a brief introduction to DFT formalism.

2.1.1 Hohenberg-Kohn theorems

Considering a system of interacting electrons in external potential $V_{ext}(\mathbf{r})$, than according to Hohenberg-Kohn (HK) theorem [61]

1) The external potential V_{ext} is determined uniquely, except for a trivial constant, by the ground state electron density $n_o(\mathbf{r})$.

As a consequence of this theorem, any physical quantity in its ground-state can be expressed as functional of the electron density. In particular, the total energy may be

written as

$$E[n] = F[n] + \int V_{ext}(\mathbf{r})n(\mathbf{r})d\mathbf{r}\,, \tag{2.1}$$

where $F[n]$ is a universal functional which includes the kinetic and electron-electron interaction energy terms.

2) The energy functional $E[n]$ is minimized by the ground-state electron density $n_o(\mathbf{r})$. This global minimum of $E[n]$ corresponds to the exact ground state energy of the system.

Unfortunately, HK theorems are not sufficient to describe the physical properties of a materiel. This is because they do not provide a way to construct wavefunctions from the electron density which is necessary to calculate $F[n]$.

2.1.2 Kohn-Sham equations

According to Kohn-Sham approach [62], the ground-state total energy functional is written as (In atomic units $e^2 = m = \hbar = 1$)

$$E[n] = T_s[n] + E_H[n] + E_{XC}[n] + \int V_{ext}(\mathbf{r})n(\mathbf{r})d\mathbf{r}\,, \tag{2.2}$$

where T_s is the kinetic energy of a non-interacting electron system given by

$$T_s = -\frac{1}{2}\sum_i \langle\psi_i|\nabla^2|\psi_i\rangle\,, \tag{2.3}$$

and E_H the Hartree energy term accounting for classical coulomb interaction

$$E_H = \frac{1}{2}\int \frac{n(\mathbf{r})n(\mathbf{r}')}{|\mathbf{r}-\mathbf{r}'|}d\mathbf{r}d\mathbf{r}'\,, \tag{2.4}$$

and where E_{XC} is the exchange-correlation functional which consists of all the effects missed by remaining terms in $E[n]$. The functional $E[n]$ given by Eq. (2.2) can be minimized with the constraint of orthonormality of wavefunctions using Lagrange multiplier technique i.e.

$$\frac{\delta}{\delta\Psi_i^*}\Big[E - \epsilon_i \int \psi_i^*(\mathbf{r})\psi_i(\mathbf{r})d\mathbf{r}\Big] = 0\,, \tag{2.5}$$

where ϵ_i is the Lagrange multiplier. This constrained minimization leads to the so called Kohn-Sham (KS) equations given as

$$\Big[-\frac{\nabla^2}{2} + V_{KS}(\mathbf{r})\Big]\psi_i(\mathbf{r}) = \epsilon_i\psi_i(\mathbf{r})\,, \tag{2.6}$$

where V_{KS} is KS potential given by

$$V_{KS}(\mathbf{r}) = V_H(\mathbf{r}) + V_{XC}(\mathbf{r}) + V(\mathbf{r}).\qquad(2.7)$$

In Eq. (2.7), $V(\mathbf{r})$ is external potential, V_H is Hartree potential

$$V_H = \frac{1}{2}\int\frac{n(\mathbf{r}')}{|\mathbf{r}-\mathbf{r}'|}\mathrm{d}\mathbf{r}',\qquad(2.8)$$

and V_{XC} the exchange correlation potential

$$V_{XC} = \frac{\delta E_{XC}}{\delta n(\mathbf{r})}.\qquad(2.9)$$

It can be thus seen that Kohn-Sham approach replaces the problem of interacting electron systems with a fictitious non-interacting system having the same density as the original system. The solution of the KS equations is the auxiliary one particle wavefunction $\psi_i(\mathbf{r})$, which can be used to calculate the electron density.

$$n(\mathbf{r}) = \sum_i |\psi_i(\mathbf{r})|^2 .\qquad(2.10)$$

2.1.3   Exchange-correlation functional

Even though KS total energy functional (Eq .(2.2)) is formally exact, it can be practically used only if the exchange-correlation functional (E_{XC}) is known. Unfortunately, there is no known exact expression of E_{XC} and DFT calculations are therefore based upon its approximative forms . Here we briefly discuss the two widely used approximations of the exchange correlation functional, namely the local density approximation (LDA) and the generalized gradient approximation (GGA) (for a detailed discussion on the exchange correlation functional and its widely used approximations, see references [60, 63–65]). In LDA, the exchange-correlation energy per electron at point $\mathbf{r}$, $\varepsilon_{XC}(\mathbf{r})$, is equal to the exchange-correlation energy per electron of homogeneous electron gas having the same density as the actual system at point $\mathbf{r}$ [66]. Thus the E_{XC} can be written as

$$E_{XC}^{LDA}[n(\mathbf{r})] = \int n(\mathbf{r})\varepsilon_{XC}(n(\mathbf{r}))\mathrm{d}\mathbf{r}.\qquad(2.11)$$

It is possible to calculate $\varepsilon_{XC}(\mathbf{r})$ for certain densities by quantum Monte Carlo method [67]. Various functionals such as the one due to Perdew and Zunger [68] have been constructed through the interpolation of quantum Monte Carlo data. The LDA has been used successfully mainly in solid state systems where the variation of the electronic

density is rather small. However LDA fails to properly describe molecular systems due to its tendency to over-bind [11]. An obvious improvement to LDA is to include not just the density n($\mathbf{r}$) at a given point $\mathbf{r}$ but also its gradient $| \nabla n(\mathbf{r}) |$, to take non-homogeneity of electron density into account. This approach is commonly referred to in literature as the generalized gradient approximation (GGA). In GGA, the E_{XC} would be written as

$$E_{XC}^{GGA}[n(\mathbf{r})] = \int n(\mathbf{r}) \varepsilon_{XC}(n(\mathbf{r}), \nabla n(\mathbf{r})) d\mathbf{r}. \qquad (2.12)$$

Since this work is mostly dedicated to studying MnPc molecule and MnPc/metal interfacial interactions, we have used the GGA functional with the PBE parameterization [11]. This functional is popular both in the condensed matter and quantum chemistry communities due to its simplicity and reliability [64, 69]. Nevertheless the PBE functional has some well known shortcomings such as its inability to accurately describe van der Waals (vdW) interactions. We discuss the problem of correlation effects within DFT in the next subsection while the vdW interactions will be the subject of section 2.3.

2.1.4 Correlation effects: DFT+U method

One of the well known failures of the standard density functionals (LDA/GGA etc.) is the description of strongly correlated materials [70]. This problem is exemplified by the case of correlated transition metal oxides whose band gap is typically underestimated by LDA/GGA. For example the antiferromagnetic insulators, CoO and FeO are described as metals by LDA [71]. The self-interaction error lies at the heart of these failures. The self-interaction of electrons in the Hartree term is canceled in the exact treatment of exchange (e.g. Hartree-Fock method) which is not the case for most of the approximate exchange correlation functionals such as GGA or LDA thus leading to spurious electronic delocalization [60].

This problem can be circumvented by taking into account the on-site coulomb electronic repulsion in localized orbitals (e.g. d or f orbitals) characterized by the Hubbard parameter (U), an approach known as 'DFT+U' method. In DFT+U method, the total energy is written as [70]

$$E_{DFT+U} = E_{DFT} + E_{Hub} - E_{DC}, \qquad (2.13)$$

where E_{DFT} is the energy calculated by a given DFT functional (LDA, GGA etc.).

The Hubbard term (E_{Hub}) accounts for on-site repulsion of electrons and E_{DC} is subtracted so as to avoid any double counting. For the implementation of DFT+U method in PWSCF, rotationally invariant formalism of E_{Hub} is used, derived from the atomic Hartree-Fock approach [70]. Furthermore, on-site coulomb repulsion is taken into account by considering only the screened first order term (F_0) in the multipolar expansion of the coulomb interaction. With this approximation the Hubbard correction reads

$$E_U = E_{Hub} - E_{DC} = \frac{U}{2} \sum_I \sum_{\sigma,m} \left\{ n_{mm}^{I\sigma} - \sum_{m'} n_{mm'}^{I\sigma} n_{m'm}^{I\sigma} \right\}, \qquad (2.14)$$

where $n_{mm'}^{I\sigma}$ is the occupation matrix of spin σ for the atomic site I, and is given by

$$n_{mm'}^{I\sigma} = \sum_{\mathbf{k},v} f_{\mathbf{k}v}^\sigma \langle \psi_{v\mathbf{k}}^\sigma | P_{mm'}^I | \psi_{v\mathbf{k}}^\sigma \rangle, \qquad (2.15)$$

where $\psi_{\mathbf{k}v}$ is the Kohn-Sham wavefunction of the valence electrons corresponding to the state $\mathbf{k}v$ and $f_{\mathbf{k}v}^\sigma$ represents the occupation number. $P_{mm'}$ is the projection operator given as $P_{mm'}^I = |\phi_{lm}^I\rangle\langle\phi_{lm'}^I|$, where ϕ_{lm}^I is the correlated orbital atomic wavefunction with orbital quantum numbers (l, m) for the atomic site I.

For transition metal-organic molecules, the correlation effects at the metallic site can play an important role in determining the ground state electronic and magnetic structure of the molecule. For example, while available exchange-correlation functionals fail to correctly predict the magnetic ground state of iron-porphyrin complexes, the correct magnetic state can be obtained by introducing the Hubbard U parameter [72]. DFT+U method has also been used to study the spin-cross over systems [73].

2.2 Plane wave pseudopotential method

In this work, the plane wave pseudopotential method has been used for all the electronic structure calculations as implemented in Quantum-Espresso Package [10]. In this section, we review the fundamental concepts associated with this method.

2.2.1 DFT in plane wave representation

According to Bloch's theorem, the electronic wavefunction of a periodic system can be represented as the product of a plane wave part, $e^{i\mathbf{k}\cdot\mathbf{r}}$ and a lattice periodic part $u_{i\mathbf{k}}(\mathbf{r})$

$$\psi_{i\mathbf{k}}(\mathbf{r}) = e^{i\mathbf{k}\cdot\mathbf{r}} u_{i\mathbf{k}}(\mathbf{r}), \qquad (2.16)$$

where **k** is a wave-vector in the Brillouin zone and i a band index. The periodic part can be expanded in plane waves

$$u_{i\mathbf{k}}(\mathbf{r}) = \sum_{\mathbf{G}} c_{i,\mathbf{G}}\, e^{i\mathbf{G}\cdot\mathbf{r}}\,, \qquad (2.17)$$

where **G** represents a reciprocal lattice vector. Putting the expression of $u_{i\mathbf{k}}(\mathbf{r})$ (Eq. (2.17)) back into Eq. (2.16)

$$\psi_{i\mathbf{k}}(\mathbf{r}) = \sum_{\mathbf{G}} c_{i,\mathbf{k}+\mathbf{G}}\, e^{i(\mathbf{k}+\mathbf{G})}\,. \qquad (2.18)$$

Thus electronic wavefunction can be expanded in discrete plane wave basis set for each **k**. The substitution of Eq. (2.18) into Eq. (2.6) gives the KS equation in the plane wave form [66]

$$\sum_{\mathbf{G}'} \Big[-\frac{1}{2}\,|\mathbf{k}+\mathbf{G}|^2\,\delta_{\mathbf{G},\mathbf{G}'} + V_H(\mathbf{G}-\mathbf{G}') + V_{ion}(\mathbf{G}-\mathbf{G}')$$

$$+ V_{XC}(\mathbf{G}-\mathbf{G}')\Big] c_{i,\mathbf{k}+\mathbf{G}'} = \epsilon_i c_{i,\mathbf{k}+\mathbf{G}}\,. \quad (2.19)$$

In principle, an infinite plane wave basis set would be required to expand a wavefunction. In practice, however, a finite cut-off is chosen. This approach is justified since the coefficients $c_{i,\mathbf{k}+\mathbf{G}}$ of lower kinetic energy plane wave are more important than those with higher kinetic energy. In a typical electronic structure calculation, the value of energy cut-off is varied until the total energy is converged. This systematic way of choosing an energy cut-off is one of the main advantages of plane wave pseudopotential method.

2.2.2   k-point sampling

The computation of the physical properties such as the charge density require a summation over **k**-points in the first Brillouin zone. This means that **k**-points used in the calculations should be sufficiently dense so that results are well converged. The number of **k** points used in a calculation can be reduced considerably by making use of the crystal symmetry. Thus the calculations are performed on the irreducible Brillouin zone which is typically much smaller than the first Brillouin zone. A function $f_i(\mathbf{k})$ can be averaged over the Brillouin zone as

$$\bar{f}_i(\mathbf{k}) = \sum_{\mathbf{k}}^{IBZ} w_{\mathbf{k}} f_i(\mathbf{k})\,, \qquad (2.20)$$

where $w_{\mathbf{k}}$ is the weighting factor of a given $\mathbf{k}$ point and IBZ stands for the irreducible Brillouin zone. Typically, a uniform mesh of $\mathbf{k}$-points is generated as proposed by Monkhorst and Pack [74].

In this work, a large supercell has been used in order to properly describe the interfacial interactions between MnPc and metallic substrates. Therefore all the calculations are performed only on Γ-point.

2.2.3 Pseudopotential approach

Even though the electronic wavefunction can be expanded in a plane wave basis set, the plane wave basis may not be the best choice to perform the electronic structure calculations. This is due to the fact that the valence electron wavefunctions are strongly oscillating near the core region (Fig. 2.1). Such wavefunctions require prohibitively large number of plane waves to be expanded. The solution to this problem can be found by replacing the strong ionic potential within the core region by a weak potential, termed as pseudopotential [66]. The corresponding pseudo-wavefunction will be much smoother in the core region and can be therefore expanded in the plane waves. Fig. 2.1 provides a schematic illustration of the concept of pseudopotential. Within core region, i.e., the region below cut-off radius (r_c), strong all-electron ionic potential is replaced by a much weaker pseudopotential. Consequently the pseudo-wavefunction is much smoother than the all electron wavefunction below r_c. Beyond r_c, both pseudo and all-electron potentials as well as corresponding wavefunctions are identical to each other.

Ideally, the pseudopotential should be generated in such a way that it should have the same scattering properties as that of the all-electron potential (a detailed discussion on the procedure of the pseudopotential generation can be found in reference [60]). The phase-shifts produced by the core region are angular momentum dependant. Outside the core region, the potential is coulombic, depending only on the distance from the nucleus. Thus the pseudopotential operator can be written as

$$\hat{V}_{SL} = V_{local}(\mathbf{r}) + \sum_{lm} |Y_{lm}\rangle \delta V_l(\mathbf{r}) \langle Y_{lm}|, \qquad (2.21)$$

where $\hat{V}_{SL}$ is the semilocal potential operator and $V_{local}(\mathbf{r})$ is the local potential i.e. the same for all angular momentum components. The second term on the right hand side of Eq. (2.21) provides the angular momentum dependence to the pseudopotential operator and therefore it is zero outside r_c.

Kleinman and Bylander (KB) [75] proposed an approach in which the semi local
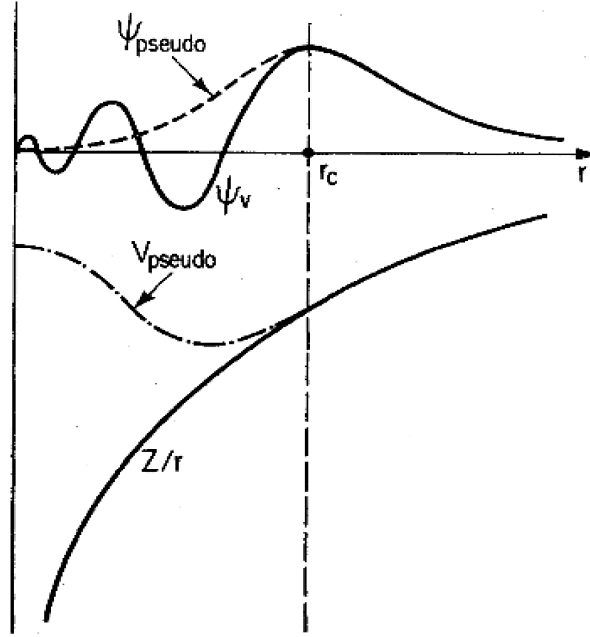
Figure 2.1: Schematic representation of pseudopotential concept. All-electron ionic potential and wavefunction (solid) compared to the corresponding pseudopotential and pseudo-wavefunction (dashed). r_c is cut-off radius (taken from [66]).

operator is replaced by a fully non-local operator of the form

$$\hat{V}_{NL} = V_{local}(\mathbf{r}) + \sum_{lm} \frac{|\psi_{lm}^{PS}\delta V_l(\mathbf{r})\rangle\langle\delta V_l(\mathbf{r})\psi_{lm}^{PS}|}{\langle\psi_{lm}^{PS}|\delta V_l(\mathbf{r})|\psi_{lm}^{PS}\rangle}, \tag{2.22}$$

where ψ_{lm}^{PS} is the reference pseudo-atomic wavefunction. The KB approach is computationally convenient since (2.22) reduces the number of integrals for $V_l(\mathbf{r})$ from $N_{PW}m(N_{PW}+1)/2$ to $N_{PW}m$ for each l where N_{PW} is the number of plane-waves used in the expansion of wavefunction and m is the projection of angular momentum l.

2.2.3.1 Norm-conserving pseudopotentials

It is possible to construct pseudopotential in such a way that inside the core, the nodeless pseudo-wavefunction has the same norm as the all-electron wavefunction. This is the norm conserving condition that ensures that the total charge inside the core region for both pseudo and all-electron wavefunction is the same i.e.

$$\int_0^{r_c} |\psi(\mathbf{r})|^2 \, d\mathbf{r} = \int_0^{r_c} |\psi^{PS}(\mathbf{r})|^2 \, d\mathbf{r}. \tag{2.23}$$

Equation (2.23) ensure that the charge density generated by the pseudo-wavefunction outside the core region is the same as all-electron wavefunction. It has been pointed out [76] also that the fulfilment of norm conservation condition also ensures correct scattering properties for the pseudopotentials. These properties make norm-conserving pseudopotentials to work well in different atomic environments, a property referred to as transferability [66].

2.2.3.2   Ultrasoft pseudopotentials

The effectiveness of norm-conserving pseudopotential is severely limited for the cases of highly localized orbitals such as the transition metal $3d$ orbitals. This problem is explained in Fig. 2.2 where norm-conservation constraint results in a pseudo wavefunction that is no more smoother than all-electron wavefunction for the case of oxygen $2p$ orbital.

Vanderbilt [77] proposed a method that considerably improves the smoothness of the pseudo wavefunctions but at the expense of norm conserving property as formulated in Eq. (2.23). In vanderbilt approach, a generalized eigenvalue problem is solved

$$(H - \epsilon_i S) \, |\psi_i^{PS}\rangle = 0 \,, \tag{2.24}$$
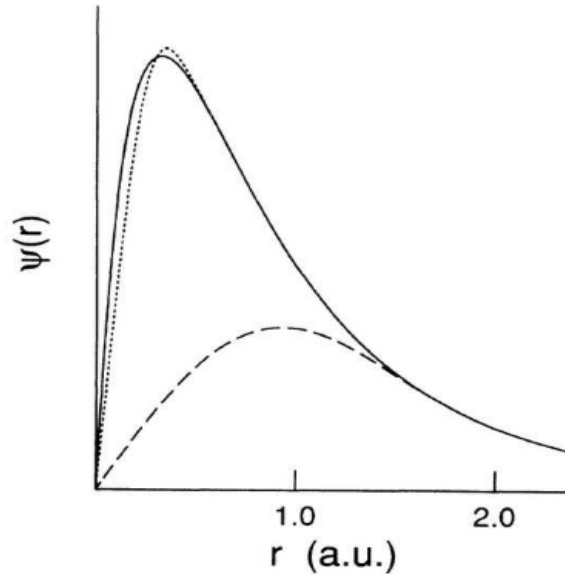
Figure 2.2: All electron wavefunction (solid) of oxygen 2p orbital and the corresponding norm-conserving (dotted) and ultrasoft pseudo wavefunction (dashed). The relaxation of the norm-conservation constraint leads to a much smoother pseudo wavefunction (taken from [77]).

where S is the non-local operator.

$$S = 1 + \sum_{i,j} Q_{ij} \, |\beta_i\rangle\langle\beta_j| \,, \tag{2.25}$$

where β_i is the beta function given by

$$\beta_i = \sum_j (B^{-1})_{ij} \, |\chi_j\rangle \,, \tag{2.26}$$

where $B^{ij} = \langle\psi_i^{PS}|\chi_j\rangle$ and $|\chi_i\rangle = (\epsilon_i - T - V_{local})\,|\psi_i^{PS}\rangle$. Q_{ij} takes into account the charge lost when the norm-conservation is relaxed

$$Q_{ij} = \langle\psi\,|\,\psi\rangle_{r_c} - \langle\psi^{PS}\,|\,\psi^{PS}\rangle_{r_c} \,, \tag{2.27}$$

where ψ represents all-electron wavefunction and $\langle\psi\,|\,\psi\rangle_{r_c}$ means that the upper limit of integral is restricted to cut-off radius r_c. For norm-conserving pseudopotential, Q_{ij} is zero. One can define non-local potential operator

$$V_{NL} = \sum_{i,j} D_{ij} \, |\beta_i\rangle\langle\beta_j| \,, \tag{2.28}$$

where D_{ij} is defined as

$$D_{ij} = B_{ij} + \epsilon_j Q_{ij} \,. \tag{2.29}$$

As evident, a trial wavefunction ψ_{nk} used in self-consistent calculations should be normalized as follows

$$\langle\psi_{n\mathbf{k}}\,|\,S\,|\,\psi_{n'\mathbf{k}}\rangle = \delta_{nn'} \,, \tag{2.30}$$

and total charge density is calculated as

$$n(\mathbf{r}) = \sum_{n,k} \left[\, |\psi_{n\mathbf{k}}|^2 + \sum_{i,j} Q_{ij}(\mathbf{r})\langle\psi_{n\mathbf{k}}\,|\,\beta_i\rangle\langle\beta_j\,|\,\psi_{n\mathbf{k}}\rangle \right] \,. \tag{2.31}$$

The second term in Eq. (2.31) accounts for the charge deficit in the core. The effect of the relaxation of the norm-conservation constraint can be seen in Fig. 2.2. The ultrasoft pseudo-wavefunction has much higher r_c and consequently it is much smoother than norm-conserving pseudo-wavefunction.

In this work, a huge supercell with large number of atoms has been used for the proper description of MnPc/metal interface. All calculations are performed using ultrasoft pseudopotentials that reduce kinetic energy cut-off to 30 Ry. However, the charge

density cut-off is 10 times (unlike 4 times for norm-conserving pseudopotential) the kinetic energy cut-off due to the presence of augmentation charge.

2.3   Van der Waals interactions

One of the well known weaknesses of the standard density functionals is their inability to describe properly the van der Waals (vdW) interactions [78]. These interactions are non-local and long range in nature and thus are particularly important for sparse systems such as graphene multilayers and MoS_2 [79]. This limitation of standard functionals may lead not only to the underestimation but even absence of binding for such systems [9]. As for adsorption of organic molecules on metallic surfaces, this means that the physics of physisorbed systems is poorly described in DFT due to the absence of vdW interactions.

Recently, various schemes have been proposed to include vdW interactions in the frame work of DFT (for example, see reviews [78, 80, 81]). Generally, these approaches can be divided into ab-initio or empirical depending upon the nature of approximation employed to include vdW interactions. A widely used ab-initio method is vdW density functional (vdW-DF). In vdW-DF, the exchange correlation functional is given by [79, 82]

$$E_{XC}^{vdW}[n] = E_X^{revPBE}[n] + E_C^{LDA}[n] + E_C^{nl}[n] \,, \tag{2.32}$$

where $E_X^{revPBE}[n]$ and $E_C^{LDA}[n]$ repersent the revPBE exchange and LDA correlation functionals respectively. $E_C^{nl}[n]$ is non-local, long range correlation energy that primarily consists of vdW interactions. $E_C^{nl}[n]$ can be calculated as

$$E_C^{nl}[n] = \int n(\mathbf{r})n(\mathbf{r'})\phi(\mathbf{r},\mathbf{r'})\mathrm{d}\mathbf{r}\mathrm{d}\mathbf{r'} \,, \tag{2.33}$$

where the kernel $\phi(\mathbf{r},\mathbf{r'})$ is calculated using fluctuation-dissipation theorem, RPA and pole-plasmon approximation [29].

Despite it successes, DFT-DF method is rather difficult to apply to larger systems due to its numerical complexity [83]. In particular, the six dimensional integral must be calculated (Eq. (2.33)) to obtain the correlation energy which can be computationally expensive for large systems. For example, for a routine molecular-surface relaxation calculations the computational cost could be prohibitive with a self consistent DFT-DF method [9]. An alternative way to include vdW interactions is to use the semi-empirical correction to compute the dispersion energy i.e. DFT-D method, proposed by Grimme [12, 84]. We discuss this last method in the next subsection.

2.3.1   DFT-D Method

Here we describe the DFT-D method in its 'D2' version (referred to as DFT-D2 method in literature). In DFT-D method, an empirical term is added ($C_6 \cdot R^{-6}$ correction) to the Kohn-Sham total energy in order to take the dispersion interactions into account. DFT-D method has been tested rigorously and shown to be robust for variety of systems [83]. A particularly attractive feature of DFT-D method is its lower numerical cost that makes it applicable to large systems. Consequently, we have used DFT-D method to include vdW interaction in this work. In DFT-D method, the total energy is given as [12]

$$E_{DFT-D} = E_{KS} + E_{Disp} \,, \tag{2.34}$$

where E_{KS} is the self consistant Kohn-Sham energy and E_{Disp} is the empirical term for the dispersion correction to the total energy. E_{Disp} is calculated as follows

$$E_{Disp} = -S_6 \sum_{i}^{N_{at}-1} \sum_{j=i+1}^{N_{at}} \frac{C_6^{ij}}{r_{ij}^6} f_{dmp}(r_{ij}) \,, \tag{2.35}$$

where r_{ij} is interactomic distance, C_6^{ij} the dispersion coefficient for the atomic pair and N_{at} the number of atoms in the system. $f_{dmp}(r_{ij})$ is the damping factor which determine the range of dispersion correction (E_{Disp} should be negligible for the case of covalent bonding).

$$f_{dmp}(r_{ij}) = \frac{1}{1 + e^{-d(r_{ij}/r_0 - 1)}} \,, \tag{2.36}$$

where r_0 is the sum of atomic vdW radii. The parameter d in Eq. (2.36) is chosen to be 20 to ensure the correct estimation of the dispersion energy in short and intermediate range. Dispersion co-efficient for atomic pairs C_6^{ij} is calculated as the geometric mean of atomic coefficients

$$C_6^{ij} = \sqrt{C_6^i C_6^j} \,, \tag{2.37}$$

where C_6^i is the dispersion coefficient for atom i. Atomic C_6 coefficients are derived from London formula of dispersion. However, for group I, II and transition metals, C_6 coefficients are calculated as the average of the coefficients of the preceding rare gas and the succeeding group III atoms. Finally, global scaling factor S_6 is determined by a least square fitting for each density functional. For PBE, a value of 0.75 is found to be optimal.

DFT-D approach has been implemented in Quantum Espresso package with the

inclusion of periodic boundary condition [85]

$$E_{Disp} = -S_6 \sum_{i}^{N_{at}-1} \sum_{j=i+1}^{N_{at}} \sum_{R} \frac{C_6^{ij}}{(r_{ij} + R)^6} \, f_{dmp}(r_{ij} + R) \,, \qquad (2.38)$$

$$f_{dmp}(r_{ij} + R) = \frac{1}{1 + e^{\dfrac{-d(r_{ij} + R)}{r_0} - 1}} \,, \qquad (2.39)$$

where R in Eq. ((2.38)-(2.39)) stands for different periodic lattice vectors. The cut-off for the summation over R is chosen so that E_{Disp} is sufficiently converged. In this work, a cut-off of 105 Å has been used.

2.4   Computational details

The DFT calculations reported here (besides geometry optimization) are carried out by means of the plane-wave pseudopotential method [77], as implemented in the PWSCF package [10]. For the exchange-correlation potential, we used the generalized gradient approximation (GGA) as parameterized by Perdew, Burke, and Ernzerhof (PBE)[11]. All calculations are performed with ultrasoft pseudopotentials. A kinetic energy cutoff of 30 Ry has been used for the plane-wave basis set and for the convergence of the charge density we used a cut off of 300 Ry.

The surfaces of Co(001) and Cu(001) have been modeled by using periodic supercells of three atomic layers of (8×8) atoms separated by a vacuum region. It has been shown that three monolayers are sufficient to obtain well converged results[6]. The lattice vector perpendicular to substrate surface is 14nm for the GGA calculations. Because the aim is to study a single molecule on metallic surfaces, we used only the gamma point to sample the first Brillouin zone. The effect of vdW interactions have been taken into account by following the GGA-D approach in its D2 version, developed by Grimme [12] and later implemented in the PWSCF package by Barone and coworkers [85]. We have used the standard values of the global scaling factor (S_6=0.75 for PBE) and the steepness parameter of damping function (d=20, see Eq. (2.36)). Moreover, the value of lattice vector perpendicular to surface is increased to 30 nm for GGA-D calculations.

The structural relaxation of MnPc/Co(001) and MnPc/Cu(001) has been performed by VASP using the projector augmented wave (PAW) method. During the geometry optimization, MnPc molecule and two top surface layers were allowed to relax while the third surface layer was held fixed. The convergence criteria for the total energy

and force were 10^{-6} eV and $5{\times}10^3$ eV/Å respectively.

2.4.1   Löwdin population analysis

The magnetic moments, the charges and the DOS presented in this work are calculated by means of Löwdin population analysis. Here we briefly explain the methodology of Löwdin population analysis (discussion is based upon references [86, 87]).

In Löwdin population analysis, the atomic charges are calculated by projecting orthonormalized atomic orbitals onto the occupied block orbitals . The DOS projected onto orthonormalized atomic orbital $\bar{\phi}$ (i.e. PDOS) is calculated as

$$n_\phi(\epsilon) = \sum_v \sum_{\mathbf{k}} |\langle \psi_{v,\mathbf{k}} | \bar{\phi} \rangle|^2 \, \delta(\epsilon - \epsilon_{v,\mathbf{k}}) \,, \tag{2.40}$$

where $\psi_{v,\mathbf{k}}$ is the vth occupied Bloch (Kohn-Sham) orbital at wave vector $\mathbf{k}$ and $\epsilon_{v,\mathbf{k}}$ represents the corresponding eigenvalue. The orthonormalized atomic orbital $\bar{\phi}(\mathbf{r})$ is defined as

$$\bar{\phi}_\mu(\mathbf{r}) = \sum_\nu S_{\mu\nu}^{-\frac{1}{2}} \phi_\nu \,. \tag{2.41}$$

S is the overlap matrix of the atomic orbitals $\phi_i(\mathbf{r})$

$$S_{\mu\nu} = \langle \phi_\mu | \phi_\nu \rangle \,. \tag{2.42}$$

$\bar{\phi}$ follows the orthonormality condition

$$\langle \phi_\nu | \bar{\phi}_\mu \rangle = \langle \bar{\phi}_\mu | \phi_\nu \rangle = \delta_{\nu\mu} \,. \tag{2.43}$$

The charge associated with orbital μ is calculated as

$$Q_\mu = \sum_v^{occupied} \sum_{\mathbf{k}} |\langle \psi_{v,\mathbf{k}} | \bar{\phi} \rangle|^2 \,. \tag{2.44}$$

The total charge of an atom A is obtained by summing the charges of all its orbitals, $Q_A = \sum_{\mu \in A} Q_\mu$.

The intergrated local density of states (LDOS) within the energy range $(\epsilon_{min}, \epsilon_{max})$ is calculates as

$$N(\epsilon_{min}, \epsilon_{max}, \mathbf{r}) = \sum_v \sum_{\mathbf{k}} \int_{\epsilon_{min}}^{\epsilon_{max}} |\psi_{v,\mathbf{k}}(\mathbf{r})|^2 \, \delta(\epsilon - \epsilon_{v,\mathbf{k}}) \mathrm{d}\epsilon \,. \tag{2.45}$$

Chapter 3

Experimental Methods

The experimental work done in this thesis is mainly based on synchrotron radiation techniques. X-ray absorption spectroscopy (XAS) and x-ray magnetic circular dichroism (XMCD) have been performed to study the adsorption and the magnetism of MnPc molecules on Cu(001) and Co(001). Spin-resolved photoemission has been employed to study the spin polarization at the MnPc/Co(001) interface. X-ray standing wave (XSW) technique is utilized to determine the adsorption distance of MnPc on Cu(001). In this chapter, a basic introduction to all the experimental techniques used is provided. This chapter is organized as follows. In section 3.1 we discuss the conceptual basis of XAS and XMCD. We also explain the NEXAFS spectroscopy technique used to determine the molecular orientation. In section 3.2 we describe the fundamental principles of spin-resolved photoemission technique. In section 3.3, we provide the basics of XSW technique.

3.1 X-Ray magnetic circular dichroism

X-ray magnetic circular dichroism (XMCD) is defined as the difference in the absorbtion of left circularly polarized (LCP) and right circularly polarized (RCP) x-rays [88]. While initially the presence of the x-ray magnetic dichroism was predicted theoretically, the first unambiguous experimental proof of its existence did not come until 1987 [89]. An important step towards the development of XMCD as experimental tool was the derivation of sum rules [90] which can be used to calculate the orbital and spin magnetic moments. Nowadays, thanks to the coherent and intense x-rays from synchrotron radiation sources and the development of insertion devices optimized for the production of x-rays with adjustable polarization, XMCD has developed into a powerful experimental tool in magnetism. The greatest advantage of XMCD lies in

its element selectivity, which is not possible for other experimental techniques such as SQUID. In this section, the underlying physics and practical aspects associated with XMCD spectroscopy are discussed.

3.1.1   X-absorption spectroscopy

Since XMCD spectra results from the difference of x-ray absorption spectra of left and right circularly polarized light, x-ray absorption spectroscopy (XAS) lies at the heart of XMCD. In XAS, x-ray absorption coefficient (μ) is measured over the range of photon energies. As an example, x-ray absorption spectrum of Fe (in FeO) is shown in Fig. 3.1. In a typical x-ray absorption spectra, μ decreases with increase in energy until
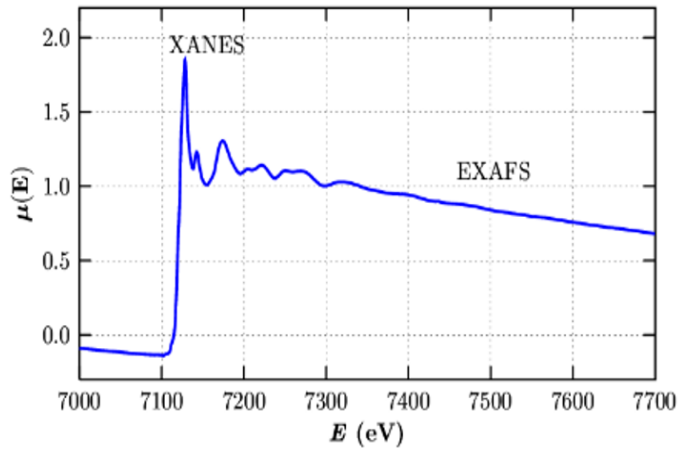
Figure 3.1: A typical x-ray absorption spectrum. X-ray absorption near edge structure (XANES) (also called near edge x-ray absorption fine structure (NEXAFS)) corresponds to a region from the edge to 30-40 eV above the edge. Oscillatory region after $\sim$ 40 eV corresponds to the extended x-ray absorption fine structure (EXAFS) (taken from [91]).

there is a sharp rise. This sharp rise is called the absorption edge [92]. Absorption edge corresponds to the transition of ground state electrons to an excited state. Theoretically, μ is proportional to the transition rate determined by Fermi's golden rule [93, 94]. Within dipolar approximation

$$\mu \propto |\langle \psi_f \left| e \cdot r \right| \psi_i \rangle|^2 \ \delta(E_f - E_i - hw) , \qquad (3.1)$$

where ψ_i and ψ_f represent the initial and the final states and the delta function ensures energy conservation. Note that the matrix element in Eq. (3.1) is non-zero only if the dipolar selection rules are satisfied, i.e., the orbital quantum numbers of the initial and the final states differ by 1 ($\Delta l = \pm 1$) and the spin is conserved ($\Delta S = 0$) during the

transition [94]. For the theoretical calculations of x-ray absorption spectra, many-body states (ψ_i and ψ_f) are replaced by computationally tractable one-electron states [92].

With the advent of synchrotron radiation, XAS has become a widely used experimental tool with applicability to a wide range of scientific problems. In general, a x-ray absorption spectrum can be divided into two regions. Near edge x-ray absorption fine structure (NEXAFS) corresponds to a region from edge to 30-40 eV above the edge. Oscillatory region after ~ 40 eV corresponds to the extended x-ray absorption fine structure (EXAFS). NEXAFS spectroscopy is used to determine the orientation of the adsorbed molecules [95]. NEXAFS can also be used to find out the valence state of the absorbing atom. EXAFS spectroscopy is employed to obtain the local structure around the absorbing atom [96]

Depending upon the nature of the sample and the measurement, various techniques are available to perform XAS. For example, in transmission technique, x-ray intensity before and after passing through the sample is used to measure the x-ray absorption coefficient. Fluorescence yield can also be used to measure the x-ray absorption spectra. In total electron yield (TEY) method, the photoelectrons are used to measure the x-ray absorption spectra [88]. An excited electron in an x-ray absorption process could de-excite through the emission of Auger electrons. This auger yield (which dominates the fluorescence in soft x-ray region) is a direct measure of x-ray absorption process [97]. However, the total TEY signal contains both the auger yield and the secondary electrons created by auger electrons. TEY is a surface sensitive technique since electrons are emitted from 25-40 Å of the sample [88]. TEY is now a standard detection technique for XAS for surface and interface measurements.

3.1.1.1 NEXAFS spectroscopy: orientation of molecules

NEXAFS spectroscopy has been used extensively to determine the orientation of the molecules upon adsorption [95]. In planer π-conjugated molecules, the energetic positions of π^* and σ^* orbitals are different [40]. Also the bonds in such materials are directional [97]. As a result, the intensity of x-ray absorption depends upon the direction of the electric field vector of the linearly polarized light. This polarization dependant variation of x-ray absorption intensity is exploited in the NEXAFS spectroscopy to determine the orientation of molecules on the substrates. Fig. 3.2 explains the application of NEXAFS spectroscopy for the determination of the orientation of benzene (C_6H_6) on Ag(011) [97].

In benzene, π^* orbitals precede σ^* orbitals in energy (left side of Fig. 3.2) . Therefore the range of C 1s $\rightarrow \pi^*$ and C 1s $\rightarrow \sigma^*$ transitions in x-ray absorption spectra can
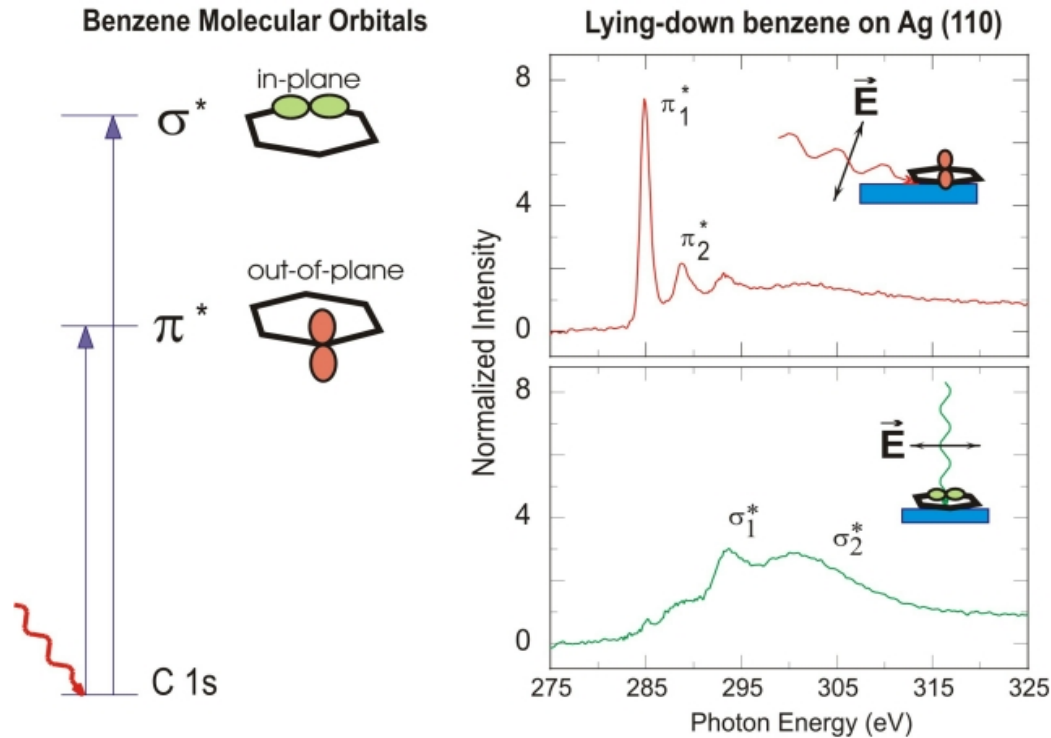
Figure 3.2: (Left) Schematic of the transition from C 1s core level to the unoccupied out of plane π^* and inplane σ^* orbitals. (Right) NEXAFS spectra of benzene on Ag(011) for the electric field vector perpendicular (top panel) and parallel (bottom panel) to the surface (taken from [97]).

easily be identified. When the electric field vector of the x-rays is perpendicular to the surface, intensity of π^* region is increased whereas σ^* orbitals are dominant when the polarization vector is parallel to the surface (right side of Fig. 3.2). This shows that inplane (out of plane) benzene orbitals are parallel (perpendicular) to the underlying surface and therefore benzene is lying flat on Ag(011).

3.1.2   Origin of XMCD effect

A "Two step model" offers a simple and intuitive explanation of the XMCD effect. Within this model, the first step describes the excitation of core electrons by circularly polarized light. Here for simplicity, we discuss only $2p \rightarrow 3d$ transition[1]. The angular momentum (or helicity) of right and left circularly polarized photons are $+\hbar$ and $-\hbar$ respectively according to Feynman's definition. During the absorption process of a photon, the photon's angular momentum is completely transferred to the electron due

---

[1]This discussion on "two step model" is based on references [98, 99]

to conservation of angular momentum. Let us consider a photoelectron that is excited from spin-orbit-split core levels e.g. the $2p_{1/2}$ and $2p_{3/2}$ levels corresponding to the L_2 and L_3 absorption edges. Then part of the photon angular momentum can be transferred to spin via spin-orbit coupling. The momentum transferred by left circularly polarized photons to the electron is opposite to that transferred by right circularly polarized light. Therefore, photoelectrons of opposite spins are produced in the two cases. Furthermore, since the L_3 and L_2 edges have opposite spin-orbit coupling ($l+s$ at L_3 edge and $l-s$ at L_2 edge, where l and s are the orbital and spin quantum numbers), the spin polarization of electrons will be opposite at the two edges. The quantization axis in the first step is defined by the helicity of photons

The magnetic properties of the sample are responsible for the second step. In a ferromagnet, the 3d valence band is exchange-split, resulting in a DOS asymmetry at the Fermi level (E_F). In the case of a hard ferromagnet like Co, there are more minority spin states than majority spin states at E_F. For the specified relative orientations of photon helicity and applied magnetic field, the absorption amplitude at the edge in turn reflects this spin-polarized DOS. It is in this sense that the ferromagnet acts as a spin detector of the photoelectron.

Thus a combination of the first step (production of spin-polarized excited electrons) and the second step (ferromagnet acting as spin filter) results in different x-ray absorption spectra for different polarizations of light in the case of a ferromagnetic sample. This difference corresponds to XMCD and qualitatively shows the presence of magnetism in the sample. The two step model is schematized in Fig. 3.3. It should be noted that the "two step model" is based on single electron picture and provides only a qualitative explanation of XMCD effect. A proper description of XMCD should include the multiplet effects which are taken into account by the ligand field multiplet theory (LFMT) [88]. In LFMT, the initial and final states are described as multiplets. In particular, the interactions between partially filled core and valence states are taken into account in the final state [92]. More details on the description of XMCD within multiplet theory can be found in review [94].

3.1.3   XMCD sum rules

One of the main advantages of XMCD is the experimental determination of the spin and the orbital magnetic moments using the sum rules. If we sum the contribution to XMCD of all the electrons that can be excited from a spin-split core level, the result only reflects an imbalance in the orbital moments of the final states as there is always a pair of photoelectron with opposite spin polarization excited from a core level. In
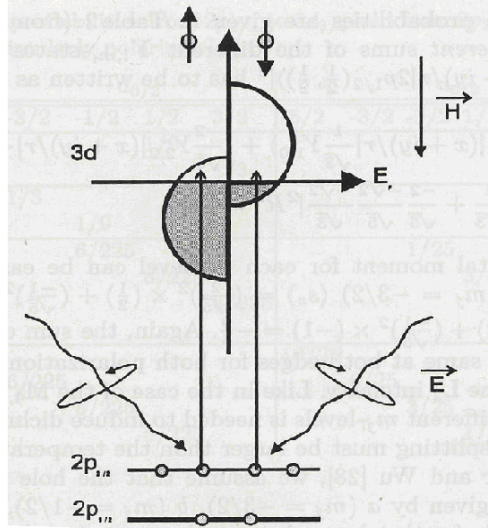
Figure 3.3: A schematic of the two step model. The first step involves the excitation of a core electron. In the second step, the ferromagnet acts as spin detector through its exchange-split d bands at E_F (taken from [100]).

contrast, the difference of dichroic intensity at two edges reflects a spin imbalance. This is the essence of magneto-optical sum rules [89]. These rules were first derived by Thole [90], while alternate ways to obtain them were given by other authors. Mathematically, these rules (for 2p → 3d transition) can be presented as follows [100].

$$\langle L_z \rangle = 2\,(10 - n)\,\frac{(\Delta L_3 + \Delta L_2)}{\displaystyle\int_{L_2 + L_3} (\mu^+ + \mu^- + \mu^0)}\;, \tag{3.2}$$

$$\langle S_z \rangle = \frac{3}{2}\,(10 - n)\,\frac{(\Delta L_3 - 2\Delta L_2)}{\displaystyle\int_{L_2 + L_3} (\mu^+ + \mu^- + \mu^0)} - 3.5\,\langle T_z \rangle\;, \tag{3.3}$$

where ΔL_2 and ΔL_3 are the integrals of the XMCD spectra at the L_2 and L_3 edges respectively, μ^+, μ^- and μ^0 are the absorption coefficients for right, left and linearly polarized light respectively and n the number of electrons in the valence shell and $\langle T_z \rangle$ is the magnetic dipole operator. Generally, the expectation value of $\langle T_z \rangle$ is much smaller than the spin moment and therefore its contribution can be neglected in most cases [89]. The sum rules (Eqs. (3.2)-(3.3)) thus allow for the experimental determination of spin magnetic moment $\left(-2\,\dfrac{\mu_\beta \langle S_z \rangle}{\hbar} \right)$ and orbital magnetic moment $\left(-\dfrac{\mu_\beta \langle L_z \rangle}{\hbar} \right)$.

Due its element selectivity and the possibility of quantitative analysis, XMCD is a powerful tool to study magnetism. In this work, presence of two magnetic elements

(Co substrate and Mn) necessitates the utilization of XMCD. Also the combination of XMCD and element specific hysteresis loops allow us to answer the question of interfacial ferromagnetic coupling in an unambiguous way.

3.1.4 Experimental conditions

In this thesis, the XAS/XMCD experiments discussed in the later chapters are done either at the Swiss Light Source (SLS) or European Synchrotron Radiation Facility (ESRF). Here we summarize the sample preparation procedures and the experimental conditions.

XAS/XMCD measurements at SLS were performed at the surface/interface microscopy (SIM) beamline. Samples were grown in the preparation chamber (base pressure of P= 5×10^{-10} mbar) of the 7 T cryomagnet setup maintained by the IPCMS and installed on the SIM beamline at SLS. A number of cycles of Ar etching/annealing ($575°$ C) were performed on a commercial Cu(001) single crystal so as to remove C contamination and promote surface reconstruction. Then 5 monolayers (ML) of Co were deposited on Cu(100) surface (T=300 K). MnPc was sublimated on both 5MLCo/Cu(001) and Cu(001) (1-5 ML; 1ML=4 Å and P= $2 - 3\times10^{-9}$ mbar). X-ray absorption spectra were obtained in TEY mode in XAS chamber at pressure P< 2×10^{-10} mbar. XMCD measurements were performed by reversing the direction of both magnetic field and light's polarity.

The experiments at ESRF were carried out at the ID08 beamline. The samples were prepared in situ using a preparation chamber equipped with a scanning tunneling microscope and low-energy diffraction apparatus. Cu(100) single crystal was used as substrate. It was cleaned by sputtering and annealing at 900 K. MnPc was sublimated (P< 10^{-9} mbar, 1 ML=4 Å) so as to form ultrathin films on Cu(100) or on Co(100) layers epitaxially grown on Cu(001). To perform XMCD, XAS spectra were acquired in total electron yield mode (P< 2×10^{-10} mbar) by reversing both the circular polarity of the photons and the sign of the external magnetic field.

3.2 Spin polarized photoemission

3.2.1 Fundamentals of photoemission

In this section, we describe the basic principle of photoemission spectroscopy. In a photoemission (PE) process, an electron below E_F is excited to a final state above the vacuum level by absorption of a photon. A PE spectra can be obtained by measuring

the kinetic energy (E_{kin}) of the photo-emitted electrons. Because of conservation of total energy [98] we have

$$E_{kin} = h\nu - \phi - E_B \,, \tag{3.4}$$

where '$h\nu$' is the energy of the photon, ϕ the work function of the detector and E_B the binding energy of the photo-emitted electron. Depending upon the nature of the measurement, the initial state of the electron can either be a core level or a valence band. Here, the main focus of the discussion will be on the valence band PE process. During the PE process, the wave vector component parallel to the surface is conserved. This conservation relates the emission angle θ to the parallel component k$_{||}$ of the wave vector [101]

$$k_{||} = (2m/\hbar)^{1/2} E_{Kin}^{1/2} \sin\theta \,. \tag{3.5}$$

Thus according to Eq. (3.5), a measurement of the kinetic energy, the emission angle and the spin of the emitted electrons allow for the determination of the spin resolved band structure of the sample [98]. According to the Fermi's golden rule, the probability of the photoexcitation from the initial state ψ_i to the final state ψ_f is given by [89]

$$w_{fi} \propto |\langle \psi_f(N) \mid \mathbf{A} \cdot \mathbf{p} \mid \psi_i(N) \rangle|^2 \, \delta(E_f - E_i - h\upsilon) \,, \tag{3.6}$$

where N is the number of electrons in the system and E_i and E_f represent the energies of the initial and final state. The operator $\mathbf{A} \cdot \mathbf{p}$ takes into account the interaction between the photon and the electron where $\mathbf{A}$ and $\mathbf{p}$ represent the vector potential of the absorbed photon and the electron momentum respectively. The total PE intensity is related to Eq. (3.6) by

$$I = \sum_{i,f} w_{fi}. \tag{3.7}$$

The matrix element in Eq. (3.6) can be further simplified by using the sudden approximation i.e. an electron is excited instantaneously such that there is a sudden change in potential of the system. Thus the final state function $\psi_f(N)$ can be written as

$$\psi_f(N) \sim \psi_f(N-1)\,\phi_f^k \,, \tag{3.8}$$

where ϕ_f^k is the wavefunction of the photoelectron and $\psi_f(N-1)$ represents the wavefunction of the (N-1) electron system. Similarly the initial state $\psi_i(N)$ can also be factorized into a one electron wavefunction ϕ_i^k and a (N-1) electron wavefunction $\psi_i(N-1)$

$$\psi_i(N) \sim \psi_i(N-1)\,\phi_i^k \,. \tag{3.9}$$

Using Eq. ((3.8)-(3.9)), it can be shown that the total PE intensity is proportional to [102]

$$I \propto \sum_{i,f} \mid M_{i,f} \mid^2 \sum_m \mid c_{m,i} \mid^2 \delta(E_{kin} + E_m^f(N-1) - E_i(N) - h\nu)\,, \qquad (3.10)$$

where $c_{i,m} = \langle \psi_m(N-1) \mid \psi_i(N-1) \rangle$ and $M_{i,f} = \langle \phi_f^k \mid \mathbf{A} \cdot \mathbf{p} \mid \phi_i^k \rangle$. In Eq. (3.10), $\psi_f(N-1)$ is replaced by sum over $\psi_m(N-1)$ states so as to account for all possible excited states. Finally, it should be mentioned that a more complete description of PE process can be obtained within the Green function formalism (see reviews [102, 103] for more information).

3.2.2   Spin polarization measurement

One of the key aspects of spin-resolved photoemission is the measurement of the spin polarization of the photo-emitted electron beam. The measurement of spin-polarization is done through a Mott detector whose working principle is explained in Fig. 3.4. The
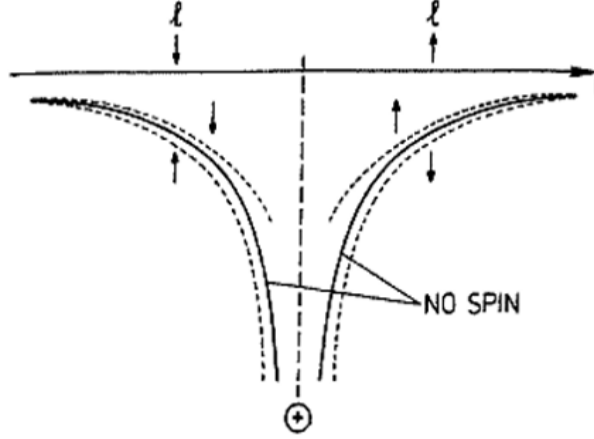
Figure 3.4: Spin dependent scattering from a gold foil arising due to spin-orbit coupling. Potential curves with (dashed) and without (solid) spin-orbit coupling (taken from [101]).

electron beam is scattered from a gold foil and due to spin-orbit coupling, there will be an asymmetry in left and right scattering if the electrons have a spin polarization component (P_n) perpendicular to the scattering plane. In a Mott detector, this asymmetry is measured by two detectors placed symmetrically to the left (L) and to the right (R) with respect to the beam direction. The asymmetry is given by

$$A = \frac{I_L - I_R}{I_L + I_R}\,. \qquad (3.11)$$

The spin polarization P_n of the electron beam is given by

$$P_n = A/S \,, \tag{3.12}$$

where S is the Sherman factor which determines the ability of the Mott detector to distinguish different spins [101]. For spin-polarized photoemission, it is necessary that the sample should be magnetically saturated. This can be done by applying a magnetic field. However, PE experiments are performed in remanence (i.e., the magnetic field is switched off during the measurements). The spin-up ($I^{\uparrow}$) and spin-down($I^{\downarrow}$) spectra can be obtained as follows [101]

$$I^{\uparrow} = \frac{I}{2}(1 + P_n) \ ; \ I^{\downarrow} = \frac{I}{2}(1 - P_n) \,, \tag{3.13}$$

where I is the spin integrated photoemission signal.

3.2.3   Experimental conditions

Experiments were carried out at the Cassiopee beamline of the Soleil synchrotron radiation source. Cu(001) substrates were cleaned through cycles of argon ion etching and annealing in a preparation chamber with a base pressure P = 7×10^{-11} mbar. The clean Cu(001) surface was then covered with 16 epitaxial monolayers (ML) of Co. MnPc was thermally evaporated at P= 7×10^{-10} mbar to form the MnPc/Co(001) interface. Auger electron spectroscopy was used to confirm that the Cu(001), Co(001) and MnPc surfaces are devoid of any contaminants. Samples were then transferred under ultra-high-vacuum conditions to the spin-polarized photoemission chamber. A beam of photons with energy of 20 eV and horizontal linear polarization of the electric field was directed toward the sample at 45°. The experiment is thus sensitive to the hybridization of the Co surface sites with MnPc molecular orbitals (MO) that are both in-plane (σ MO) and out-of-plane (π MO). Photoelectrons were in turn collected by a hemispherical analyzer that integrates a Mott detector for spin detector.

3.3   X-ray standing wave technique

3.3.1   Fundamental principle

X-ray standing wave (XSW) is a powerful tool that allows for the element selective determination of the interface and surface structure. While x-ray standing waves were first observed in 1964 [104], XSW became a mainstream experimental technique only

after the advent of synchrotron radiation.

Fig. 3.5 schematically explains the generation of XSW. As the Bragg condition is fulfilled, the incoming and Bragg scattered x-ray beams interfere. As a result, XSW field is formed whose intensity has the same periodicity as the scatterer planes [105].
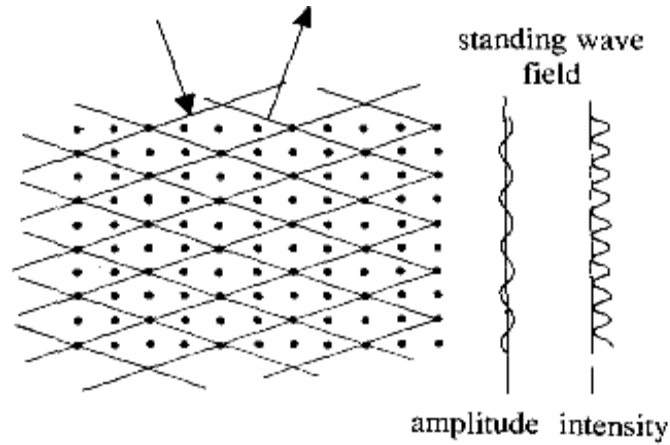
Figure 3.5: Schematic diagram of the x-ray standing waves (XSW) generated by the interference of incoming and Bragg scattered x-ray beams. The intensity of XSW has the same periodicity as that of scatterer planes (taken from [105]).

It can be shown that the intensity arising from the superposition of two coherent traveling x-ray beams can be expressed as [106]

$$I = 1 + R(E) + 2\sqrt{R(E)}\cos(\upsilon(E) - \mathbf{H}\cdot\mathbf{r}),\qquad(3.14)$$

where $R(E)$ is the energy dependant reflectivity and $\upsilon(E)$ is the phase of reflected wave as compared to the incident wave. H is the reciprocal vector associated with scatterer plane spacing (d_H) by relation $H = 2\pi/d_H$. The small phase shift of the forward scattered beam causes the Bragg reflections to extend over a finite energy or angle range [107]. As the width of reflecting curve is scanned (by changing energy in the case of synchrotron source), the phase υ changes by π and consequently the standing waves intensity is shifted by $d_H/2$ [108]. This means that the position of nodes and antinodes in XSW can be moved systematically by changing the phase $\upsilon(E)$. Consequently, the XSW absorption profile of an atom is characteristic of its position relative to the scattering plane since x-ray absorption is proportional to the XSW field intensity.

If the absorption is measured indirectly through photoemission, the photoemission yield $(Y_p(E))$ will be proportional to the XSW field intensity. In case there is a distribution of positions for a given element, the relation of normalized photoemission yield

can be written as (in the dipolar approximation)

$$Y_p(E) = 1 + R(E) + 2\sqrt{R(E)}F_H \cos(\upsilon(E) - 2\pi P_H)\,, \qquad (3.15)$$

where the parameters F_H and P_H are the coherent fraction and coherent position respectively. F_H describes the degree of disorder of the adsorbate element under investigation and the coherent position P_H gives its position with respect to the scatterer planes (modulo d_H). Eq.(3.15) can also be modified to incorporate electric quadrupole transitions (see reviews [105, 106] for more details).

A limitation of XSW technique is the requirement of a perfect crystal [106]. This is because the reflectivity curve has very small width and in case the sample crystal has large mosaicity, the effect of standing waves would be lost [105]. This problem of finite mosaicity can be solved by performing XSW experiments at normal incidence (NIXSW). In the case of normal incidence, the Bragg condition has a turning point and thus the width of reflectivity curves increases considerably [109].

3.3.2   Determination of structural parameters

The structural dependence of the absorption profile is described completely by the coherent fraction F_H and the coherent position P_H. Here we briefly discuss the procedure that is used to obtain these parameters. Both F_H and P_H can be obtained by fitting Eq. (3.15) to the experimental photoemission yield curve. In this work, the software DARE has been used for this purpose [110].

In order to obtain the photoemission yield curve (i.e. right hand side of Eq. (3.15)), photoemission experiments are performed for the energies around the Bragg reflection. The photoemission spectrum for a given energy is fitted with an appropriate function and the area under the peak is calculated which corresponds to $Y_p(E)$ for that particular energy. In our case, one or two components were fitted to photoemission spectra so as to properly describe the chemical shifts of atoms for the element studied. By repeating this procedure for the whole energy range, photoemission yield curve is obtained. According to (3.15), fitting can only be performed if absolute reflectivity $R(E)$ and relative phase $\upsilon(E)$ are known. The DARE programme calculates the $R(E)$ and $\upsilon(E)$ by using the dynamic diffraction theory. The calculated reflectivity curve is then fitted to the experimental rocking curve in order to calibrate the energy scales. Finally the best fitted reflectivity curve is used for fitting the photoemission yield curve.

Chapter 4

Hybrid MnPc/Metal Interfacial Interactions: Theory and Experiment

In this chapter, we describe the chemical and magnetic properties of hybrid MnPc/Metal interfaces. All DFT results discussed here are based on the generalized gradient approximation (GGA) functional. On the experimental side, XAS and XMCD are used to probe the electronic structure and magnetic properties of these interfaces. This chapter is organized as follows. In section 4.1, we study the adsorption of MnPc on Cu(001) and Co(001) through NEXAFS experiments and DFT calculations. In section 4.2 we show that MnPc is magnetically coupled to Co(001) through direct exchange mechanism. We discuss the impact of the interfacial hybridization on the spin polarization at MnPc/Co(001) interface in section 4.3. We finish this chapter by providing a summary of the main results and the conclusions (section 4.4).

4.1   MnPc adsorption on Cu(001) and Co(001)

In this section, we describe the adsorption of MnPc on Cu(001) and Co(001) and ensuing chemical interactions. We discuss the results from NEXAFS experiments that provide the orientation of MnPc molecule on the substrate. We use the determined molecular orientation in the theoretical calculations to find the adsorption mechanism (i.e. physisorption or chemisorption) of MnPc on Cu(001) or Co(001).

4.1.1   Orientation of MnPc: NEXAFS spectroscopy

A crucial aspect of organic thin film growth on metallic substrates is the orientation of molecules. The molecular orientation at the organic/metal interface can affect the charge injection probability and the interface electronic properties [40, 111]. An experimental determination of the molecular orientation is particularly advantageous for the theory (DFT calculation) since otherwise the search for the energetically favorable orientation may be too time consuming.

Realizing the importance of molecular orientation, we found the orientation of MnPc monolayer (1ML) on Cu(001) and Co(001) (for experiments, Co(001) corresponds to 5ML Co/Cu(001)). For this purpose, we performed NEXAFS at Nitrogen (N) K-edge. The results are shown in Fig. 4.1. In MPc molecules, the energy range of π^* and σ^* orbitals is very well defined and therefore N 1s $\rightarrow$ π^* and N 1s $\rightarrow$ σ^* transitions can easily be identified in the N K-edge XAS spectra [40]. The intensity of $\pi^*(\sigma^*)$ transitions depends strongly on the direction of electric field vector of linearly polarized x-rays, being maximum (minimum) when the electric field vector is out of the plane (grazing incidence) and minimum (maximum) when the electric field vector is in the plane (normal incidence) of the molecule. This systematic variation of x-ray absorption intensity with the polarization of light allows for the determination of the molecular orientation. The x-ray absorption spectra for N K edge are shown in Fig. 4.1 for both 1ML MnPc/Cu(001) and 1ML MnPc/Co(001). For both samples, we observe
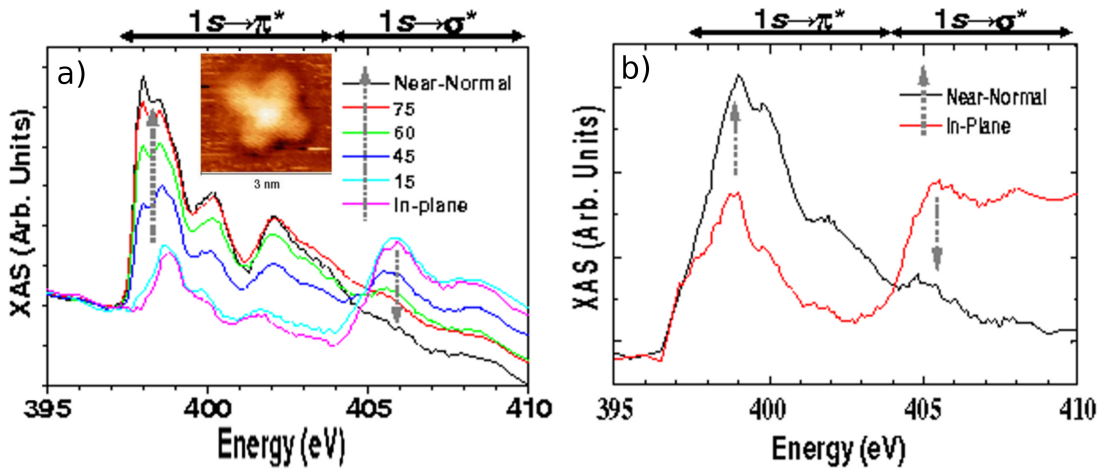

Figure 4.1: N K-edge NEXAFS spectra for the different directions of electric field vector of x-rays with respect to the substrate a) for 1ML MnPc/Cu(001) and b) for 1ML MnPc/Co(001). The horizontal arrows point out the range of N 1s $\rightarrow$ π^* and N 1s $\rightarrow$ σ^* transitions. The inset in a) shows the STM image of MnPc molecule on Cu(001).

similar trend namely the intensity of π^* (σ^*) transition decreases (increases) as we go from grazing incidence to normal incidence with respect to the substrate. Since the polarization is perpendicular to the direction of incidence, this shows that the molecules are oriented parallel to the substrate. This result is consistent with recent NEXAFS studies [40, 41] that also find 1ML MPc molecules to be lying flat on metallic substrates.

A further evidence for flat orientation of MnPc molecules on Cu(001) or Co(001) can be found from the STM experiments [45]. A STM image of MnPc molecule on Cu(001) is shown as an inset in Fig 4.1a. The usual four lobes of MnPc molecule are visible and have the same intensity. This means that the four sides of the Pc ring are about the same distance from the tip and thus the molecule is lying flat above the substrate.

4.1.2   MnPc adsorption mechanism: DFT calculations

Here we provide the theoretical description of MnPc adsorption on Cu(001) and Co(001). In order to determine the adsorption site of MnPc on Cu(001) and Co(001), DFT calculations were performed for ontop, bridge and hollow geometries. For all the calculations, flat orientation of molecules was chosen as determined by the experiment. For both Cu(001) and Co(001), we found that the bridge position was energetically the most favorable. Consequently, all the results discussed in this chapter are based upon the bridge geometry. Fig. 4.2a illustrates the adsorption of MnPc at bridge position on a fcc (001) surface. The adsorption energy (E_a) of MnPc on a metallic slab is calculated as

$$E_a = E_{\mathrm{MnPc/Slab}} - E_{\mathrm{MnPc}} - E_{\mathrm{Slab}} . \qquad (4.1)$$

In Fig. 4.2b, E_a is plotted against the vertical distance between the MnPc molecule and the substrate (the adsorption energy (E_a) curve). Despite having the same adsorption geometry, MnPc has drastically different adsorption distance (corresponding to the E_a curve minimum) on Cu(001) as compared to that of Co(001). On Cu(001), MnPc has an adsorption distance of ~ 3.60 Å whereas for Co(001) the adsorption distance is reduced to 2.25 Å. Another noticeable difference between the two systems is the curvature of the E_a curve. It is evident that the E_a curve for MnPc/Cu(001) is a lot more shallower than that of MnPc/Co(001) indicating that the energetics of adsorption of MnPc on the two surfaces is quite different. This understanding can be further confirmed by the fact that the calculated E_a for MnPc/Co(001) is much higher

(2.20 eV) than that of MnPc/Cu(001) (0.5 eV). Both the calculated adsorption distance and E_a suggest that the interactions responsible for MnPc adsorption on Co(001) are much stronger than that of Cu(001).
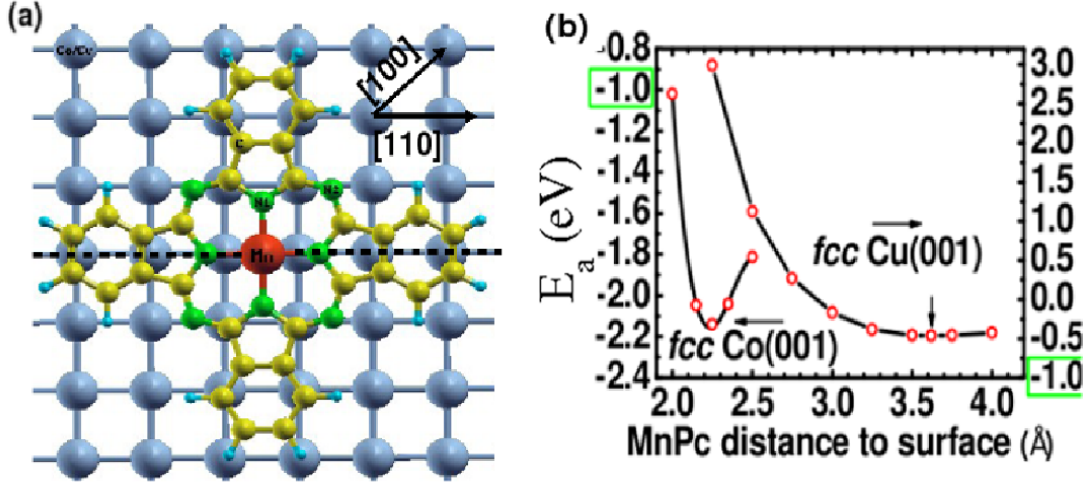
Figure 4.2: MnPc adsorption on Cu(001) or Co(001). a) Adsorption geometry of MnPc on fcc (001) surface. b) Adsorption energy vs MnPc distance to the Co(001) or Cu(001) substrate.

In order to visualize the chemical interactions at the interface, we have calculated the charge density along (110) plane (indicated by the dotted line in Fig. 4.2a) shown in Fig. 4.3. For MnPc/Cu(001) (top panel), the chemical bonding at the interface is very weak since MnPc does not share much charge with the interface Cu atoms. As for MnPc/Co(001)(bottom panel), the charge density contours can be seen propagating from surface Co(001) atoms to MnPc molecule. The presence of charge density contours and charge localization at the interface is a clear indication of covalent bonding at the MnPc/Co(001) interface which is much reduced for that of MnPc/Cu(001).

These results also help us understand why E_a of MnPc/Co(001) is much larger than that of MnPc/Cu(001). Due to the large adsorption distance of MnPc (> 3 Å) on Cu(001), the orbital overlap between the interface Cu(001) and MnPc atoms is very small resulting in a very weak chemical hybridization at the interface. Consequently, the weak dispersive van der Waals (vdW) interactions are responsible for MnPc adsorption on Cu(001), i.e., the GGA calculations without vdW interaction suggest that MnPc is *physisorbed* on Cu(001) surface. For Co(001) surface, much stronger chemical interactions are responsible for MnPc adsorption and therefore the E_a of MnPc/Co(001) is much higher than that of MnPc/Cu(001). Due to the presence of chemical hybridization at the interface, MnPc is *chemisorbed* on Co(001).
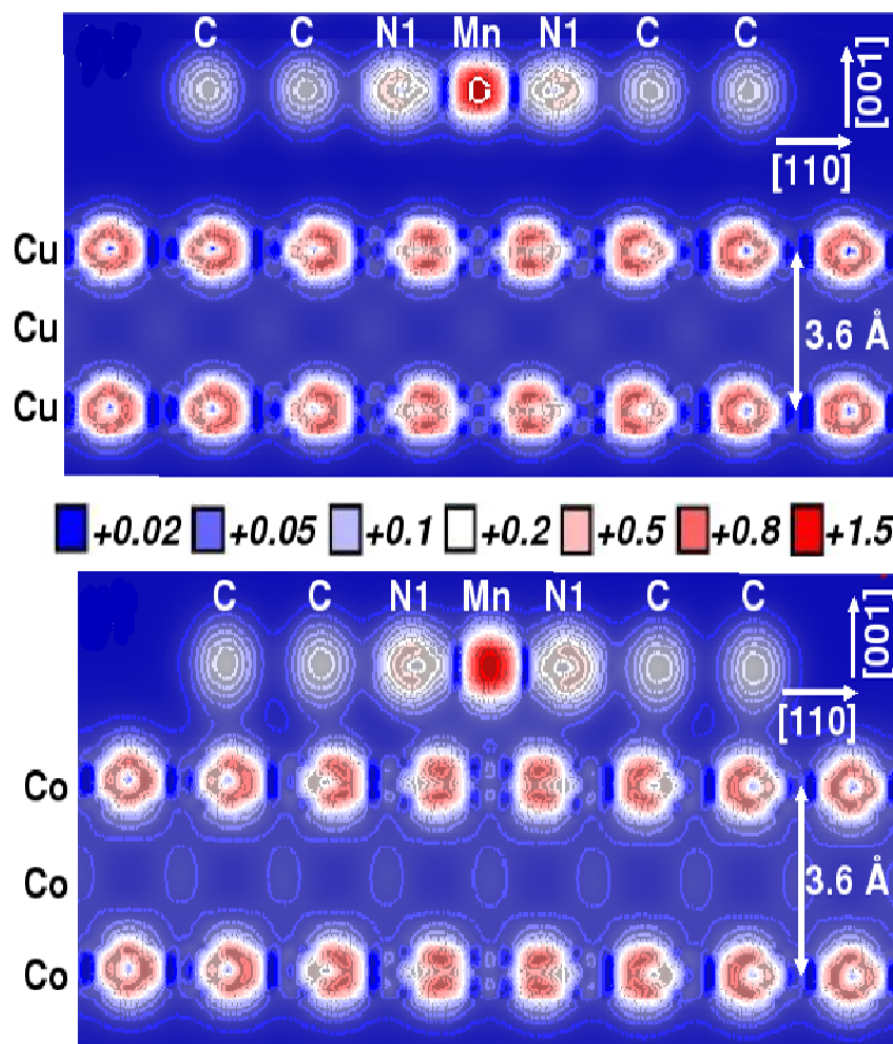
Figure 4.3: Interfacial chemical interactions. Charge density profiles [cut in a (110) plane, along the line shown in panel Fig. 4.2a] for (top) MnPc/Cu(001) and (bottom) MnPc/Co(001) in the plane perpendicular to the substrate.

4.1.3   XAS spectra and calculated PDOS for N

Chemisorption of MnPc on Co(001) means that the molecular orbitals of MnPc would be strongly modified by the interaction with the substrate. This includes not only out of plane π orbitals directly involved in chemical hybridization with Co atoms, but also in-plane σ orbitals. Here we present N K-edge experimental XAS spectra probing either out of plane N 1s $\rightarrow \pi^*$ transitions (Fig 4.4a) [112] or in-plane N 1s $\rightarrow \sigma^*$ (Fig 4.4b). Besides 1ML MnPc, XAS spectra for higher thicknesses of MnPc (2.5 ML MnPc/Cu(001) and 2.3 ML MnPc/Co(001)) are also measured so that the effect of interfacial interactions could be separated from the bulk like features.
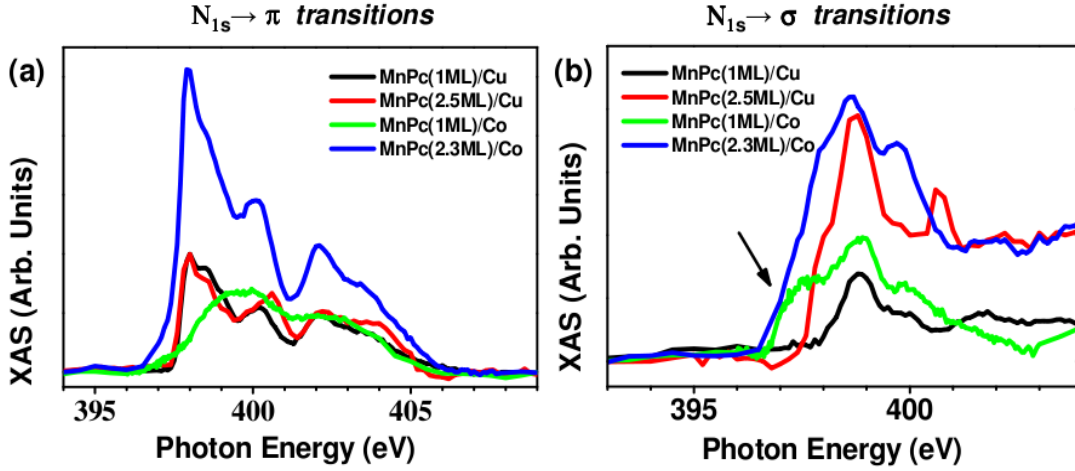
Figure 4.4: Experimental XAS spectra at the N K edge for (1,2.3 ML) MnPc/Co(001) and (1,2.5 ML) MnPc/Cu(001) for a) N 1s → π^* and b) N 1s → σ^* transitions.

For N 1s → π^* transition, we find that the XAS spectra for 1ML MnPc/Cu(001) and 2.5 MnPc MnPc/Cu(001) are similar. This means that the Cu surface atoms do not significantly modify the electronic properties of N sites at the interface and thus chemical interactions at MnPc/Cu(001) interface are weak. These results are in qualitative agreement with the theory (preceding section) that predicts MnPc/Cu(001) system to be physisorbed. Nevertheless, a case for weak chemisorption cannot be ruled out as it will be shown later when vdW interactions are included. We also find that (N 1s → π^*) XAS spectra for the higher thickness of MnPc are similar in shape for both Cu(001) and Co(001). This is expected since for thicker films, the effect of interface interactions are mitigated and XAS spectra consists mostly of bulk like features. However, XAS spectrum probing N 1s → π^* transition for 1ML MnPc/Co(001) is markedly different from that of 2.3 ML MnPc/Co(001). In particular, the XAS spectra for 1ML MnPc/Co(001) is considerably smeared in comparison to 1ML MnPc/Cu(001) with its spectral weight shifted to the center of transition. As for N 1s → σ^* transition, the XAS spectrum for 1ML MnPc/Co(001) is dominated by a pre-edge feature shown by the arrow in Fig. 4.4b . For the higher thickness of MnPc on Co(001), this feature weighs the edge to lower energy by a vanishing contribution. This pre-edge is absent for the case of MnPc/Cu(001). We thus conclude that this pre-edge feature is arising due to MnPc/Co(001) interfacial interactions.

To compare experimental XAS spectra (Fig 4.4) with theory, we calculated the N site resolved partial density of states (PDOS) of σ^* and π^* unoccupied orbitals for MnPc/Cu(001) and MnPc/Co(001) interfaces. The results are presented in Fig 4.5
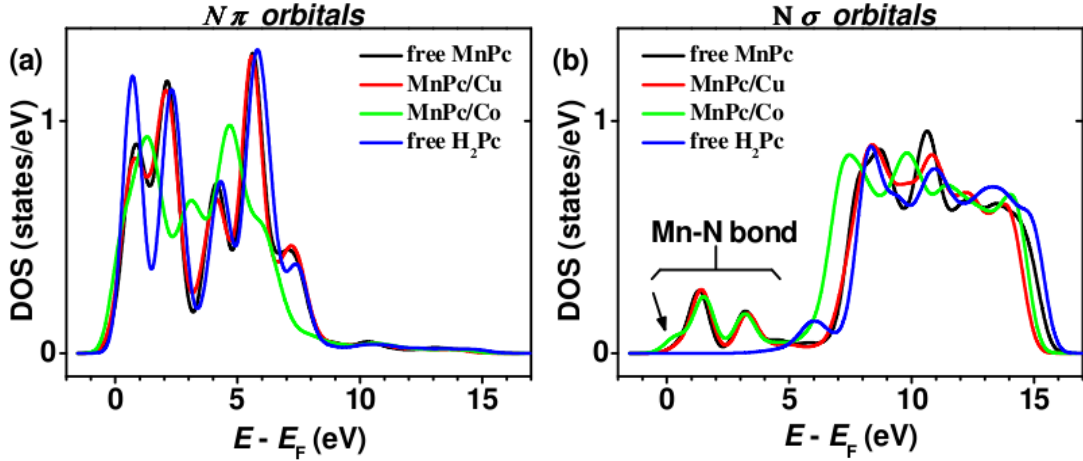
Figure 4.5: Calculated N PDOS for unoccupied a) π^* and b) σ^* orbitals for MnPc/Co(001), MnPc/Cu(001), free MnPc and H_2Pc molecules.

where besides MnPc/Co(001) and MnPc/Cu(001), N σ^* and π^* PDOS for free MnPc and H_2Pc molecules are also shown. A comparison with a metal free H_2Pc N PDOS may help us identify the effect of the central molecular site Mn (i.e. Mn-N bond) on the electronic structure of N in MnPc. Consistent with experiments (Fig. 4.1), we find that N 1s $\rightarrow \pi^*$ transition (Fig 4.5a) precedes the N 1s $\rightarrow \sigma^*$ transition (4.5b). Moreover, the calculated σ^* and π^* N PDOS correctly describe the energetic range of N 1s $\rightarrow \pi^*$ and N 1s $\rightarrow \sigma^*$ transitions. π^* N PDOS of free MnPc molecule and MnPc/Cu(001) are similar due to weak chemical interactions at MnPc/Cu(001) interface. However, π^* N PDOS of MnPc/Co(001) is strongly modified compared to that of free MnPc molecule due to strong chemical hybridization at MnPc/Co(001) interface. Also the spectral tightening of PDOS for MnPc/Co(001) in comparison to MnPc/Cu(001) and free MnPc is in qualitative agreement with the experimental results (see Fig. 4.4a). Except for H_2Pc, all the σ^* N PDOS have two small peaks in a region that is otherwise dominated by N 1s $\rightarrow \pi^*$ transitions. Due to the absence of these peaks in H_2Pc σ^* N PDOS, we attribute this feature to the molecular orbitals arising primarily due to Mn-N in-plane bond. While σ^* N PDOS of MnPc/Cu(001) and MnPc free molecule are essentially the same, an additional feature appears for MnPc/Co(001) around the Fermi level, in line with the experimental observation of a pre-peak structure of σ^* XAS.

The results shown in this section affirm the presence of a strong chemical hybridization at MnPc/Co(001) interface and relatively weak chemical interactions at MnPc/Cu(001) interface. Both experiment and theory show that the chemisorption of

MnPc on Co(001) leads to the modification of in-plane and out of the plane orbitals of MnPc.

4.2   Magnetic coupling at MnPc/Co(001) interface

In this section we discuss the magnetic interactions at MnPc/Co(001) and MnPc/Cu(001) interfaces. Through XMCD experimental results, we show that MnPc(Mn) is ferromagnetically coupled to the Co(001) substrate. Furthermore, DFT calculations provide an insight into the nature of the exchange coupling responsible for the interfacial magnetic coupling.

4.2.1   XMCD measurement for Mn

Fig. 4.6 shows the measured Mn L-edge XAS spectra for right and left circularly polarized x-rays (top panel) and XMCD (bottom panel) for 1ML MnPc/Cu(001) and 0.5 ML MnPc/Co(001). Both XAS and XMCD spectra of MnPC/Cu(001) have fine structure in particular at L_3 edge. In comparison, XAS and XMCD spectra for MnPc/Co(001)
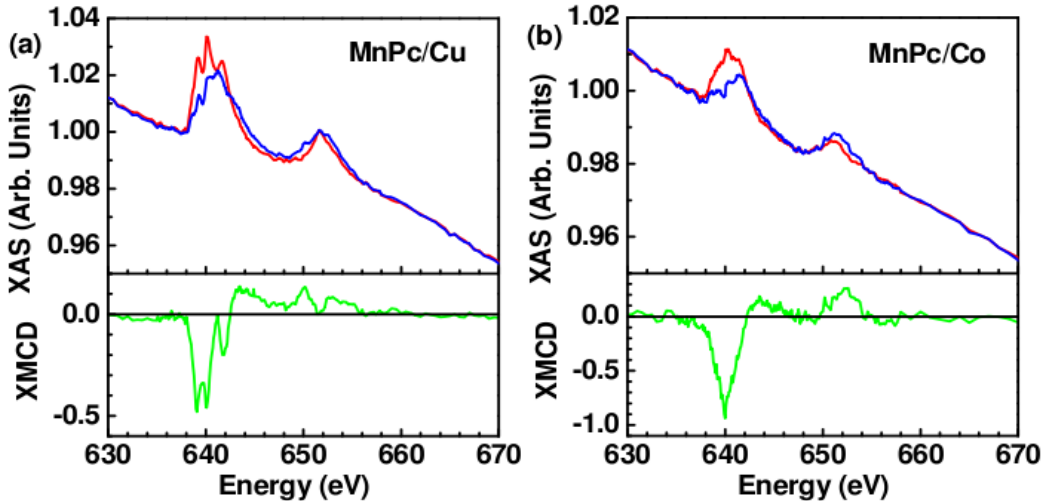
Figure 4.6: XAS spectra for right (red) and left (blue) circularly polarized light (top panel) and XMCD spectra(bottom panel) of Mn for (a) MnPc(1ML)/Cu(001) and (b) MnPc(0.5ML)/Co(001) acquired at T=8K and H=3T with the photon's electric field inclined 60 out of the substrate plane ($\theta = 60°$). XMCD is obtained by normalizing the difference of the XAS spectra for the two polarizations by the edge jump of the isotropic spectra.

are much smoother. This difference can be understood in terms of the strength of hybridization at MnPc/Cu(001) and MnPc/Co(001) interfaces. Owing to weak chemical

interaction at MnPc/Cu(001) interface, free molecular ligand field effects are still dominant and result in the fine structure appearing in Mn L-edge. For MnPc/Co(001), due to the strong hybridization between Mn and Co atoms, multiplet fine structures are considerably smeared and as a consequence both XAS and XMCD spectra look much smoother. We note that for both MnPc/Co(001) and MnPc/Cu(001), the XMCD signal is present. However, MnPc cannot be ferromagnetically coupled to the paramagnetic Cu(001) substrate. Therefore we conclude that the Mn XMCD signal for MnPc/Cu(001) is due to saturated paramagnetism of MnPc since the XMCD experiments are performed at low temperature (T=8K) and high magnetic field (H=3T). A strong modification of Mn XMCD spectra due to Co(001) seems to suggest that MnPc/Co(001) interface is magnetically active and MnPc is magnetically coupled to Co(001) substrate.

To clarify the origin of Mn $L_{2,3}$ XMCD of MnPc/Cu(001) and MnPc/Co(001), we measured the dependence of XMCD signal on the strength of applied magnetic field, i.e., element specific hysteresis loop. In Fig. 4.7 hysteresis loops of Mn for MnPc/Cu(001) and MnPc/Co(001) and for Co(001), recorded at L_3 edge maxima of XMCD are shown. Expectedly, hysteresis loop of MnPc/Cu(001) (Fig. 4.7a) manifests paramagnetic behavior. The hysteresis loop is not saturated even at higher magnetic fields and low temperatures (8K). In sharp contrast, hysteresis loop recorded at room temperature for MnPc/Co(001) (Fig. 4.7b) is a square and coincides with that of Co(001) (Fig. 4.7c). This means that the orientation of Mn spin is determined by the ferromagnetic Co(001) substrate. Furthermore, the magnetization of Mn switches in the same way as that of Co. We therefore conclude that Mn(MnPc) is ferromagnetically coupled to Co(001). This is one of the main results of this work and it underscores the impact of magnetic interactions between ferromagnetic substrate and the adsorbed metal-organic molecule.

4.2.2 Interfacial electronic structure: DFT calculations

Here we present the spin-polarized PDOS of MnPc/Cu(001) (Fig. 4.8a) and MnPc/Co(001) (Fig. 4.8b). For comparison, Mn PDOS for free MnPc molecule is also shown. Due to physisorption of MnPc on Cu(001), we expect that the electronic structure of MnPc would not change significantly from that of a free molecule. Indeed Mn PDOS on Cu(001) is similar to that of a free MnPc. However, the electronic structure of MnPc is strongly modified due to the influence of Co(001) substrate. The effect of interfacial chemical hybridization is evident by the shape of Mn majority spin PDOS that resembles the corresponding PDOS of Co(001), while the minority spin PDOS is also
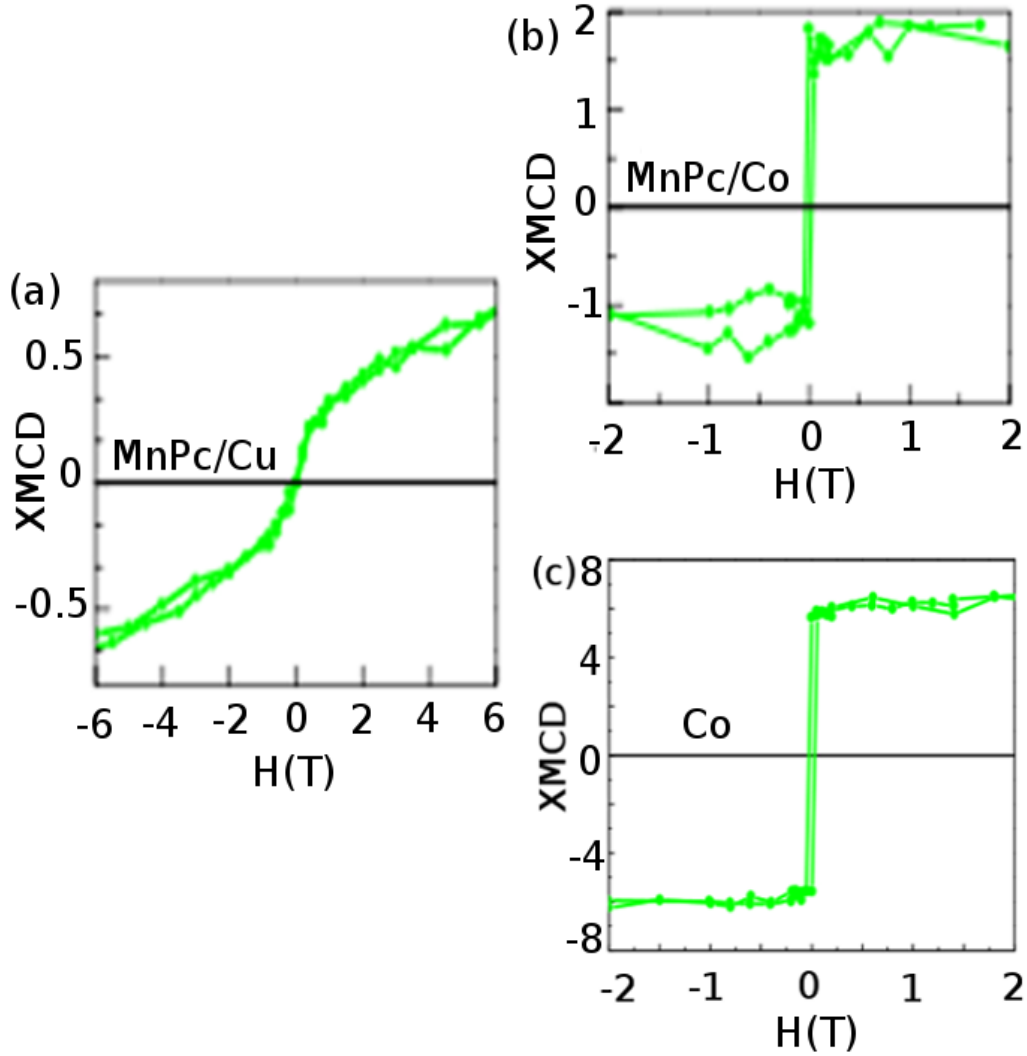
Figure 4.7: Element specific hysteresis loop (i.e. XMCD as function of H)) of Mn at L_3 edge (E=640 eV) for a) 2.5 ML MnPc/Cu(001) (8K), b) 1ML MnPc/Co(001) (300K) and c) hysteresis loop for L_3 edge of Co(001)(5ML Co/Cu(001)) (8K).

broadened. Since the magnetism in MnPc is essentially driven by Mn d orbitals, strong modification of Mn PDOS due to Co should also affect the magnetic properties of MnPc. Therefore, the calculated spin moment of the Mn site of MnPc on Cu(001) is the same as that of the free molecule (3.74 μ_B), while on Co(001), the Mn magnetic moment is reduced to 2.90 μ_B. Similar reduction of magnetic moment has also been observed for MnPc on Au(111) [52] and CoPc on Cu(111) [6, 57].

Another important consequence of strong interfacial hybridization of MnPc/Co(001) is the creation of interface states near E_F in majority spin channel shown in the inset
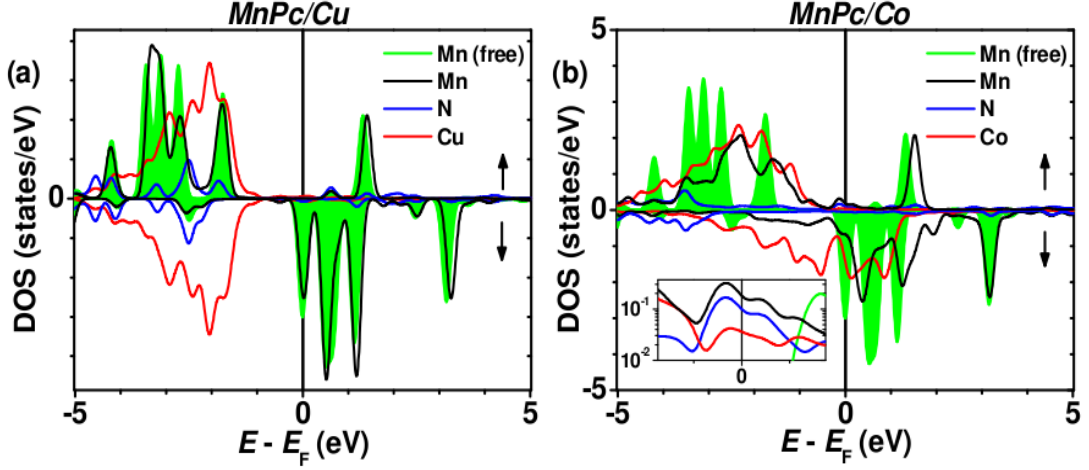
Figure 4.8: The spin-polarized PDOS of Mn, N and interface layer of the substrate (Co(001) or Cu(001)) for (a) MnPc/Cu(001) and (b) MnPc/Co(001). Mn PDOS for MnPc molecule is also provided for comparison. The inset in panel (b) provides the magnified image of the the majority-spin PDOS of MnPc/Co(001) near the Fermi level in the log scale.

of Fig. 4.8. For free MnPc and MnPc/Cu(001), no states are present in the majority spin channel at E_F as it lies between the HOMO-LUMO energy gap. However Co induces spin-polarized states at E_F not only on Mn but also on Pc ring (see N PDOS in the inset). Since the electrons at the vicinity of E_F contribute to charge and spin transport, the substrate induced states can strongly influence the transport properties of MnPc molecules.

The orientation Mn and Co spin is better revealed by the magnetization density isosurface plot shown in Fig. 4.9. No significant magnetization is observed in MnPc expect for Mn (Mn position corresponds to the lobe of ↑ (red) spin magnetization density). There is nevertheless a small ↓ (blue) spin magnetization on nearest N from Mn, while second nearest N and some C atoms have small ↑ magnetization towards Co. Most crucially both Mn and Co have their magnetization oriented in the same direction consistent with the XMCD results already discussed.

4.2.3   Exchange coupling mechanism

While we have confirmed the presence of interfacial magnetic coupling, the exchange mechanism responsible for it is not yet discussed. Here we identify the nature of exchange mechanism that magnetically couples Mn with the ferromagnetic Co substrate. First, we note that MnPc is chemisorbed on Co(001). This means there is a significant orbital overlap of the interface Co and MnPc atoms. The direct chemical hybridization
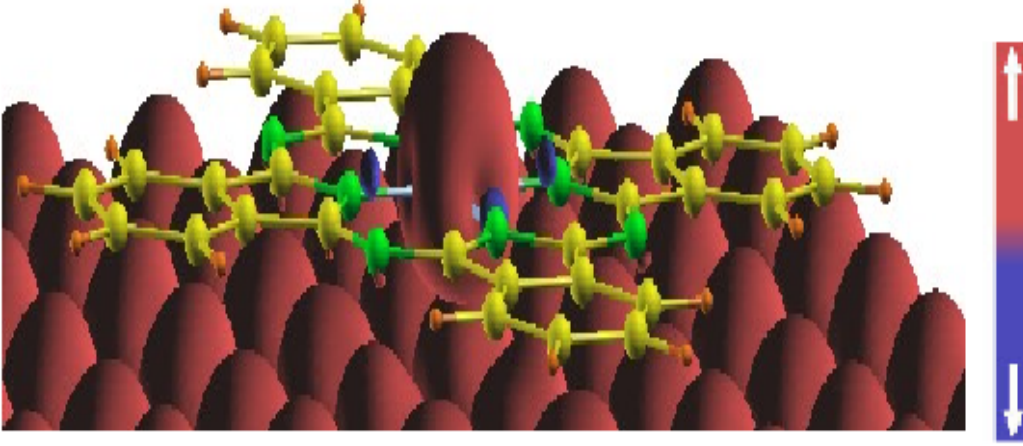
Figure 4.9: Isosurface plot of magnetization density of MnPc on Co(001). The red represents spin up while blue represents the spin down as indicated by the arrows. Green, yellow and orange spheres represent N, C and H respectively

between Co and Mn can be confirmed by interfacial charge density plot (Fig. 4.3) and calculated PDOS (Fig. 4.8). Second, since MnPc is adsorbed on Co(001) in the bridge position with adsorption distance of ~ 2.25 Å , the distance between Mn and the first Co neighbor is around 2.58 Å, which is close to the nearest neighbor distance of Co. Both these factors indicate that the direct exchange is mainly responsible for the ferromagnetic coupling between MnPc and Co(001). It may however be noted also that MnPc adsorption at the bridge position should also be helpful in promoting indirect 90° superexchange according to Goodenough-Kanamori rules [57]. Nevertheless, in the presence of strong overlap of 3d orbitals of Mn and Co, the direct exchange must be the dominant mechanism promoting the interfacial ferromagnetic coupling.

Some previous studies have also identified direct exchange as a possible origin of the coupling mechanism [7, 57]. However, this result is in contradiction with a previous study of Fe-OEP/Co(111) interfacial ferromagnetic coupling [8] where the exchange mechanism was attributed to the indirect 90° superexchange due to large (~ 3.60 Å) Fe-OEP adsorption distance on Co(111).

4.3   Chemical hybridization at E_F: role of Mn

A well know fact about inorganic magnetic tunnel junction is that the relevant spin polarization for the TMR is not that of bulk ferromagnet but the spin polarization at inorganic/ferromagnetic interface [33]. In this section, we describe the impact of interfacial orbital hybridization on the spin polarization at the MnPc/Co(001) interface.

For this purpose, the local density of states (LDOS) in the vicinity of E_F is calculated. To understand the role of the central molecular site, i.e., Mn in defining the spin polarization at the interface, a comparison with (metal-free phthalocyanine)H_2Pc/Co interface is also provided.

4.3.1   Adsorption of H_2Pc on Co(001)

Here for completeness, we briefly describe the adsorption of H_2Pc on Co(001). Similar to MnPc, calculation were performed for the bridge, hollow and ontop adsorption sites of fcc(001) Co surface, while molecular orientation on Co(001) was chosen to be flat as determined by the experiment [45]. However unlike MnPc, we found that the hollow site was energetically most favorable. Therefore all the results discussed in this section are based upon the hollow geometry of adsorption.

In Fig. 4.10, the total energy is plotted as function of the vertical distance of H_2Pc from Co(001) surface. The zero of the energy scale corresponds to the minimum total energy value, i.e., the equilibrium adsorption distance. Similar to MnPc, the adsorption distance of H_2Pc on Co(001) is $\sim$ 2.20-2.25 Å. Due to small adsorption distance and therefore strong orbital overlap of interface H_2Pc and Co atoms, H_2Pc is chemisorbed on Co(001). A further evidence of the chemisorption of H_2Pc will be provided in the following discussion on the LDOS of MnPc/Co(001) and H_2Pc/Co(001) interfaces.
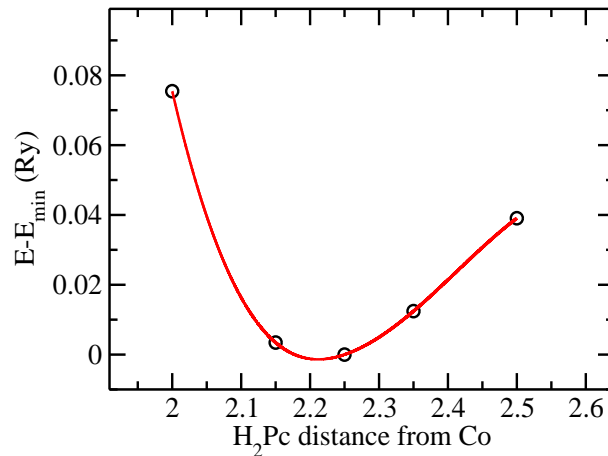

Figure 4.10: Calculated total energy of H_2Pc/Co(001) plotted as a function of the vertical distance between H_2Pc and Co(001) substrate. The energy scale is shifted such that the zero corresponds to minimum total energy value.

4.3.2   LDOS at E_F

LDOS of MnPc/Co(001) over the energy range $E_F < E < E_F+0.15$ eV is shown in Fig 4.11. This energy range is relevant for the electronic transport and corresponds to the interface states created near E_F due to the hybridization of MnPc and Co(001) surface, as shown in the inset of Fig. 4.8. For the majority spin channel (top panel as indicated by ↑), Co hybridizes not only with Mn but also with atomic sites of Pc ring (i.e. N, C). However for the minority spin channel (bottom panel indicated by ↓, notice that the scale is an order of magnitude higher than the majority channel), the main contribution to the DOS comes from the metallic bridge between Co and Mn. This is understandable since Mn, being a 3d metal has more states in the minority spin channel at the Fermi level as compared to the majority spin states. It is clear that MnPc hybridizes differently with Co in the two spin channels.

To elucidate further the impact of Mn on the interface spin polarization, we present in Fig. 4.12 the LDOS for H_2Pc/Co(001) calculated for the same energy range as that of MnPc/Co(001). For spin-up channel, Co hybridizes mainly with C and N similar to the case of MnPc/Co(001). Nevertheless, the shape of the spin-up LDOS for the two cases is different due to different adsorption geometry of MnPc and H_2Pc on Co(001). The effect of the absence of metallic site is most telling for the spin-down channel. We find that there is no hybridization between the interface H_2Pc and Co atoms and the contribution of Pc ring to the DOS in the minority spin channel is negligible.

A comparison of the LDOS of H_2Pc/Co(001) and MnPc/Co(001) demonstrates clearly that N and C atoms in Pc ring couple to Co(001) surface mainly in the majority spin channel and for the minority spin channel, their contribution is negligible. Conversely, the contribution to the minority states comes from the Mn 3d states that are hybridized to Co. The impact of this bonding scenario on the interface spin polarization (P_{int}) is explained in Fig. 4.11c. For H_2Pc/Co(001) , H_2Pc couples to Co only in the majority spin channel through weak hybridization between Co and N, C sites and therefore the spin polarization at the interface will be positive ((P_{int}) > 0). For MnPc/Co(001), there will be a competition between the two spin channels (spin ↑ dominated by C and N while spin ↓ by Mn) to define the sign and amplitude of P_{int}. Thus similar to the case of inorganic spintronics, the hybridization at the interface plays a crucial role in determining the P_{int} at E_F.
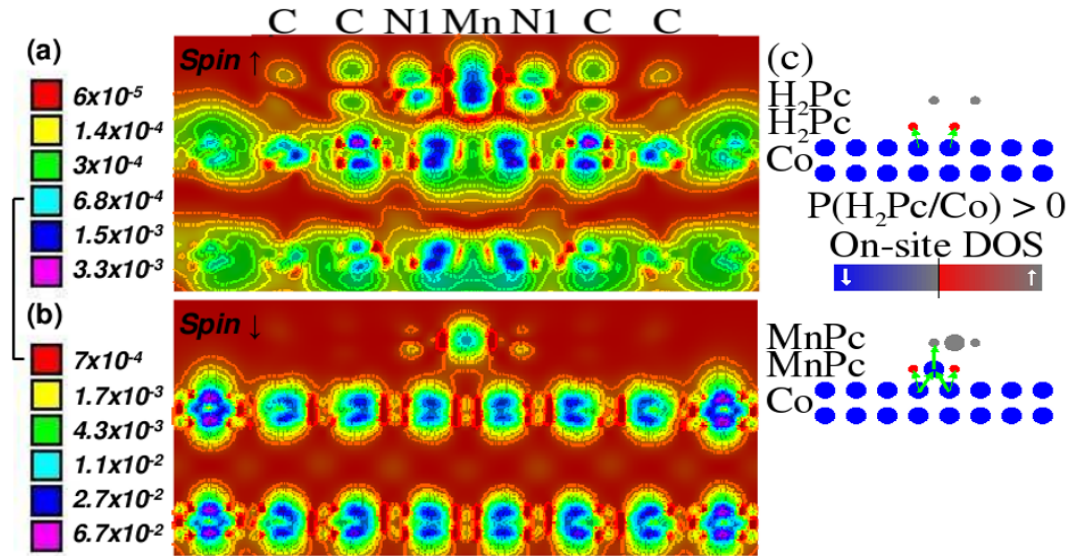
Figure 4.11: Spin-resolved LDOS at $E_F < E < E_F+0.15$ eV of MnPc/Co(001) for spin a) up
(↑) and b) down (↓). The plot is for (011) plane (see Fig. 4.2 for more details). c) The impact
of hybridization in different spin channels on spin injection is schematized for MnPc/Co(001)
and H₂Pc/Co(001). The green arrows indicated the wavefunction hybridization between Co
and MnPc/H₂Pc.
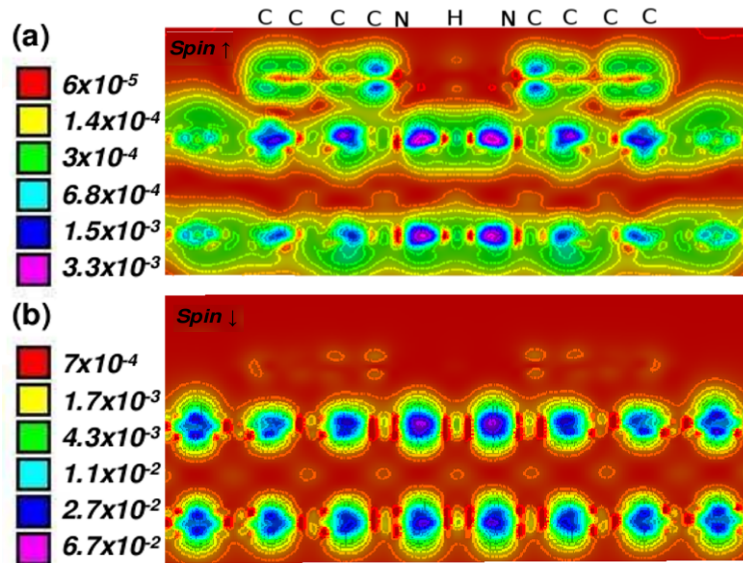
Figure 4.12: Spin-resolved LDOS at $E_F < E < E_F+0.15$ eV of H₂Pc/Co(001) for spin a) up
(↑) and b) down (↓).

4.4   Conclusion

In this chapter we have described the chemical and magnetic properties at MnPc/Cu(001) and MnPc/Co(001) interfaces. The molecular orientation determined from NEXAFS spectroscopy measurements is found to be planar on both surfaces and used as such afterwards in all the theoretical calculations based on DFT (within GGA).

DFT calculations show that MnPc is chemisorbed on Co(001) but physisorbed on Cu(001). Experimental confirmation of the chemisorption of MnPc is provided by measured σ^* and π^* N XAS spectra that show a strong modification of both in-plane and out of plane orbitals of MnPc.

XMCD measurements find MnPc to be magnetically coupled to Co(001) substrate. Furthermore, the calculated electronic structure shows that there is a strong hybridization between Mn and Co. Therefore, owing to the small adsorption distance and strong orbital overlap of Mn and Co, we conclude that the mechanism for the interfacial magnetic coupling is direct exchange.

LDOS calculations in the vicinity of E_F demonstrate that for majority spin, Co hybridizes mainly with N and C sites (Pc ring) while the interaction of Mn 3d states and Co dominates the minority spin channel. Therefore the interface spin polarization at E_F is determined by the competition between a net positive spin polarization at N and C sites induced due to the hybridization with Co and negative spin polarization at Mn. Thus, in the absence of 3d metal in phthalocyanine (i.e. H_2Pc/Co), spin polarization at the interface is positive.

The results described above identify clearly the chemical bonding at the interface as the main reason for the drastically different properties of MnPc/Co(001) and MnPc/Cu(001) interfaces. However, the impact of interfacial hybridization goes beyond the expected modification of molecular orbitals due to chemisorption. We have shown that the magnetic properties of MnPc are also driven by the chemical interactions with Co(001) substrate through direct exchange mechanism. Our results also affirm the presence of 'spin dependant interfacial hybridization' [5] at MnPc/Co(001) interface. The hybridization of Co(001) with MnPc is strongly spin dependant, with C, N hybridizing mainly with Co in the majority spin channel while the Mn-Co hybridization dominate the minority spin channel. Furthermore the spin polarized N and C states present at E_F are the interface states induced by the hybridization of MnPc and Co.

It is important to highlight the good agreement between the experimental results and the DFT calculations, and that the key parameter that determines the strength of

the interfacial interactions is the molecular adsorption distance. However since the calculations are based on GGA, the weak vdW interactions are not properly taken into account. A more precise determination of adsorption distance necessitates the inclusion of vdW interactions particularly for weakly interacting interfaces such as MnPc/Cu(001). The Impact of vdW interactions on the adsorption of MnPc on Cu(001) or Co(001) surfaces will be the subject of the next chapter.

Chapter 5

Impact of the vdW Interactions on MnPc Adsorption and Interfacial Electronic Properties

In the previous chapter, the GGA functional was used to describe MnPc/metal interfacial properties. Here we seek to further improve the theoretical description of these interfaces by including vdW correction to the GGA functional by employing dispersion correction (GGA-D method in DFT-D2 version) developed by Grimme [12]. The details of this method are already discussed in Chapter 2. This chapter is organized as follows. In section 5.1, we discuss how the GGA adsorption distances are modified by the vdW interactions. Theoretically, an important aspect of the molecular adsorption on metallic surfaces is the subsequent structural relaxation of the molecule and the metallic slab. Consequently, we have performed the geometry optimization of MnPc-metal system including also the vdW forces. In section 5.2, we describe the effect of the geometry optimization on the structural, electronic and magnetic properties of MnPc/Cu(001) and MnPc/Co(001) interfaces. In section 5.3, we study the electronic properties of MnPc/metal interfaces with the focus on the interface dipole and the metal work function change due to MnPc adsorption. We point out various factors that can influence the magnitude and sign of the metallic work function change. In Section 5.4 we present the results of XSW experiments, used to determine the MnPc adsorption distance on Cu(001). We finish this chapter by providing a summary of the main results and the conclusions.

5.1 Adsorption distance and adsorption energy

In this section, we investigate the changes brought to the adsorption distance and to the adsorption energy (E_a) of unrelaxed MnPc/Cu(001) and MnPc/Co(001) when the vdW interactions are taken into account. We will also study the subsequent change in the chemical interactions at the interface.
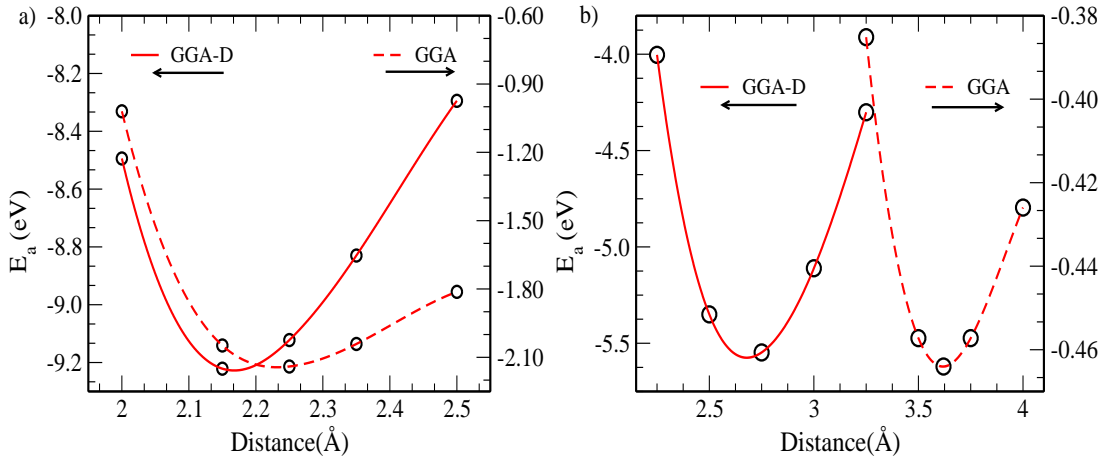
Figure 5.1: The adsorption energy (E_a) of MnPc plotted against the vertical distance between MnPc and a) Co(001) and b) Cu(001). The solid and dashed red curves represent the calculations with (GGA-D) and without (GGA) vdW interactions, respectively. The corresponding scales are shown by the arrows.

The effect of the vdW interactions on MnPc adsorption on Cu(001) or Co(001) is summarized in Fig. 5.1 where MnPc E_a computed with GGA-D (red, solid line) is plotted as a function of MnPc vertical distance with respect to the two surfaces. For comparison, the corresponding results from the GGA calculations are also reported (red, dashed line). Note that GGA-D calculations find bridge position to be energetically most favorable adsorption site for MnPc on Cu(001) or Co(001), consistent with GGA results. For MnPc/Co(001) (Fig. 5.1a), the vdW interactions bring only a small change to the adsorption distance (~ 0.1 Å). This is understandable since MnPc is chemisorbed on Co(001) and therefore the effect of weak vdW interactions is relatively small. In sharp contrast, the adsorption distance of MnPc on Cu(001) is changed drastically. As shown in Fig. 5.1b, from a value of ~ 3.60 Å calculated from GGA, the adsorption distance becomes ~ 2.65 Å. We thus observe a decrease of ~ 1 Å of adsorption distance due to vdW interactions.

In contrast to the adsorption distance, MnPc E_a calculated with GGA-D on both Cu(001) and Cu(001) is markedly different from that of GGA. The E_a of MnPc on

Co(001) is increased from 2.20 eV to 9.25 eV due to the vdW interactions despite the fact that the adsorption distances computed using GGA and GGA-D are almost the same. A more stark change is observed for MnPc on Cu(001) where E_a computed form GGA-D has a value of 5.55 eV, more than 10 times the value found using GGA. This sharp increase in E_a is concomitant with the sharp decrease in the adsorption distance. We thus conclude that the vdW interactions markedly change the adsorption energetics of MnPc on Cu(001) or Co(001). However, the effect of the vdW interactions is more pronounced for MnPc/Cu(001) since the attractive vdW interactions besides increasing the adsorption energy, also bring MnPc much closer to Cu(001) surface in comparison to GGA. To show the impact of the vdW interactions on the interfacial
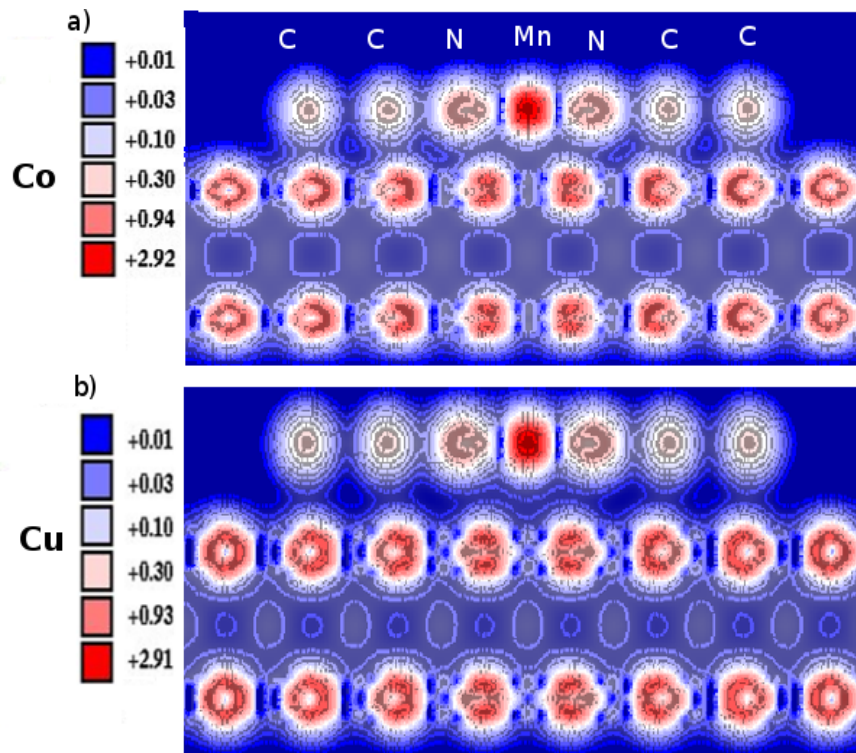
Figure 5.2: Charge density plot along (011) plane of a) MnPc/Co(001) and b) MnPc/Cu(001) interface for the adsorption distance calculated after including vdW interactions. (see Fig. 4.3 for more details about the plane of plot).

chemical properties, we depict in Fig. 5.2 the charge density plot for MnPc/Cu(001) and MnPc/Co(001) interfaces computed for the adsorption distance determined using GGA-D. For MnPc/Co(001) (Fig.5.2a), we observe a strong chemical hybridization at the interface comparable to that of GGA (see Fig. 4.3 for comparison). As for

MnPc/Cu(001) (Fig. 5.2b) charge contours propagating from the interface Cu atoms to MnPc can be seen clearly indicating the presence of chemical hybridization at the interface. Even though the chemical interaction at MnPc/Cu(001) interface found with GGA-D is much weaker as compared to that of MnPc/Co(001), it is evidently at odds with the results of GGA which describe MnPc to be physisorbed to Cu(001). Thus a sharp decrease (~ 1 Å) in adsorption distance of MnPc on Cu(001) makes the orbitals of the interface Cu and MnPc atoms overlap by promoting chemical hybridization at the interface. Therefore MnPc described to be physisorbed by GGA, becomes weakly chemisorbed due to the vdW interactions. This remarkable result, along with the drastic increase in the adsorption energies of MnPc/Cu(001) and MnPc/Co(001) underscores the effect of vdW interactions on the adsorption of phthalocyanine molecules on metallic surfaces.

5.2 Structural relaxation with vdW forces

In this section, we will describe the effect of structural relaxation of MnPc-metal system on the MnPc adsorption and interfacial structural and electronic properties. The structural relaxation is performed by VASP code. All the calculations are performed using DFT-D approach to account for the vdW forces during the geometry optimization.

5.2.1 Atomic relaxation of MnPc/metal interface

Here we describe the structural changes brought to the MnPc-metal system due to atomic relaxation. During the geometry optimization, MnPc molecule and two top surface layers were allowed to relax while the third surface layer was held fixed. In Fig. 5.3, we show the optimized geometric structure of MnPc on Cu(001) or Co(001). For more detailed understanding of the structural variation due to relaxation, both top and side views of MnPc-metal systems are presented in Fig. 5.3. During the relaxation, MnPc or the substrate atoms that are lying in the same plane prior to relaxation, can be vertically displaced from each other. Therefore the vertical distance between MnPc and substrate is defined as the distance between the topmost atom of the first surface layer and Mn. According to this definition, the adsorption distance of MnPc on Co(001) and Cu(001) is found to be ~ 1.90 Å and ~ 2.35 Å respectively (see 5.2.2 for a detailed discussion).

The top view for both MnPc/Co(001) (Fig. 5.3a) and MnPc/Cu(001) (Fig. 5.3b) show that MnPc is adsorbed at the bridge geometry. Thus the adsorption site of MnPc is not changed due to atomic relaxations. The atomic relaxations also do not result

in any significant lateral (i.e. in xy plane) displacement of MnPc atoms from each other. The side view for both systems however indicates that the geometry of MnPc molecule is distorted due to adsorption as the atoms of MnPc are vertically displaced (i.e. along z-axis, see Fig. 5.3) from each other during the geometry optimization. The vertical displacement of MnPc atoms on Cu(001) or Co(001) is quantified in the top view of Fig. 5.3 where the position of Mn is chosen as the reference to calculate the vertical displacement of other atoms. The structural variation of two (out of four) lobes are shown since the other two lobes are equivalent due to the symmetry of the MnPc molecule, adsorbed at the bridge position on a fcc(001) surface.

The vertical displacements of MnPc atoms on Co(001) are strongly site dependant. Generally, a considerable depression of benzopyrrole groups is observed. On the other hand, H atoms are strongly elevated as compared to Mn, whereas N atoms are in an intermediate situation. Evidently, MnPc molecule is distorted due to chemisorption on Co. Furthermore, C atoms in the benzopyrrole groups play a significant role in the chemisorption as indicated by the reduction of Co-C distance during the relaxation. They promote the chemical hybridization between benzopyrrole groups and Co. Similar to MnPc/Co(001), the vertical displacements of MnPc on Cu(001) are also site dependent. Interestingly, one of the benzene rings is depressed while the other is elevated as compared to Mn. H atoms are elevated, though by smaller amount in comparison to MnPc/Co(001). Generally, the structural distortion of MnPc is relatively smaller than that of MnPc/Co thus indicating a weaker interfacial chemical interactions as compared to MnPc/Co(001). This is because the adsorption distance obtained after relaxation for MnPc/Cu(001) is much larger as compared to that of MnPc/Co(001).

The Co(001) and Cu(001) surfaces are also effected by atomic relaxations, namely the two top surface layers involved in the geometry optimization show a small contraction. The first and second surface layers of Co are on average displaced by ~ 0.31 Å and ~ 0.16 Å respectively below their unrelaxed (i.e. bulk) positions. The contraction is smaller for Cu as the first and second surface layers are lying on average ~ 0.07 Å and ~ 0.03 Å below their bulk unrelaxed values.

5.2.2   Total energy curve

In Fig. 5.4, the optimized atomic positions acquired from the structural relaxation are used to obtain total energy as a function of the vertical distance between MnPc and Cu(001) or Co(001) substrates. Besides VASP, the dependence of total energy on the MnPc-substrate distance has also been computed by PWSCF. The good agreement between the calculations from VASP and PWSCF (see Fig. 5.4) show that the results
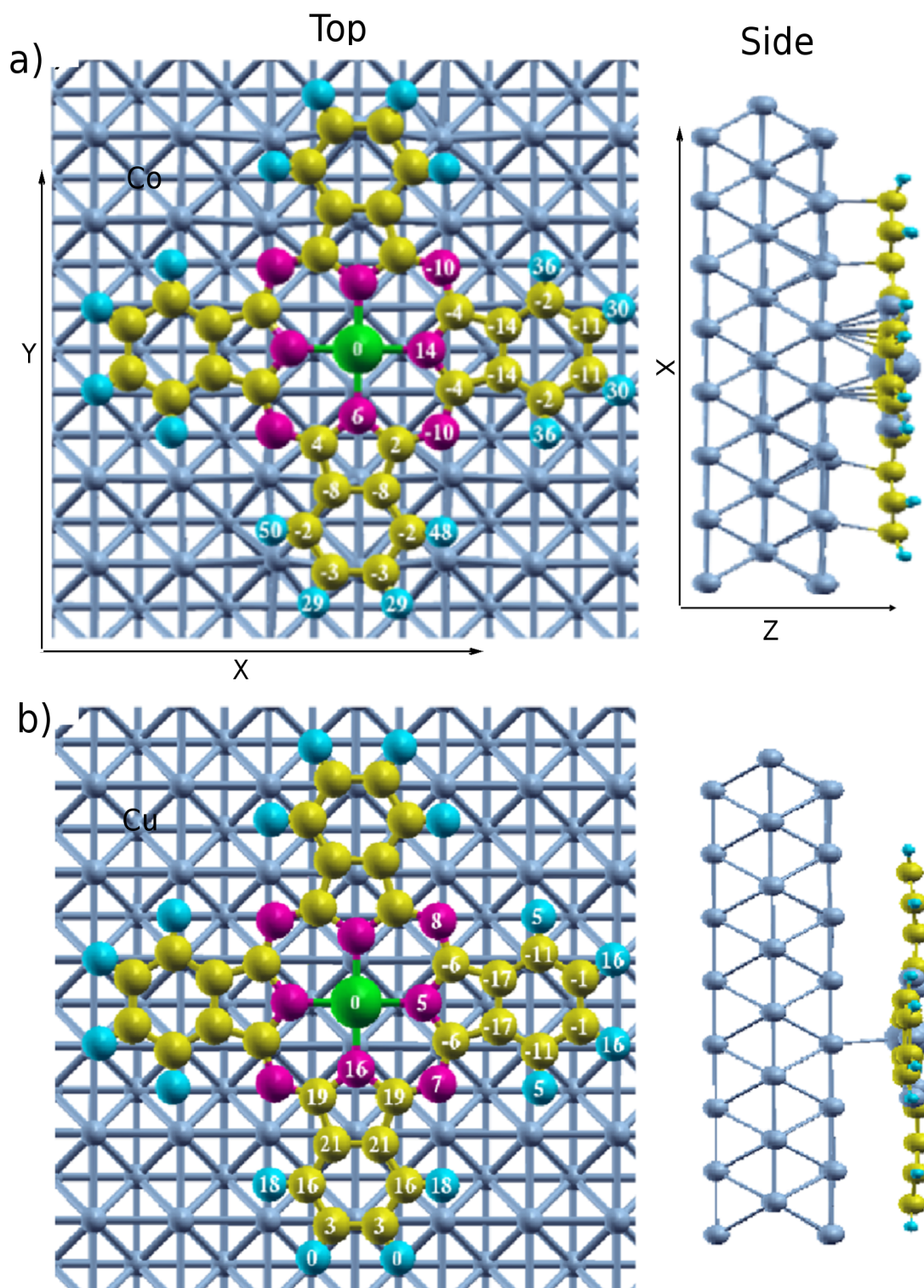
Figure 5.3: Top and side view of the relaxed structure obtained from the GGA-D method for MnPc on a) Co(001) and on b) Cu(001) . In the figure, green, red, yellow and blue spheres represent Mn, N, C and H respectively. In the top view, the vertical displacements (with respect to Mn, scale: 10^{-2} Å) of MnPc atoms due to atomic relaxations are also shown.

are independent of methodology used and are thus reliable.

The adsorption distance of MnPc on Co(001) (as defined above) is ~ 1.90 Å (Fig. 5.4a). For MnPc on Cu(001) ((Fig. 5.4b), the adsorption distance is ~ 2.35 Å. Besides the smaller adsorption distance of MnPc on Co(001), the energy scale of MnPc/Co(001) shown in Fig. 5.4a is almost an order of magnitude larger than that of MnPc/Cu(001). Thus the strength of the adsorption of MnPc on Co(001) is much stronger than that of MnPc/Cu(001). In comparison to the unrelaxed DFT-D calculations (Fig. 5.1), the adsorption distances obtained after relaxation are reduced. This is because during the relaxation Mn (which is chosen to be the reference for the calculation of adsoption distance) comes much closer to the surface as compared to H and the nearest N.

Expectedly, the relaxation is energetically more favorable as indicated by the increase in the adsorption energy of relaxed MnPc/Co(001) and MnPc/Cu(001) as compared to those of the unrelaxed caculations. The E_a is increased from ~ 9.25 eV to 11.50 eV for MnPc/Co(001) and from ~ 5.55 eV to 5.75 eV for MnPc/Cu(001). While these values are in the correct range in comparison to the previously computed values of E_a from GGA-D method for phthalocyanine/metal systems [53, 113], it should be emphasized that DFT-D method has the tendency to overbind the metallic systems [83].
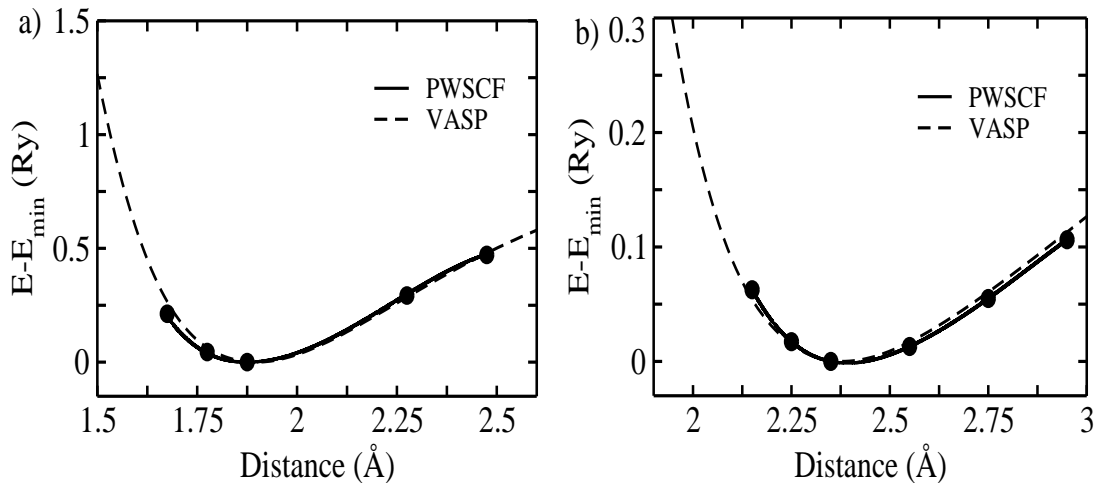
Figure 5.4: Computed total energy as a function of the vertical distance between MnPc and a) Co(001), b) Cu(001). The zero of the energy scale corresponds to the total energy minimum value. Solid black lines represent the calculations performed by PWSCF, while the corresponding dashed line represent the calculations performed by VASP.

5.2.3   Electronic structure of relaxed MnPc/Metal interface

Here we will explore the changes brought to the interfacial chemical hybridization and interfacial electronic structure due to atomic relaxation with the vdW interactions.

In Fig. 5.5, we present the charge density plot along the (011) plane (top panel) and the PDOS (bottom panel), calculated for the relaxed MnPc/Co(001) (Fig. 5.5a) and MnPc/Cu(001) (Fig. 5.5b). The charge density plot shows strong chemical hybridization at MnPc/Co(001) interface, consistent with the unrelaxed GGA (Fig. 4.3) and GGA-D (Fig. 5.2) results. Consequently, the PDOS of MnPc is strongly modified due to the strong hybridization with Co. Also the PDOS for Mn and N are more strongly broadened in comparison to those calculated using GGA (Fig. 4.8). This larger broadening is the result of stronger chemical hybridization at MnPc/Co(001) interface arising due to the vdW interactions that reduce the adsorption distance of MnPc on Co(001) as compared to the one found with GGA. As a consequence, the magnetic moment of Mn is reduced to 2.80 μ_B in comparison to 2.90 μ_B found in GGA since there are more states below E_F in Mn minority PDOS. The inset in (Fig. 5.5a) provides the magnified image of majority spin PDOS in the vicinity of E_F. Similar to GGA results (see 4.8, inset), hybridization at MnPc/Co interface induces states near E_F in the majority spin channel which are absent for the free MnPc molecule.

The charge density contours propagating from Cu to MnPc indicate the presence of chemical hybridization at MnPc/Cu(001) interface. Similar to MnPc/Co(001), the Mn PDOS is broadened in both spin channels as compared to that of a free MnPc molecule. As discussed earlier, a consequence of this broadening is the reduction of the magnetic moment; Mn GGA magnetic moment on Cu(001) is 3.47 μ_B, and is reduced to 3.05 μ_B when calculated within GGA-D. A comparison of the charge density plots of MnPc/Co(001) and MnPc/Cu(001) shows clearly that the chemical interactions at MnPc/Cu(001) interface are much weaker in comparison to those of MnPc/Co(001). Consequently, the modification of the electronic structure of MnPc due to adsorption is relatively smaller for MnPc/Cu(001) than that of MnPc/Co(001).

Qualitatively, the electronic structure of MnPc on Co(001) has not changed significantly by the vdW interactions. For the unrelaxed geometry within GGA and GGA-D, and also for the relaxed geometry obtained using the GGA-D, we observe a strong chemical bonding at MnPc/Co(001) interface indicating that MnPc is chemisorbed on Co(001). On the other hand, while MnPc is predicted to be physisorbed on Cu(001) by GGA, we have shown that for the relaxed MnPc/Cu(001) interface, chemical interactions contribute also to the adsorption. Since this result is in agreement with

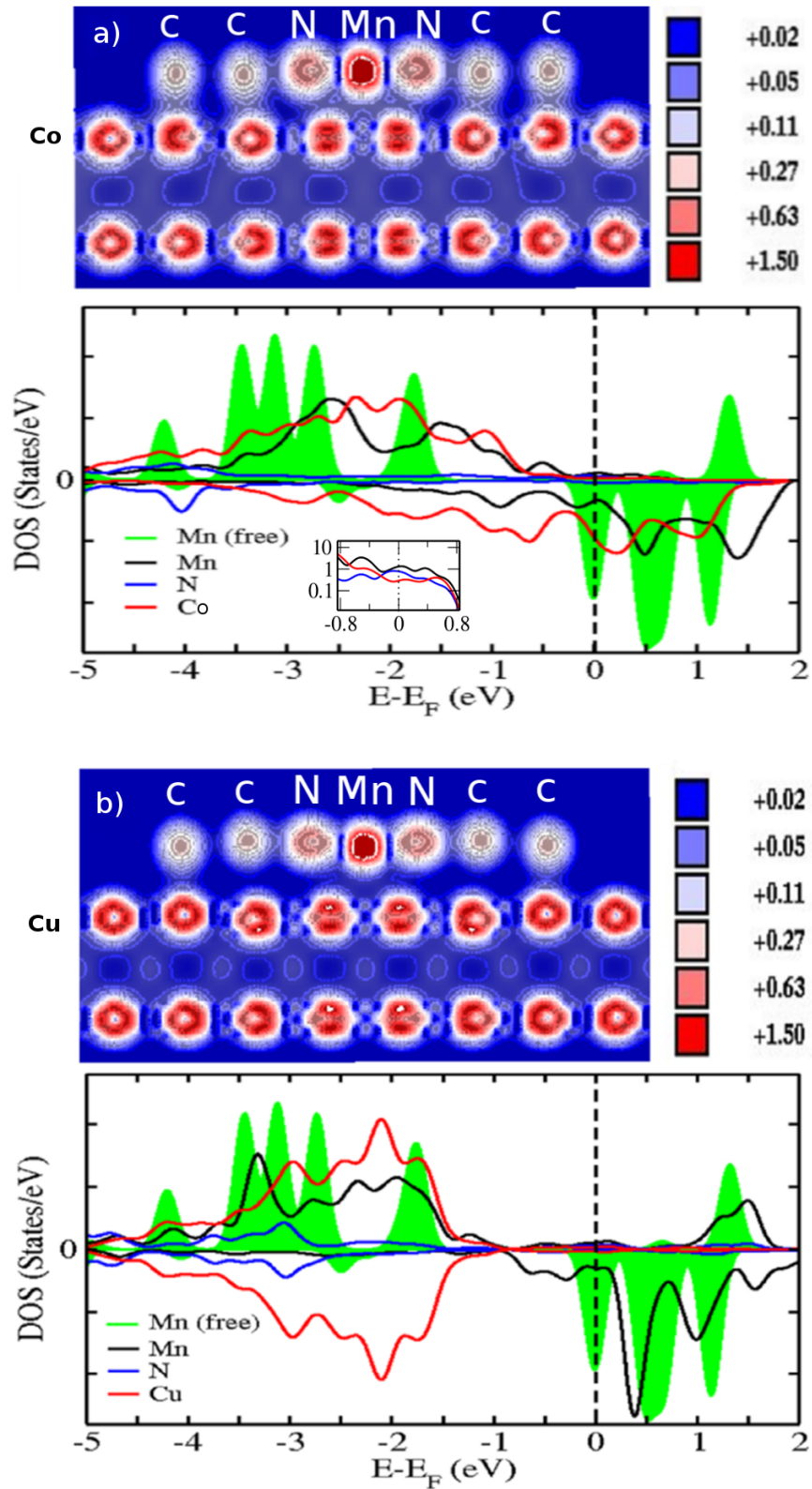Figure 5.5: Charge density plot along (110) plane (top panel) and PDOS of Mn, N and the top surface layer (bottom panel) of the relaxed structure obtained from DFT-D for a) MnPc/Co(001) and b) MnPc/Cu(001). The Mn PDOS for a free MnPc molecule is also plotted for comparison. The inset in bottom panel of (a) provides the magnified image of the the majority-spin PDOS of MnPc/Co(001) near the Fermi level in the log scale.

DFT-D calculations for unrelaxed MnPc/Cu(001), we conclude that the structural relaxation plays a minor role in determining the adsoption mechanism and the chemical hybridization at the interface are mainly due to the vdW interactions. Thus adsorption mechanism of MnPc on Cu(001) has changed from physisorption to weak chemisorption due to the vdW interactions. The change of the adsorption mechanism of organic adsorbate on metallic surfaces due to the vdW interactions has been also studied previously [9, 58]. Interestingly, the reduction in the adsorption distance due to the vdW interactions in these studies is much smaller ($\sim$ 0.50 Å) than found in our case for MnPc on Cu(001) ($\sim$ 1 Å).

5.3   Interface dipole and work function

A crucial aspect of molecular adsorption on metals is the subsequent change of the metal work function ($\Delta\Phi$) [114]. A metallic surface has an electric dipole formed due to tailing for electron density outside the surface thus making vacuum side negative and metal surface positive [25]. In order to extract an electron from the metal, the potential barrier created due to the surface dipole has to be overcome. When a molecule is adsorbed on a metal, interaction between the adsorbate and the metallic surface may create an additional dipole at the interface. Intuitively, an obvious reason for the formation of an interface dipole is the metal-adsorbate charge transfer. However, if naively the formation of the interface dipole is attributed only to the charge transfer than a metal to adsorbate charge transfer will create an interface dipole having the same direction as that of bare metallic surface. As a consequence the work function of the metal will increase ($\Delta\Phi > 0$) [26]. Conversely, in the case of a charge transfer from adsorbate to metal, the metal work function will decrease ($\Delta\Phi < 0$). In this section, we will show that despite the fact that the electric dipole due to charge tranfer has the same direction as the surface dipole, the work function decreases instead of increasing.

5.3.1   Work function change due to MnPc adsorption

We have used Löwdin population analysis to determine the net charge on MnPc molecule adsorbed on Co(001) or Cu(001). The results show that MnPc assumes a negative charge of $\sim$ 4.80 au and $\sim$ 2.60 au upon the adsorption on Co(001) and Cu(001) respectively (see table 5.1). Thus there is a net electron transfer from the metal to MnPc. The electron transfer is much stronger for MnPc on Co(001) owing to strong chemisorption and therefore the chemical bonding at MnPc/Co(001) interface has also a strong ionic character. A charge transfer from the metal to the MnPc

molecule means that MnPc adsorption induces an interface dipole directed towards the
metallic slab (i.e. a net accumulation of electrons near the molecule and depletion near
the surface of the slab). If we consider this dipole to be isolated from the surface (i.e.
we ignore any charge re-organization due to MnPc adsorption on Cu(001) or Co(001)),
this should lead to an increase of the metallic work function as explained before [26].

To confirm the insights coming from charge transfer analysis, we have calculated
the work function change due to MnPc adsorption.

$$\Delta\Phi = \Phi_{\mathrm{MnPc/slab}} - \Phi_{\mathrm{slab}} \,, \tag{5.1}$$

where $\Phi_{\mathrm{MnPc/slab}}$ and Φ_{slab} represent the work functions of the metallic slab (i.e.
Cu(001) or Co(001)) after MnPc adsorption and the free slab respectively. The work
function is calculated as the difference between the average vacuum potential and the
Fermi energy.

$$\Phi = E_{\mathrm{vacuum}} - E_F \,. \tag{5.2}$$

The results are summarized in table 5.1. We find that $\Delta\Phi$ has a value of $\sim$ -0.50
eV for MnPc/Co(001) and $\sim$ -0.33 eV for MnPc/Cu(001). According to (5.1), the
negative value means a decrease in work function due to MnPc adsorption. This result
is in apparent contradiction with charge transfer analysis which predicts an increase of
metallic work function due to MnPc adsorption.

	Φ (bare surface)	$\Delta\Phi$	charge transfer
MnPc/Cu	4.53 (4.63)	-0.33	2.60
MnPc/Co	4.65 (5.0)	-0.50	4.80

Table 5.1: Metal work function change $\Delta\Phi$ (in eV) of Cu(001) and Co(001) surfaces due to
MnPc adsorption. Slab of surface area 400 Å^2 contains one MnPc molecule. The theoretical
and experimental values of work functions Φ, for Cu(001) and Co(001) are also shown. The
experimental values for Cu(001) and Co(001), shown between parenthesis, are from ref. [115]
and ref. [116], respectively. The value of net metal to MnPc charge transfer (in au) is also
shown .

In order to resolve this apparent contradiction, we have calculated the planar aver-
aged charge density change ($\Delta\rho(z)$) due MnPc adsorption on Cu(00) or Co(001).

$$\Delta\rho(z) = \rho(z)_{\mathrm{MnPc/slab}} - \rho(z)_{\mathrm{slab}} - \rho(z)_{\mathrm{MnPc}} \,, \tag{5.3}$$

where $\rho(z)_{\mathrm{MnPc/slab}}, \rho(z)_{\mathrm{slab}}$ and $\rho(z)_{\mathrm{MnPc}}$ represent respectively the planar averaged

charge density of combined system (MnPc/Cu or MnPc/Co), metallic slab and the free MnPc molecule. Physically, $\Delta\rho(z)$ is the measure of charge re-organization due to the MnPc adsorption. The planar averaged charge density $\rho(z)$ is calculated by integrating charge densities in the x-y plane within the unit cell.

$$\rho(z) = \frac{1}{A} \int_A \rho(x, y, z) \mathrm{d}x\mathrm{d}y\,. \qquad (5.4)$$

The $\Delta\rho(z)$ for MnPc/Cu(001) and MnPc/Co(001) are shown Fig. 5.6. We observe that the charge re-organization of MnPc on Co(001) (Fig. 5.6b) is much stronger as compared to that of MnPc on Cu(001) (Fig. 5.6a) (the scale for MnPc/Co(001) is more than 2 times larger than that of MnPc/Cu(001)). This is because MnPc is more strongly chemisorbed on Co(001) as compared to Cu(001). We also observe that the charge re-organization for both system is oscillatory in nature (positive (negative) peaks corresponds to accumulation (depletion) in the electron density). Friedel oscillations may in part be responsible for these oscillations.

For both MnPc/Cu(001) (Fig. 5.6a) and MnPc/Co(001) (Fig. 5.6b) there is an accumulation of electron density on the topmost metallic layer and a depletion of electron density just above it. This is well known push-back or pillow effect [117] which is also known to exist for the organic adsorbates [28, 29]. The push-back effect arises due to the repulsion between the overlapping interface metallic and adsorbate orbitals. This repulsion is physical in nature (Pauli repulsion) and pushes the tailing part of metallic electron cloud back to the metal surface. This reduces the dipole present at the metallic surface (due to tailing of electron density) and thus the net result of push back effect is to reduce the work function of the metallic surface [118].

Another possible reason for the adsorption induced work function reduction is the image effect. The electron of the adsorbate are attracted by the image charge in the metal. This leads to the depletion of electrons at the vaccum side and accumulation near the metallic surface [25], i.e, a dipole is formed directed opposite to that of the bare metallic surface.

In Fig. 5.6, just above and below MnPc, a region of electron density depletion is present, accompanied by an accumulation of electron density at the interface for both systems. This re-arrangement is due to the interfacial chemical bonding as the electrons that will be otherwise lying close to MnPc plane are now engaged in hybridization at the center of the interface. The impact of chemical hybridiztion between electronegative adsorbate (i.e. adsorbate that accepts electrons from the metal surface) and metallic substrate on the work function change has been studied previoulsy [26, 27]. These
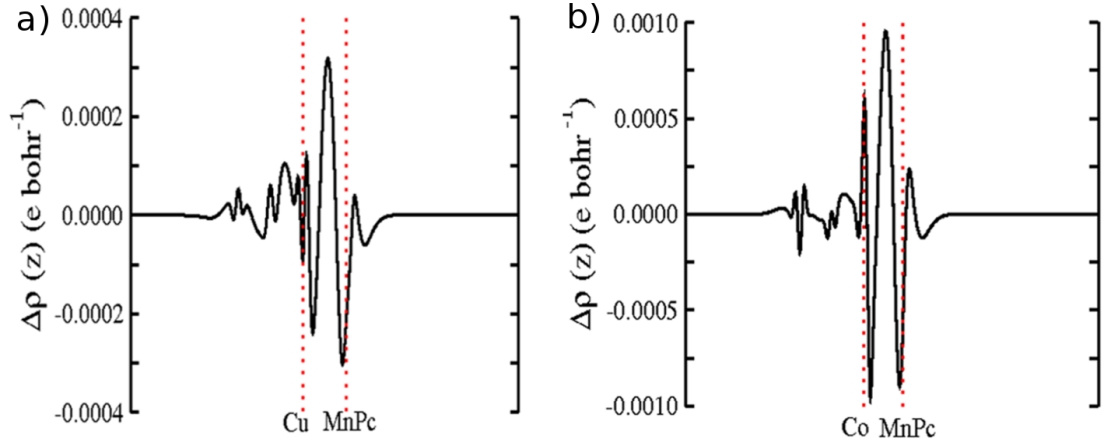
Figure 5.6: Planar average charge density change due to MnPc adsorption on a) Cu(001) or b) Co(001). The red dashed vertical lines represent the average position of the top surface layer and MnPc .

results show that the hybridization at the interface can also reduce the metal function. This is because the tailing electron density is pushed nearer to the surfaces due to hybridization [26] and also because the hybridization can reduce the adsorbate distance from metal, leading also to the lowering of the magnitude of the interface dipole between negative adsorbate and positive metallic surface [27]. In the light of these finding, it is possible that the hybridization at MnPc/Cu(001) and MnPc/Co(001) interfaces may also be contributing to the reduction of the metal work function along side push-back effect.

We thus see that various mechanisms compete to determine the sign and the magnitude of $\Delta\Phi$ at the MnPc/metal interface. The charge transfer from the metal to MnPc tends to increase the metallic work function ($\Delta\Phi > 0$) while push-back effect, image forces, Friedel oscillations and possibly chemical bonding act in conjunction to reduce the metallic work function ($\Delta\Phi < 0$). The fact that $\Delta\Phi$ is found to be negative by calculations shows that impact of charge transfer is overcome by other physical (like push-back effect) or chemical interactions present at the interface.

5.4   XSW experiments

In the preceding sections, we have discussed the impact of the vdW interaction on the adsorption of MnPc on Cu(001) and Co(001). The weak vdW interactions have particularly telling effect on the MnPc/Cu(00) such that the adsorption distance of MnPc reduces drastically, leading to the change of the adsorption mechanism. It is

therefore clear that an experimental determination of the adsorption distance of MnPc on Cu(001) is necessary for affirming or not the reliability of our theoretical results. In this section, we will describe the results of a recently performed XSW experiment to determine the adsorption distance of MnPc on Cu(001). The experimental XSW data is still in the process of being analyzed and here we present the preliminary results. The main focus of the discussion is the Cu-C distance. This is because C constitutes a large proportion of MnPc molecule (C constitutes $\sim$ 56 % of MnPc), therefore the signal to noise ratio of C XSW spectra is much better than other MnPc elements.

Before discussing the experimental results, we summarize some of the important aspects of XSW analysis. The XSW analysis give mainly two parameters, coherent fraction (F_H) and coherent position (P_H) where F_H describes the degrees of disorder of the adsorbate atom under investigation and P_H gives its position with respect to scatterer planes (modulo d_H). The distance of adsorbate atom from the substrate Bragg planes is determined as [49, 50]

$$d = d_H(1 + P_H), \tag{5.5}$$

where d_H is the ideal scatterer planes spacing. For Cu(001) surface, the value of d_H is 1.805 Å.

It is important to note that in the XSW experiments, the adsorbate-surface distance is given with respect to the ideal topmost bulk lattice plane rather than the topmost layer of relaxed surface [29] as illustrated in Fig. 5.7. A deviation of the surface lattice planes from ideal bulk structure appears in coherent fraction F_H whose value is reduced from 1 due to the atomic relaxations. Therefore, we have used the same definition for determining the theoretical distances.
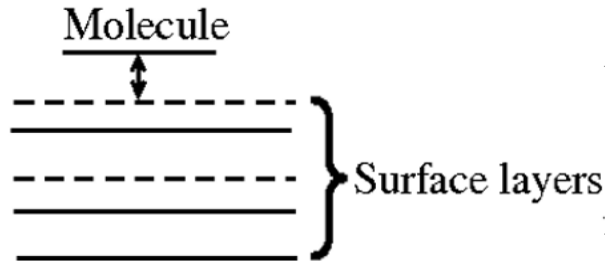

Figure 5.7: Schematic explaining that in XSW experiments, the molecular adsorption distance is measured with respect to the position of the ideal topmost bulk plane (dashed) rather than actual (relaxed) topmost plane of the surface. The difference between topmost planes of bulk and relaxed surface is exaggerated for clarity.

5.4.1   XSW analysis for C

The XSW measurements for C are summarized in Fig. 5.8. The core-level photoemission spectra for C 1s level is shown in Fig. 5.8a. The photoemission spectra can be resolved into two peaks (C1, C2), corresponding to two C sites, distinguishable within the experimental resolution. The peak appearing at the higher binding energy (C1) come from the pyrrole while the second peak (C2) correpsonds to the benzene [40] in MnPc. Fig. 5.8b shows the photoemission yield curve as a function of photon energy in the Bragg reflection range for the two peaks appearing in the photoemission spectra. The structural parameters are obtained by fitting Eq. (3.15)((solid black line) to the experimental photoemission yield (red circles) using DARE programme [110].

The structural parameters obtained from the fitting are summarized in table 5.2. For the peak marked as C2, we find a value of 0.313 ± 0.0157 and 0.316 ± 0.0437 for the P_H and F_H respectively. According to Eq. 5.5, this means that C atoms corresponding to the C2 peak are $2.37(\pm 0.02)$ Å above Cu(001) surface. As for peak C1, the fitting gives a value of 0.328 ± 0.020 and 0.458 ± 0.0834 for the P_H and F_H respectively. This corresponds to Cu(001)-C distance of $\sim 2.40(\pm 0.036)$ Å. For both C sites, we find low values of coherent fraction F_H, indicating a relatively higher disorder in the (vertical) position of C atoms and thus the P_H corresponds to an average value. Nevertheless, it is interesting to note that the P_H of the two C sites are very close to each other (2.37 Å and 2.40 Å) within the experimental errors.

	C2	C1	GGA-D
F_H	0.316(±0.043)	0.458(±0.083)	-
P_H	0.313(±0.015)	0.328(±0.020	-
d (Å)	2.37(±0.027)	2.40(±0.036)	2.39

Table 5.2: Coherent fraction (F_H), coherent position (P_H) and the corresponding Cu(001)-C distance (d) for the two C sites. For comparison, the GGA-D results are also shown.

Consistent with the experimental results, the calculated relaxed interface geometry (Sec. 5.3) show a relatively large spread in the vertical position of C on Cu(001). The average Cu(001)-C distance is calculated to be 2.39 Å, in excellent agreement with the experimental results (the theoretical value lies within the experimental error). It must be mentioned that we have discussed only the preliminary results and in a more complete analysis, experimental Mn-Cu(001) and N-Cu(001) distances should also be
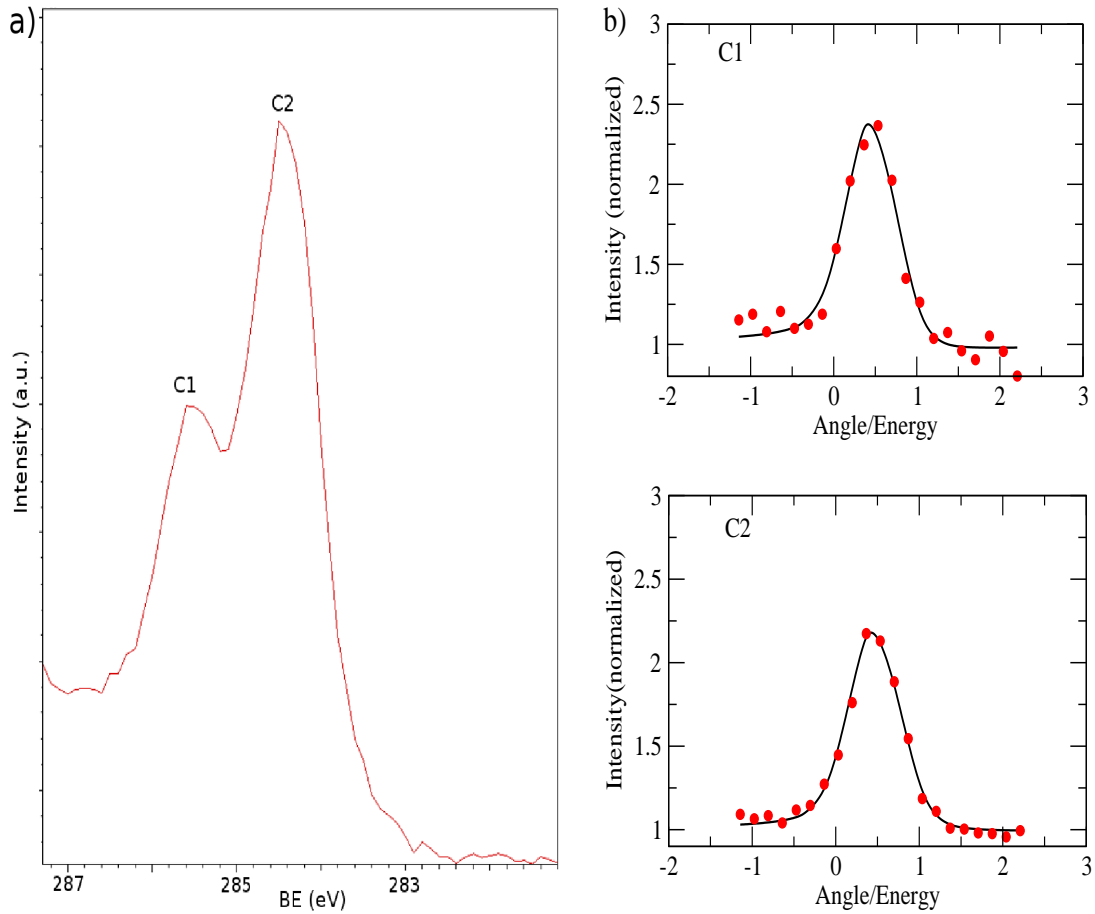
Figure 5.8: a) Core-level photoemission spectra of MnPc C 1s level near Bragg reflection. The spectra is resolved into two peaks C1, C2 . b) XSW scans for for the peaks C2 (top) and C1 (bottom). Red circles are the experimental data points while the solid black lines are the least-square fits to obtain coherent fraction and coherent position

compared with the theory. Nevertheless, it is evident that the GGA largely overestimates the MnPc adsorption distance on Cu(001) and the inclusion of the vdW interactions (GGA-D approach) provides a major improvement to the calculated adsorption distances.

5.5   Conclusion

In this chapter, we have studied the effect of the vdW interactions on the adsorption of MnPc on Co(001) and Cu(001). We have shown that there is no significant change in the adsorption distance of MnPc on Co(001) due to the vdW interactions. On the other hand, the distance between MnPc and Cu(001) is reduced drastically (~ 1 Å) as weak vdW interactions are taken into account. For both MnPc/Co(001) and MnPc/Cu(001), the vdW interactions strongly modify the energetics of adsorption as the adsorption energies of MnPc on Cu(001) or Co(001) increase sharply with GGA-D as compared to those obtained using GGA. The geometry optimization of MnPc/Cu(001) and MnPc/Co(001) leads to a slight distortion of MnPc molecules as its atoms are vertically displaced from each other due to atomic relaxations. In particular, we observe that the C atoms in benzene ring are strongly depressed as compared to other MnPc atoms, indicating that the chemical interactions between MnPc benzene ring and the underlying surface play an important role in MnPc adsorption. We have measured the distance between C (in MnPc) and Cu(001) surface through XSW experiments and the results are in good agreement with the average Cu-C distance obtained from the relaxed geometry of MnPc/Cu(001).

Since MnPc is found to be chemisorbed on Co(001) by means of GGA, no significant change of adsorption distance is observed due to the vdW interactions. However, the interface chemical interactions and electronics structure of MnPc/Cu(001) are significantly effected as the vdW interactions are taken into account. Thus the adsorption mechanism of MnPc on Cu is changed from physisorption to weak chemisorption. DFT calculations show that the adsorption of MnPc on Cu(001) and Co(001) leads to a reduction of the metal work function. The magnitude of the work function change and thus the interface dipole depends on the MnPc adsorption distance from the substrate.

Evidently, the main result of this chapter is the dramatic impact of the vdW interaction on MnPc/Cu(001) interfacial properties. The change of adsorption mechanism from physisorption to weak chemisorption has also been theoretically predicted for the adsorption of other organic molecules on metallic surfaces [9]. However a direct experimental confirmation of theoretical predictions is necessary for validating the theoretical approach. In this respect, through a comparison of calculated adsorption distances and XSW experimental results, we are able to show that GGA-D approach provides a much better description of MnPc adsorption on Cu(001) in comparison to pure GGA calculations. These results are consistent with a recent combined STM and DFT study on CoPc/Fe(111) [58], and highlight the necessity of including vdW interactions in

ab-initio DFT calculations.

An important aspect of the MnPc/metal interfacial interactions is the creation of interface dipole due to MnPc adsorption. From a fundamental perspective, the competition of various (physical or chemical) mechanisms so as to define the sign and magnitude of interface dipole highlights the complexity of MnPc/metal interface. This study seems to indicate that a detailed understanding of phthalocyanine/metal interfacial electronic properties is an important step towards achieving a control over charge and spin injection across these interfaces.

XSW experiments discussed in this chapter describe only the distance of C (in MnPc) from Cu(001) substrate. For a more complete comparison with theory, experimental determination of Cu-N and Cu-Mn distances is also necessary. Furthermore, XSW experiments for chemisorbed MnPc/Co(001) will also be helpful in estimating the accuracy of the theoretical results. On the theoretical side, an improvement to DFT-D approach has been recently proposed (DFT-D3) [83]. In DFT-D3 approach, the dispersion coefficients of the atoms are calculated by taking into account the chemical enviorment. The study of MnPc/Cu(001) and MnPc/Co(001) by DFT-D3 may help improve the theoretical results, in particular the adsorption energy of MnPc on Cu(001) or Co(001).

Chapter 6

Spin Polarization at MnPc/Co(001) Interface

The main aim of this chapter is to study the impact of the MnPc/Co(001) interfacial hybridization on the spin polarization of MnPc molecules near E_F. The spin polarization of MnPc, induced by interaction with the Co(001) substrate is important for the understanding of the spin polarized transport as discussed in section 1.3. In chapter 4, we have discussed the magnetic interactions at the MnPc/Co(001) interface in terms of magnetic coupling between MnPc and Co(001) substrate. Here the main focus of the discussion will be the C and N atoms (i.e. Pc ring) of MnPc molecules. In particular, we aim to confirm the theoretical insight coming from LDOS analysis (section 4.3) which shows that at E_F, C and N atoms dominate the majority spin channel while the main contribution to the minority spin channel comes from Mn. This chapter is organized as follows. In section 6.1, we study the spin polarization at the MnPc/Co(001) interface through spin-resolved photoemission spectroscopy. In section 6.2, we focus on the N site and describe the impact of Co(001) substrate on its magnetic properties through N K-edge XMCD experiments. Finally, we summarize the main results and conclude in section 6.3.

6.1 Spin-resolved photoemission of MnPc/Co(001)

In this section, we describe the results of spin-resolved photoemission experiments performed to determine the spin polarization at the MnPc/Co(001) interface. The details about the experimental conditions and the sample preparation can be found in

the section 3.2.

Fig. 6.1 shows the photoemission spectra of the two spin channels for Co(001) (Fig. 6.1a) and 1.3 ML MnPc/Co(001) (Fig. 6.1b) measured at 20 eV. For Co(001) and 1.3 ML MnPc/Co(001), we find that the photoemission spectra for the two spin channels are different thus indicating the presence of ferromagnetism in both samples. Fig. 6.1c depicts the % spin polarization (P) for the Co(001), 1.3 ML MnPc/Co(001) and 2.6 ML MnPc/Co(001), calculated as

$$P(E) = \frac{I^\uparrow(E) - I^\downarrow(E)}{I^\uparrow(E) + I^\downarrow(E)} \times 100, \tag{6.1}$$

where $I^\uparrow(E)(I^\downarrow(E))$ stands for the photoemission signal at a given energy E in the majority (minority) spin channel. For Co(001) the spin polarization is strongly negative at E_F. This is understandable since 3d bands of ferromagnetic Co are exchange split and therefore the DOS for the minority spin channel is much higher at E_F as compared to that of the majority spin channel. However, MnPc/Co(001) samples show qualitatively different behavior in the vicinity of E_F. In the region ~ 0.20-0.30 eV below E_F (indicated by the arrow), the spin polarization of Co(001) is negative whereas the spin polarization of 1.3 ML MnPc/Co(001) is almost zero. This result seems to suggest that MnPc has a net positive spin polarization on the Co(001) surface in the vicinity of E_F. However, the spin polarization of 1.3 ML MnPc/Co(001) near E_F can be less negative in comparison to that of Co(001) also due to the decay of Co(001) photoemission signal which is in turn due to MnPc deposition. The impact of MnPc becomes much more revealing for the case of 2.6 ML MnPc/Co(001) where the spin polarization becomes positive (as opposed to the negative spin polarization of Co) in this region. The inversion of spin polarization near E_F (see the region identified by the arrow) confirms the fact that the hybridization at MnPc/Co(001) interface induces a net positive polarization on MnPc near E_F.

While interpreting these results, the dependence of the photoemission cross section of the different orbitals on the photon energy must be considered. At 20 eV, the photoemission cross sections of 2p orbitals of N and C and 3d orbitals of Mn and Co are comparable [119]. In order to identify the atomic sites responsible for the observed positive spin polarization of MnPc on Co(001) near E_F at 20 eV, we performed the spin-resolved photoemission experiments at 100 eV. At 100 eV, the cross section of d states increases by an order of magnitude as compared to that of p states [119]. Therefore the photoemission spectra will be dominated by Mn rather than N and C in MnPc. Fig. 6.2 shows the photoemission spectra of the two spin channels for Co(001) (Fig. 6.2a)
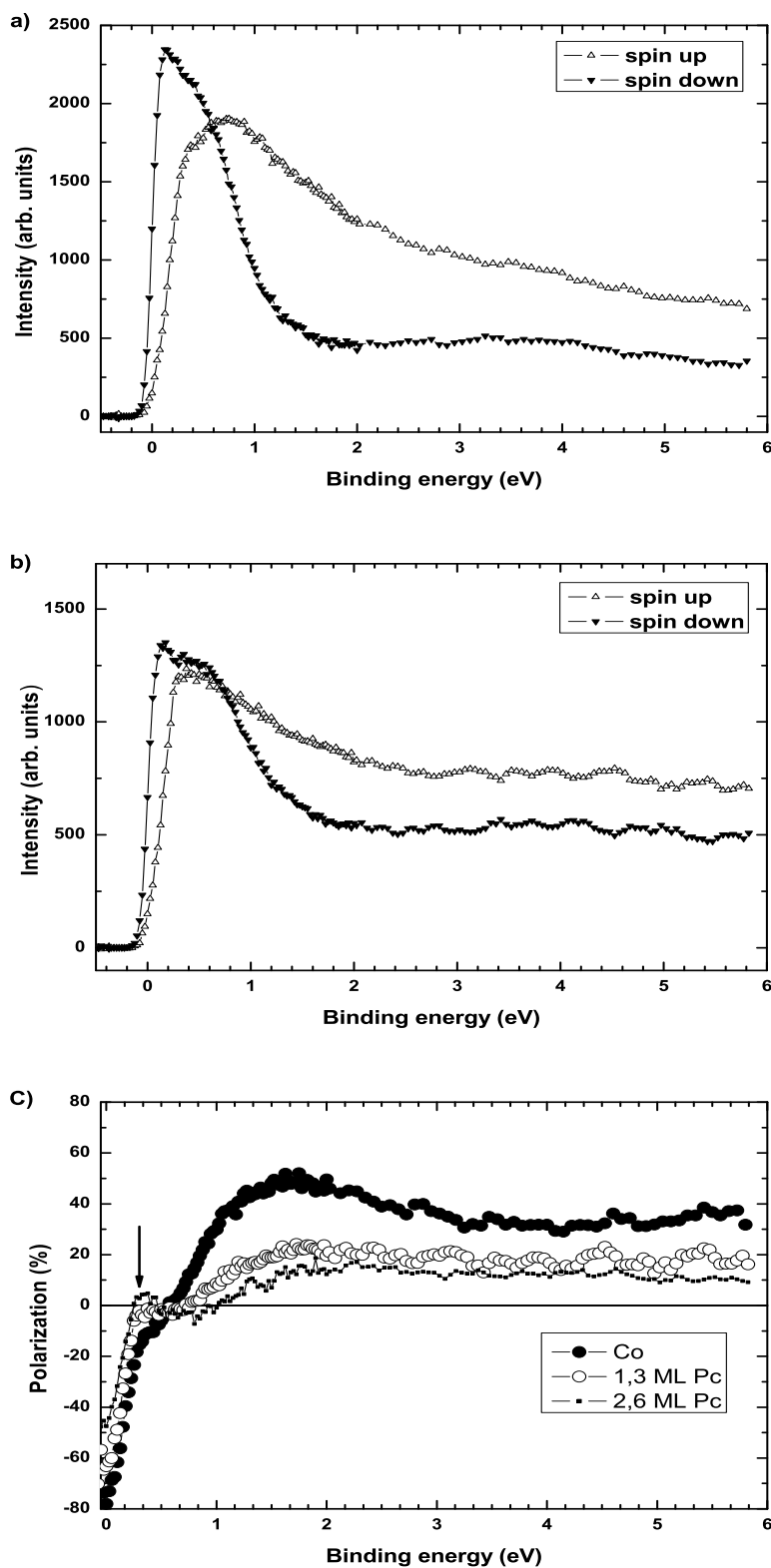
Figure 6.1: Spin resolved photoemission spectra of a) Co(001) and b) 1.3ML MnPc/Co(001). c) Spin polarization (%) for Co(001), 1.3 and 2.6 ML of MnPc on Co(001). All spectra are measured at 20 eV.
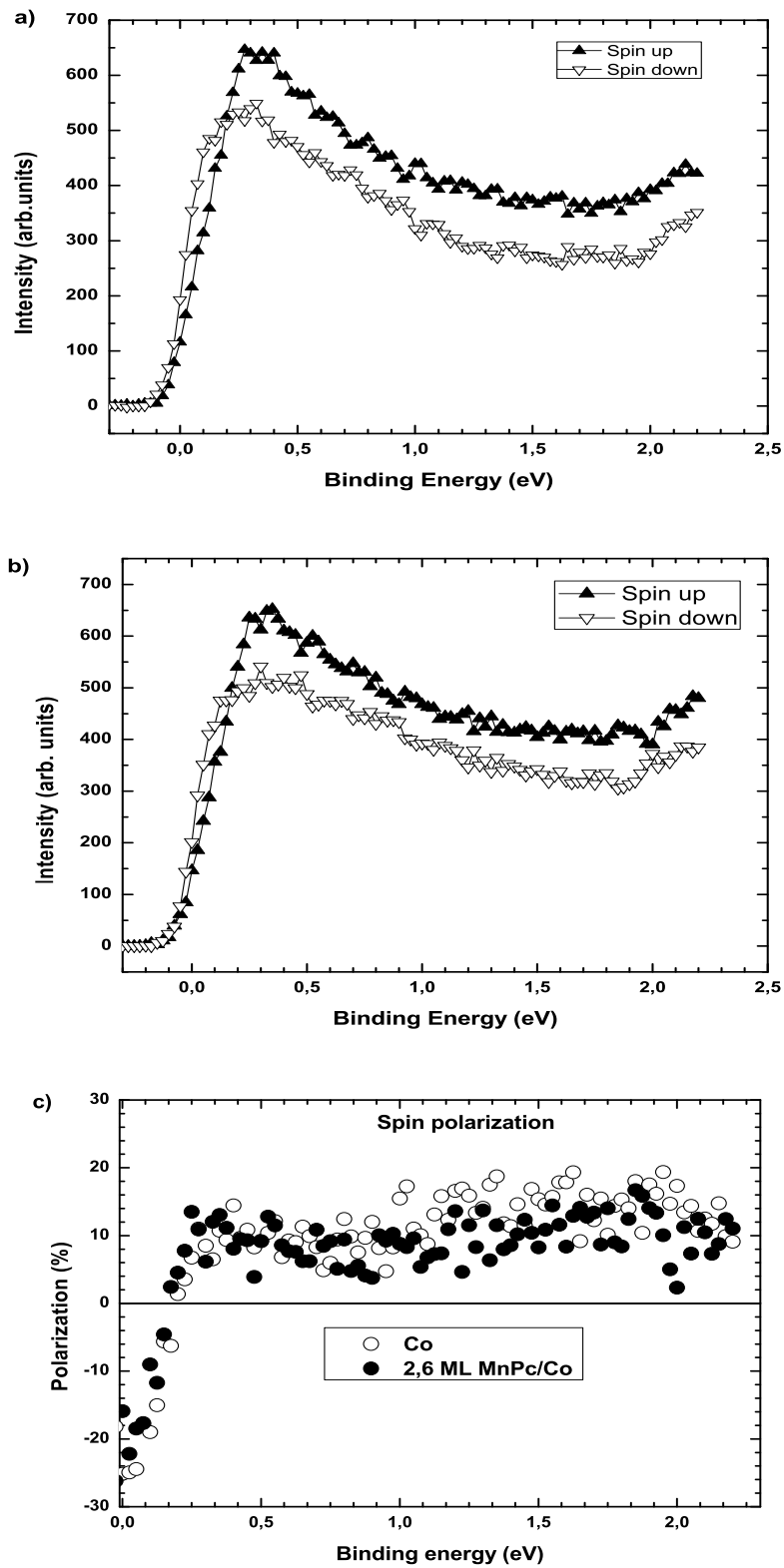
Figure 6.2: Spin resolved photoemission spectra of a) Co(001) and b) 2.6ML MnPc/Co(001) measured at 100 eV. c) Spin polarization (%) for Co(001) and 2.6 ML of MnPc on Co(001).

and 2.6 ML MnPc/Co(001) (Fig. 6.2b) measured at 100 eV. Fig. 6.2c displays the corresponding spin polarization. Unlike the spin polarization spectra measured at 20 eV, the spin polarization of 2.6 MnPc/Co(001) is similar to that of Co(001) for 100 eV. This is because the Co d orbitals dominate the photoemission spectra. These results confirm that the positive spin polarization near E_F of MnPc on Co(001) observed at 20 eV arises from 2p orbitals of N and C atoms.

We also note that these experimental findings are in qualitative agreement with both GGA and GGA-D results. GGA calculations for MnPc/Co reveal the presence of the hybridization induced interfacial states such that N and C sites of MnPc have a net positive polarization near E_F (see Fig. 4.8 (inset), Fig. 4.11). Similar results are also found for GGA-D calculations (see inset of Fig. 5.5a).

6.2 XMCD at Nitrogen K-edge

In this section, we describe the impact of Co(001) on the mangetic properties of N sites in MnPc. We will mainly discuss the results of N K-edge XMCD spectroscopy performed at ESRF. It is important to mention that the K-edge XMCD reveals only the orbital magnetism [120].

We first confirm the ferromagnetic coupling between MnPc and Co(001) (Co(001) corresponds to 5 ML Co/Cu(001)). Fig. 6.3 depicts the hysteresis loop of Mn for 1.2 ML MnPc/Cu(001) (Fig. 6.3a) and 1 ML MnPc/Co(001) (Fig. 6.3b) recorded at L-edge. In the latter figure, the Co hysteresis loop is also plotted for comparison. For 1.2 ML MnPc/Cu(001), the hysteresis loop of Mn is measured for the incidence angle of 0° (i.e. normal incidence) and 40° of photon beam with respect to the surface normal. In both cases, the hysteresis loops can be fitted nicely by the Brillouin function[1] (blue) which confirms the paramagnetic behavior of MnPc molecules on Cu(001). Interestingly, the hysteresis loops measured at 0° and 40° incidences are similar, indicating that MnPc molecule has only a small magnetic anisotropy on Cu(001). In sharp contrast to 1.2 ML MnPc/Cu(001), the hysteresis loop of Mn for 1 ML MnPc/Co(001) is much squarer and coincides nicely with that of Co(001). We therefore conclude that MnPc is magnetically coupled to Co(001), consistent with our previous experimental results (see section 4.2).

We now turn to the magnetic properties of N in MnPc. Fig. 6.4 displays the XAS (top) and corresponding XMCD (bottom) for 1.2 ML MnPc/Cu(001) (Fig. 6.4a) and 1 ML MnPc/Co(001) (Fig. 6.4b). For 1.2 ML MnPc/Cu(001), the XAS of N K-edge has a sharp peak at $\sim$ 401 eV arising due to the adsorption of molecular N.

---

[1]Brillouin function is calculated for the intermediate spin state of Mn, i.e., S=3/2

As for the XMCD, there is no visible signal outside the noise level besides the spurious signal coming from the molecular N. In order to avoid the problem of the adsorption of molecular N, the XAS experiments for 1 ML MnPc/Co(001) were performed at room temperature. Unlike the case of 1.2 ML MnPc/Cu(001), a clear XMCD signal is present at the N K-edge for 1 ML MnPc/Co(001). We note that the XMCD signal has maximum intensity in the energy range of 397-407 eV. This energy range mainly corresponds to out of plane π^* states [40] which hybridize directly with Co atoms. Also the orbital moment of N is aligned parallel to that of Co. This is because the orbital moment is proportional to the integral of XMCD signal [89]. For both N K-edge and Co L-edge (for L-edge, integral should be performed over L_2 and L_3 edges), the integral of XMCD has the same sign, i.e., negative. This shows that Co(001) induces an orbital magnetic moment on N, aligned parallel to the orbital magnetic moment of Co(001).

While the N K-edge XMCD probes the orbital magnetism, DFT calculations of the relaxed MnPc/Co(001) reveal the impact of interfacial interactions on the spin magnetism of N. N atoms in free MnPc molecule have small local magnetic moment aligned oppositely to that of Mn. However on Co(001), the spin magnetic moment of N atoms becomes parallel to the magnetic moment of Co(001) and Mn. We therefore conclude that the magnetic properties of N in MnPc are strongly modified due to interactions at MnPc/Co(001) interface.
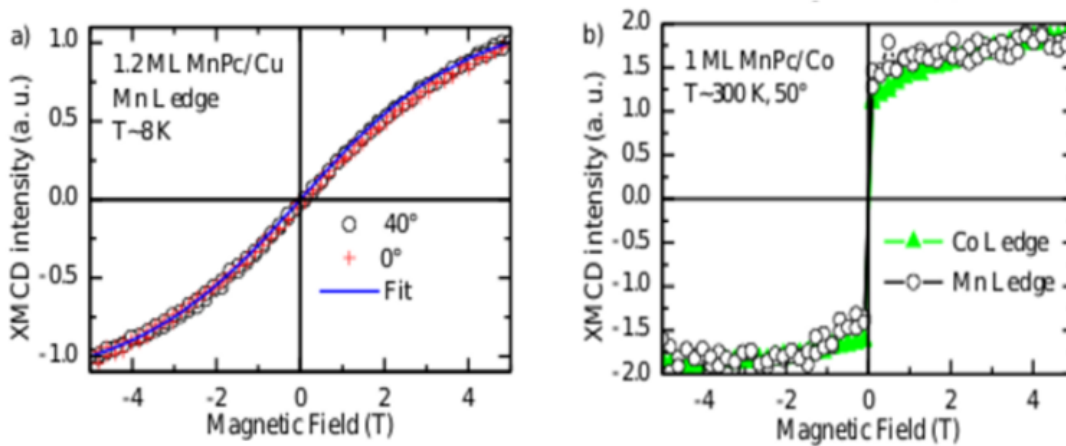
Figure 6.3: Element specific hysteresis loop of a) Mn for 1.2 ML MnPc/Cu(001) at an incidence of 0° and 40°, and of b) Mn and Co for 1 ML MnPc/Co(001) at an incidence of 50°. Blue line in a) represents the Brillouin function fit to the Mn hysteresis loops.
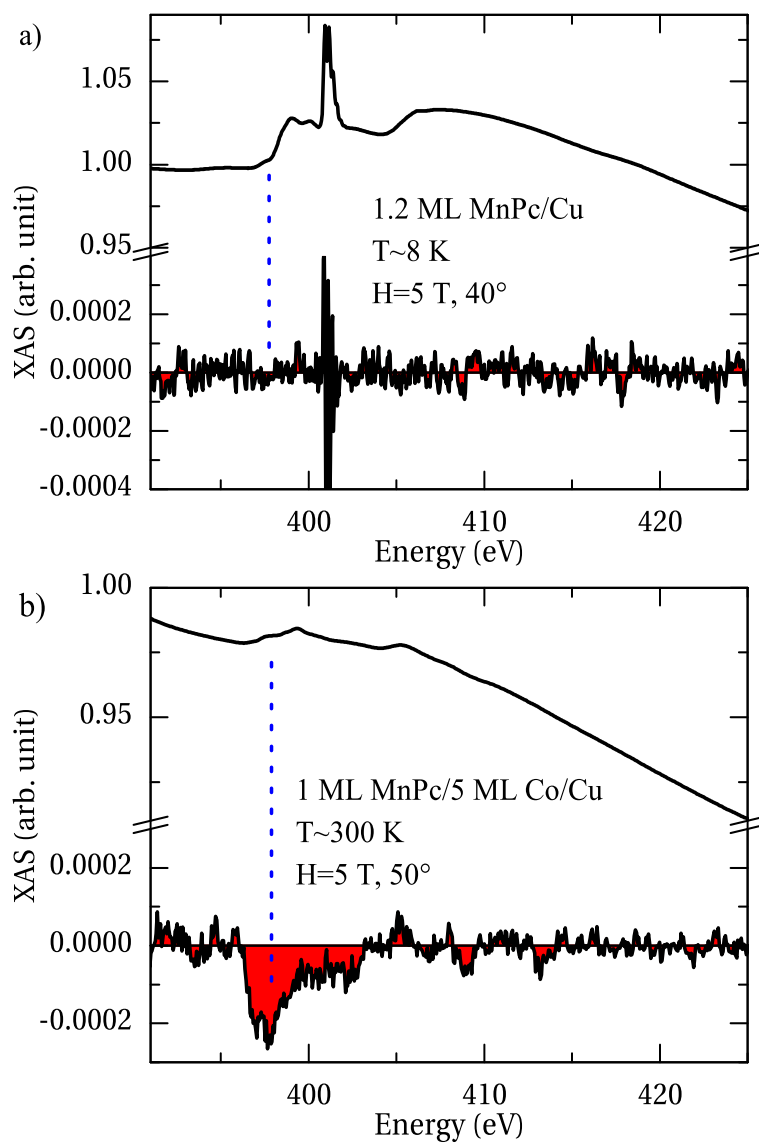
Figure 6.4: XAS (top) and XMCD (bottom) at the N K edge for a) 1.2 ML MnPc/Cu(001) and b) 1 ML MnPc/Co(001). The blue dashed line indicates the region in N XAS spectra which yields the maximum XMCD signal for 1 ML MnPc/Co(001) [121]. XMCD is obtained by normalizing the difference of the XAS spectra for the two polarizations by the edge jump of the isotropic spectra.

6.3 Conclusion

In this chapter, we have studied the impact of ferromagnetic Co(001) substrate on the magnetic properties of MnPc with the main focus on N and C atoms. Spin-resolved photoemission experiments performed at 20 eV show that Co(001) induces a net positive spin polarization on MnPc near E_F. Furthermore, we demonstrate that this spin polarization originates from C and N atoms in MnPc. Magnetic properties of N were probed by the N K-edge XMCD. We found that Co(001) induces an orbital magnetic moment on N which is aligned parallel to that of Co.

C and N sites are non-magnetic in MnPc molecule. However due to hybridization with the Co(001) substrate, N and C sites become spin polarized . The impact of interfacial interactions is highlighted by the fact that the sign of this spin polarization is opposite to that of the substrate Co(001)in the vicinity of E_F. From a technological perspective, the spin polarization on MnPc, induced and modulated by ferromagnetic substrates underscores the suitability of MPc/ferromagnetic hybrid interfaces for the efficient spin injection and spin transport.

Conclusions and Perspectives

The main objective of this combined theoretical and experimental thesis has been to understand the adsorption of MnPc on Co(001) or Cu(001) metallic surfaces and the ensuing interfacial interactions. Here we summarize the main results of this thesis along with some suggestions with regards to the future work.

First, we have performed DFT calculations (within GGA) to study the adsorption of MnPc on Cu(001) or Co(001). We found that the adsorption distance of MnPc on Co(001) is much smaller as compared to that on Cu(001). Furthermore, the adsorption energy of MnPc on Co(001) is much higher in comparison to the adsorption energy of MnPc on Cu(001). Both calculated adsorption distances and adsorption energies indicate that interfacial chemical interactions are much stronger for MnPc/Co(001) as compared to MnPc/Cu(001). We therefore concluded that MnPc is physisorbed on Cu(001) and chemisorbed on Co(001). Experimentally, MnPc adsorption has been studied by the means of x-ray absorption spectroscopy. The N K-edge XAS spectra show that while the electronic structure of MnPc on Cu(001) resembles that of a free MnPc molecule, it is strongly modified on Co(001) due to interfacial hybridization. We therefore found a qualitative agreement between the experimental results and the DFT calculations.

The magnetic interactions at MnPc/Co(001) and MnPc/Cu(001) interfaces have been studied thoroughly in this work. We first addressed the question of ferromagnetic coupling between MnPc and Co(001). The XMCD and hysteresis loop of Mn at the L-edge indicate that MnPc retains its paramagnetic state on Cu(001). However on Co(001), the XMCD spectrum of Mn is much smoother as compared to that of MnPc/Cu(001). Moreover, the hysteresis loop of Mn is a square and coincides with the hysteresis loop of Co(001) substrate. This showed that Mn in MnPc is ferromagnetically coupled to Co(001). The calculated interfacial electronic structure confirmed this result and also pointed out that the exchange mechanism of the interfacial magnetic coupling is direct exchange. Besides the central transition metal Mn site in MnPc, we

have also studied the impact of magnetic interactions on Pc atoms, i.e., C and N. The XMCD experiments performed at the N K-edge showed that Co(001) induces orbital magnetic moment on N sites, aligned parallel to that of Co(001). The spin polarization of MnPc on Co(001) have been studied by spin-resolved photoemission spectroscopy. The results showed that the hybridization of Co(001) and MnPc leads to a net positive spin polarization on Pc atoms (C and N) near E_F.

We finally describe the impact of the vdW interactions on MnPc adsorption. Besides adding a semi-empirical dispersion correction (i.e. DFT-D method) to the total energy, we also performed the geometry optimization (the vdW forces were included within DFT-D approach) to obtain optimal atomic positions. The main results are that MnPc, which is found to be chemisorbed on Co(001) from the GGA calculations, does not show a significant change in either the adsorption distance or the electronic structure. This is understandable since due to the presence of chemical interactions at MnPc/Co(001) interface, the effect of vdW interactions is small. The vdW interactions however bring a drastic change to the adsorption of MnPc on Cu(001), namely the adsorption distance is reduced by about 1 Å. Much shorter adsorption distance (~ 2.40 Å) allows for the hybridization at MnPc/Cu(001) interface. Therefore the adsorption mechanism of MnPc on Cu(001) changes from physisorption to weak chemisorption. The adsorption distance of MnPc on Cu(001) is determined by XSW experiments and is found to be in good agreement with the adsorption distance calculated by the GGA-D approach.

The results obtained in this work highlight the strong impact of ferromagnetic substrate on the magnetic properties of paramagnetic MnPc molecule. The magnetic interactions at MnPc/Co(001) interface lead to magnetic coupling between Mn and Co(001). Furthermore, the non-magnetic benzopyrrole rings (i.e. C and N atoms) of the MnPc molecule also become magnetically polarized due to the interactions with Co(001) substrate. An interesting consequence of the strong hybridization at MnPc/Co(001) interface is the inversion of spin polarization of the benzopyrrole rings of MnPc in comparison to Co(001) near E_F. Such inversion has been recently observed for H_2Pc/Fe by spin polarized STM experiments [122]. From spintronics perspective, the spin polarization on MnPc, induced and modulated by ferromagnetic substrates underscores the possibility of efficient spin injection across MPc/ferromagnetic hybrid interfaces.

The theoretical description of interfacial magnetic interactions can be improved by including spin-orbit coupling in our DFT calculations. This will allow us to calculate the orbital moment and therefore a direct comparison with the N K-edge XMCD experiments will be possible. Furthermore, the magnetic anisotropic energy (MAE) of

MnPc molecules on metallic substrates can be calculated. On the experimental side, element selective XMCD experiments have been very helpful in revealing the interfacial magnetic interactions. In the future, spin polarized STM can be used to probe the local magnetic and transport properties of phthalocyanine molecules on the magnetic surfaces.

Another interesting finding of this work is the drastic change in the adsorption distance of MnPc on Cu(001) due vdW interactions. Our combined experimental and theoretical study has shown that GGA-D approach provides a much better description of MnPc adsorption on Cu(001) in comparison to pure GGA calculations. Theoretical results within DFT-D can be further refined by calculating dispersion co-efficient from first principle as proposed recently (DFT-D3 method) [83]. It may also be helpful to compare the results of semi-empirical DFT-D method with that of ab-initio methods (such vdW-DF). On the experimental side, the determination of the adsorption distances and adsorption energies of MnPc on Co(001) or Cu(001) will provide valuable insights into the adsorption of phthalocyanine molecule on the metallic surfaces.

Bibliography

[1] W. J. Naber, S. Faez, and W. G. van der wiel. Organic spintronics. *J. Phys. D: Appl. Phys.*, 40:R205–R228, 2007.

[2] V. A. Dediu, L. E. Hueso, I. Bergenti, and C. Taliani. Spin routes in organic semiconductors. *Nat. Mater.*, 8:707, 2009.

[3] S. Santivo. The rise of spinterface science. *Nat. Phys.*, 6:562, 2010.

[4] P. Ruden. Interfaces are critical. *Nat. Phys.*, 10:8, 2011.

[5] C. Barraud, P. Seneor, R. Mattana, S. Fusil, K. Bouzehouane, C. Deranlot, P. Graziosi, L. Hueso, I. Bergenti, V. Dediu, F. Petroff, and A. Fert. Unravelling the role of the interface for spin injection into organic semiconductors. *Nat. Phys.*, 6:615, 2010.

[6] X. Chen and M. Alouani. Effect of metallic surfaces on the electronic structure, magnetism, and transport properties of Co-phthalocyanine molecules. *Phys. Rev. B*, 82:094443, 2010.

[7] A. Scheybal, T. Ramsvik, R. Bertschinger, M. Putero, F. Nolting, and T.A. Jung. Induced magnetic ordering in a molecular monolayer. *Chem. Phys. Lett.*, 214:411, 2005.

[8] H. Wende, M. Bernien, J. Luo, C. Sorg, N. Ponpandian, J. Kurde, J. Miguel, M. Piantek, X. Xu, Ph. Eckhold, W. Kuch, K. Baberschke, P. M. Panchmatia, B. Sanyal, P. M. Oppeneer, and O.Eriksson. Substrate-induced magnetic ordering and switching of iron porphyrin molecules. *Nat. Mater.*, 6:516, 2007.

[9] N. Atodiresei, V. Caciuc, P. Lazic, and S. Blugel. Chemical versus van der Waals interaction: The role of the heteroatom in the flat absorption of aromatic molecules C_6H_6,C_5NH_5 , and $C_4N_2H_4$ on the Cu(110) surface. *Phys. Rev. Lett.*, 102:136809, 2009.

[10] P. Giannozzi, S. Baroni, N. Bonini, M. Calandra, R. Car, C. Cavazzoni, D. Ceresoli, G.L. Chiarotti, M. Cococcioni, I. Dabo, A. Dal Corso, S. Fabris, G. Fratesi, S. de Gironcoli, R. Gebauer, U. Gerstmann, C. Gougoussis, A. Kokalj, M. Lazzeri, L. Martin-Samos, N. Marzari, F. Mauri, R. Mazzarello, S. Paolini, A. Pasquarello, L. Paulatto, C. Sbraccia, S. Scandolo, G. Sclauzero, A. P. Seitsonen, A. Smogunov, P. Umari, and R. M. Wentzcovitch. Quantum espresso: a modular and open-source software project for quantum simulations of materials. *J. Phys.: Condens. Matt*, 21:395502, 2009.

[11] John P. Perdew, K. Burke, and M. Ernzerhof. Generalized gradient approximation made simple. *Phys. Rev. Lett*, 77:3865, 1996.

[12] S. Grimme. Semiempirical GGA-type density functional constructed with a long-range dispersion correction. *J. Comput. Chem.*, 27:1787, 2006.

[13] I. Zutic, J. Fabian, and S. Das Sarma. Spintronics: fundamentals and applications. *Rev. Mod. Phys.*, 76:323, 2004.

[14] N. F. Mott. The resistance and thermoelectric properties of the transition metals. *Proc. R. Soc.*, 156:368–382, 1936.

[15] M. Julliere. Tunneling between ferromagnetic films. *Phys. Lett. A*, 54:225, 1975.

[16] M.S Liao and S. Scheiner. Electronic structure and bonding in metal phthalocyanines, Metal= Fe, Co, Ni, Cu, Zn, Mg. *J. Chem. Phys.*, 114:9780, 2001.

[17] S. Yim, S. Heutz, and T. S. Jones. Model for the $\alpha \rightarrow \beta_1$ phase transition in phthalocyanine thin films. *J. Appl. Phys.*, 91:3632, 2002.

[18] R. D. Gould. Structural and conduction properties of phthalocyanine films. *Coor. Chem. Rev.*, 156:237, 1996.

[19] A. Calzolari, A. Ferretti, and M. B. Nardelli. Ab-initio correlation effects on the electronic and transport properties of metal(II)-phthalocyanine-based devices. *Nanotechnology*, 18:424013, 2007.

[20] X. Shen, L. Sun, E. Benassi, Z. Shen, X. Zhao, S. Sanvito, and S. Hou. Spin filter effect of manganese phthalocyanine contacted with single-walled carbon nanotube electrodes. *J. Chem. Phys.*, 132:054703, 2010.

[21] S. Heutz, C. Mitra, W. Wu, A. J. Fisher, A. Kerridge, M. Stoneham, A. H. Harker, J. Gardener, H.-H. Tseng, T. S. Jones, C. Renner, and G. Aeppli. Molecular thin films: A new type of magnetic switch. *Adv. Mater.*, 19:3618, 2007.

[22] H. Yamada, T. Shimada, and A. Koma. Preparation and magnetic properties of manganese(II) phthalocyanine thin films. *J. Chem. Phys.*, 108:10256, 1998.

[23] C.G. Barraclough, R. L. Martin, S Mitra, and R. C. Sherwood. Magnetic anisotropy, electronic structure and ferromagnetism in spin s= 3/2 manganese phthalocyanine. *J. Chem. Phys.*, 53:1683, 1970.

[24] M. Witko and K. Hermann. Different addsorbate bingding mechanism of hydrocarbons: theoratical studies of Cu(111)-C_2H_2 and Cu(111)-C_2H_4. *Appl. Catal. A: General*, 172:85, 1998.

[25] H. Ishii, K. Sugiyama, E. Ito, and K. Seki. Energy level alignment and interfacial electronic structures at organic/metal and organic/organic interfaces. *Adv. Mater.*, 11:605, 1999.

[26] A. Michaelides, P. M.-H. Lee, A. Alavi, and D. A. King. Resolution of an ancient surface science anomaly: Work function change induced by N adsorption on W(100). *Phys. Rev. Lett.*, 90:246103, 2003.

[27] P. S. Bagus, D. Kafer, G. Witte, and C. Wöll. Work function changes induced by charged adsorbates: Origin of the polarity asymmetry. *Phys. Rev. Lett.*, 100:126101, 2008.

[28] G. Witte, S. Lukas, P. S. Bagus, and C. Wöll. Vacuum level alignment at organic/metal junctions: cushion effect and the interface dipole. *Appl. Phys. Lett.*, 87:26350, 2005.

[29] L. Romaner, D. Nabok, P. Puschnig, E. Zojer, and C. Ambrosch-Draxl. Theoretical study of PTCDA adsorbed on the coinage metal surfaces, Ag(111), Au(111) and Cu(111). *New J. Phys.*, 11:053010, 2009.

[30] H. B. Akkerman, R. C. G. Naber, B. Jongbloed, P. A. van Hal, P. W. M. Blom, D. M. de Leeuw, and B. de Boer. Electron tunneling through alkanedithiolself-assembled monolayers in large-area molecular junctions. *Proc. Nat. Acd. Sci.*, 104:11161, 2007.

[31] Y. Zhan, E. Holmstrom, R. Lizarraga, O. Eriksson, X. Liu, E. Carlegrim F. Li, S. Stafstrom, and M. Fahlman. Efficient spin injection through exchange coupling at organic semiconductor/ferromagnet heterojunctions. *Adv. Mater.*, 22:1626, 2009.

[32] U. G. E. Perera, H. J. Kulik, V. Iancu, L. G. G. V. Dias da Silva, S. E. Ulloa, N. Marzari, and S.-W. Hla. Spatially extended kondo state in magnetic molecules induced by interfacial charge transfer. *Phys. Rev. Lett.*, 105:106601, 2010.

[33] J. M. de Teresa, A. Barthelemy, A. Fert, J. P. Contour, F. Montaigne, and P. Seneor. Role of metal-oxide interface in determining the spin polarization of magnetic tunnel junctions. *Science*, 286:507, 1999.

[34] I. I. Oleinik, E. Yu. Tsymbal, and D. G. Pettifor. Atomic and electronic sturcture of Co/SrTiO$_3$ /Co magnetic tunnel junctions. *Phys. Rev. B*, 65:020401, 2001.

[35] I. I. Oleinik, E. Yu. Tsymbal, and D. G. Pettifor. Structural and electronic properties of Co/Al$_2$O$_3$/Co magnetic tunnel junction from first principles. *Phys. Rev. B.*, 62:3952, 2000.

[36] W. H. Butler, X.-G. Zhang, T. C. Schulthess, and J. M. MacLaren. Spin-dependent tunneling conductance of Fe | MgO | Fe sandwiches. *Phys. Rev. B*, 63:054416, 2001.

[37] T. S. Santos, J. S. Lee, P. Migdal, I. C. Lekshmi, B. Satpati, and J. S. Moodera. Room temperature tunnel magnetoresistance and spin-polarized tunneling through an organic semiconductor barrier. *Phys. Rev. Lett.*, 98:016601, 2007.

[38] Z. H. Xiong, Di Wu, Z. Valy Vardeny, and Jing Shi. Giant magnetoresistance in organic spin valves. *Nature*, 427:821, 2004.

[39] A. R. Rocha, V. M. G.-Suarez, S. W. Bailey, C. J. Lambert, J. Ferrer, and S. Sanvito. Towards molecular spintronics. *Nat. Mater.*, 4:335, 2005.

[40] I. Biswas, H. Peisert, M. Nagel, M. B. Casu, S. Schuppler, P. Nagel, E. Pellegrin, and T. Chass. Buried interfacial layer of highly oriented molecules in copper phthalocyanine thin films on polycrystalline gold. *J. Chem. Phys.*, 126:174704, 2007.

[41] H. Peisert, T. Schwieger, J. M. Auerhammer, M. Knupfer, M. S. Golden, J. Fink, P. R. Bressler, and M. Mast. Order on disorder: Copper phthalocyanine thin films on technical substrates. *J. Appl. Phys.*, 90:466, 2001.

[42] I. Biswas, H. Peisert, T. Schwieger, D. Dini, M. Hanack, M. Knupfer, T. Schmidt, and T. Chass. Tetra-t-butyl magnesium phthalocyanine on gold: Electronic structure and molecular orientation. *J. Chem. Phys.*, 122:064710, 2005.

[43] H. Peisert, I. Biswas, L. Zhang, M. Knupfer, M. Hanack, D. Dini, M.J. Cook, I. Chambrier, T. Schmidt, D. Batchelor, and T. Chass. Orientation of substituted phthalocyanines on polycrystalline gold: distinguishing between the first layers and thin films. *Chem. Phys. Lett.*, 403:1, 2005.

[44] A. Ruocco, F. Evangelist, A. Attili, M. P. Donzello, M. G. Betti, L. Giovanelli, and R. Gotter. Copper-phthalocyanine ultra thin films grown onto Al(100) surface investigated by synchrotron radiation. *J. Elec. Spec. Relat. Phenom.*, 137:165, 2004.

[45] A. F. Takacs, F. Witt, S. Schmaus, T. Balashov, M. Bowen, E. Beaurepaire, and W. Wulfhekel. Electron transport through single phthalocyanine molecules studied using scanning tunneling microscopy. *Phys. Rev. B*, 78:233404, 2008.

[46] L. Gao, W. Ji, Y. B. Hu, Z. H. Cheng, Z. T. Deng, Q. Liu, N. Jiang, X. Lin, W. Guo, S. X. Du, W. A. Hofer, X. C. Xie, , and H.-J. Gao. Site-specific Kondo effect at ambient temperatures in iron-based molecules. *Phys. Rev. Lett.*, 99:106402, 2007.

[47] N. Papageorgiou, E. Salomon abd T. Angot abd J.-M. Layet, L. Giovanelli, and G. Le Lay. Physics of ultra-thin phthalocyanine films on semiconductors. *Prog. Sur. Sci.*, 77:139, 2005.

[48] C. Stadler, S. Hansen, I. Krger, C. Kumpf, and E. Umbach. Tuning intermolecular interaction in long-range-ordered submonolayer organic films. *Nat. Phys.*, 5:153, 2009.

[49] A. Gerlach, F. Schreiber, S. Sellner, H. Dosch, I. A. Vartanyants, B. C. C. Cowie, T.-L. Lee, and J. Zegenhagen. Adsorption-induced distortion of $F_{16}CuPc$ on Cu(111) and Ag(111): An x-ray standing wave study. *Phys. Rev. B*, 71:205425, 2005.

[50] J. D. Baran, J. A. Larsson, R. A. J. Woolley, Yan Cong, P. J. Moriarty, A. A. Cafolla, K. Schulte, and V. R. Dhanak. Theoretical and experimental comparison of SnPc, PbPc, and CoPc adsorption on Ag(111). *Phys. Rev. B*, 81:075413, 2010.

[51] A. Gerlach, T. Hosokai, S. Duhm, S. Kera, O. T. Hofmann, E. Zojer, J. Zegenhagen, and F. Schreiber. Orientational ordering of nonplanar phthalocyanines on Cu(111): Strength and orientation of the electric dipole moment. *Phys. Rev. Lett.*, 106:156102, 2011.

[52] Z. Hu, B. Li, A. Zhao, J. Yang, and J. G. Hou. Electronic and magnetic properties of metal-phthalocyanines on Au(111) surface: A first-principles study. *J. Phys. Chem. C*, 112:13650, 2008.

[53] B. W. Heinrich, C. Iacovita, T. Brumme, D.-J. Choi, L. Limot, M. V. Rastei, W. A. Hofer, J. Kortus, and J.-P. Bucher. Direct observation of the tunneling channels of a chemisorbed molecule. *J. Phys. Chem. Lett.*, 1:1517, 2010.

[54] A. Zhao, Q. Li, L. Chen, H. Xiang, W. Wang, S. Pan, B. Wang, X. Xiao, J. Yang, J. G. Hou, , and Q. Zhu. Controlling the Kondo effect of an adsorbed magnetic ion through its chemical bonding. *Science*, 309:1542, 2005.

[55] Y.-S. Fu, S.-H. Ji, X. Chen, X.-C. Ma, R. Wu, C.-C. Wang, W. H. Duan, X.-H. Qiu, B. Sun, P. Zhang, J.-F. Jia, and Q.-K. Xue. Manipulating the Kondo resonance through quantum size effects. *Phys. Rev. Lett.*, 99:256601, 2007.

[56] S. Pan, A. Zhao, B. Wang, J. Yang, and J. Hou. Controlling electronic states and transport properties at the level of single molecules. *Adv. Mat.*, 22:1967, 2010.

[57] C. Iacovita, M. V. Rastei, B. W. Heinrich, T. Brumme, J. Kortus, L. Limot, and J. P. Bucher. Visualizing the spin of the individual cobalt-phthalocyanine molecules. *Phys. Rev. Lett.*, 101:116602, 2008.

[58] J. Brede, N. Atodiresei, S. Kuck, P. Lazic, V. Caciuc, Y.Morikawa, G. Hoffmann, S. Blugel, and R. Wiesendanger. Spin-and energy-dependent tunneling through a single molecule with intramolecular spatial resolution. *Phys. Rev. Lett.*, 105:047204, 2010.

[59] S. Javaid, M . Bowen, S. Boukari, L. Joly, J.-B. Beaufrand, X. chen, Y. Dappe, F. Scheurer, J.-P. Kappler, J. Arabski, W. Wulfhekel, M. Alouani, and E. Beaurepaire. Impact on interface spin polarization of molecular bonding to metallic surfaces. *Phys. Rev. Lett.*, 105:077201, 2010.

[60] R. M. Martin. Electronic structure: Basic theory and practical methods. *Cambridge press*, 2004.

[61] P. Hohenberg and W. Kohn. Inhomogeneous electron gas. *Phys. Rev*, 136:864, 1964.

[62] W. Kohn and L. J. Sham. Self-consistent equations including exchange and correlation effects. *Phys. Rev*, 140:1133, 1965.

[63] R. O. Jones and O. Gunnarsson. The density functional formalism, its applications and prospects. *Rev. Mod. Phys.*, 61:689, 1989.

[64] K. Burke. The ABC of DFT. *http://chem.ps.uci.edu/ kieron/dft/book/*.

[65] J. Perdew and S. Kurth. Density functionals for non relativistic coulomb systems. *Proceedings of the Tenth Chris Engelbrecht Summer School in Theoretical Physics, Springer lecture notes in physics*, 500:8, 1998.

[66] M. C. Payne, M. P. Teter, D. C. Allan, T. A. Arias, and J. D. Joannopoulus. Iterative minimization techniques for ab-initio total energy calculations: molecular dynamics and conjugate gradients. *Phys. Rev. Lett*, 46:1045, 1992.

[67] D. M. Ceperley and B. J. Alder. Ground state of the electron gas by a stochastic method. *Phys. Rev. Lett*, 45:566, 1980.

[68] J. P. Perdew and A. Zunger. Self-interaction correction to density-functional approximations for many-electron systems. *Phys. Rev. B*, 23:5048, 1981.

[69] T. Thonhauser, V. R. Cooper, S. Li, A. Puzder, P. Hyldgaard, and D. C. Langreth. Van der Waals density functional: Self-consistent potential and the nature of the van der Waals bond. *Phys. Rev. B*, 76:125112, 2007.

[70] M. Cococcioni and S. de Gironcoli. Linear response approach to the calculation of the effective interaction parameters in the LDA+U method. *Phys. Rev. B*, 71:035105, 2005.

[71] V. I. Anisimov, J. Zaanen, and O. K. Anderson. Band theory and mott insulators: Hubbard u instead of stoner i. *Phys. Rev. B*, 44:943, 1991.

[72] D. A. Scherlis, M. Cococcioni, P. Sit, and N. Marzari. Simulation of heme using DFT+U: A step toward accurate spin-state energetics. *J. Phys. Chem. B*, 111:7384, 2007.

[73] S. Lebégue, S. Pillet, and J. G. Angyan. Modeling spin-crossover compounds by periodic DFT+U approach. *Phys. Rev. B*, 78:024433, 2008.

[74] H. J. Monkhorst and J. D. Pack. Special points for brillouin-zone integrations. *Phys. Rev. B*, 13:5188, 1976.

[75] L. Kleinman and D. M. Bylander. Efficacious form for model pseudopotentials. *Phys. Rev. Lett.*, 48:1425, 1982.

[76] D. R. Hamann, M. Schluter, and C. Chiang. Norm-conserving pseudopotentials. *Phys. Rev. Lett.*, 43:1494, 1979.

[77] D. Vanderbilt. Soft self-consistent pseudopotentials in a generalized eigenvalue formalism. *Phys. Rev. B*, 41:7892, 1990.

[78] J. F. Dobson, J. Wang, B. P. Dinte, K. Mclennan, and H. M. Le. Soft cohesive forces. *Int. J. of Quan. Chem.*, 101:579, 2005.

[79] H. Rydberg, M. Dion, N. Jacobson, E. Schroder, P. Hyldgaard, S. I. Simak, D. C. Langreth, and B. I. Lundqvist. Van der Waals density functional for layered structures. *Phys. Rev. Lett.*, 91:126402, 2003.

[80] E. R. Johnson, I. D. Mackie, and G. A. DiLabio. Dispersion interactions in density-functional theory. *J. Phys. Org. Chem.*, 22:1127, 2009.

[81] S. Grimme, J. Antony, T. Schwabe, and C. M.-Lichtenfeld. Density functional theory with dispersion corrections for supramolecular structures, aggregates, and complexes of (bio)organic molecules.

[82] M. Dion, H. Rydberg, E. Schroder, D. C. Langreth, and B. I. Lundqvist. Van der Waals density functional for general geometries. *Phys. Rev. Lett.*, 92:246401, 2004.

[83] S. Grimme, J. Antony, S. Ehrlich, and H. Krieg. A consistent and accurate ab initio parametrization of density functional dispersion correction (DFT-D) for the 94 elements H-Pu. *J. Chem. Phys.*, 132:154104, 2010.

[84] S. Grimme. Accurate description of van der Waals complexes by density functional theory including empirical corrections. *J. Comput. Chem.*, 25:1463, 2004.

[85] V. Barone, M. Casarin, D. Forrer, M. Pavone, M. Sambi, and A. Vittadini. Role and effective treatment of dispersive forces in materials: Polyethylene and graphite crystals as test cases. *J Comput. Chem.*, 30:934, 2009.

[86] S. Peljhan and A. Kokalj. Adsorption of chlorine on Cu(111): A density-functional theory study. *J. Phys. Chem. C*, 113:14363, 2009.

[87] A. Kokalj, A. D. Corso, S. de Gironcoli, and S. Baroni. The interaction of ethylene with perfect and defective Ag(001) surfaces. *J. Phys. Chem. B*, 106:9839, 2002.

[88] T. Funk, A. Deb, S. J. George, H. Wang, and S. P. Cramer. X-ray magnetic circular dichroisma high energy probe of magnetic properties. *Coor. Chem. Rev.*, 249:3, 2005.

[89] E. Beaurepaire, H. Bulou, F. Sheurer, and J. P. Kappler. Magnetism: A synchrotron radiation approach. *Springer*, 2006.

[90] B. T. Thole, P. Carra, F. Sette, and G. van der Laan. X-ray circular dichroism as a probe of orbital magnetization. *Phys. Rev. Lett.*, 68:1943, 1992.

[91] M. Newville. Fundamentals of XAFS. *http://xafs.org/Tutorials*, 2004.

[92] F. De Groot. Multiplet effects in x-ray spectroscopy. *Coor. Chem. Rev.*, 249:31, 2005.

[93] J. J. Rehr and R. C. Albers. Theoretical approaches to x-ray absorption fine structure. *Rev. Mod. Phys.*, 72:621, 2000.

[94] F. De Groot. High-resolution x-ray emission and x-ray absorption spectroscopy. *Chem. Rev.*, 101:1779, 2001.

[95] J. Stöhr. NEXAFS spectroscopy. *Springer*, 1992.

[96] D. C. Koningsberger and R. Prins. X-ray absorption: Principles, applications, techniques of EXAFS, SEXAFS and XANES. *Wiley-Interscience*, 1988.

[97] J. Stöhr. NEXAFS spectroscopy. *http://ssrl.slac.stanford.edu/stohr/.*

[98] J. Stöhr and H. C. Siegman. Magnetism: From fundamentals to nanoscale dynamics. *Springer*, 2006.

[99] J. Stöhr. Exploring the microscopic origin of magnetic anisotropies with x-ray magnetic circular dichroism (XMCD) spectroscopy. *J. Mag. and Magnet. Mat.*, 200:470, 1999.

[100] E. Beaurepaire, F. Sheurer, G. Krill, and J. P. Kappler. Magnetism and synchrotron radiation. *Springer*, 2001.

[101] J. P. Johnson. Spin-polarized photoemission. *Rep. Prog. Phys.*, 60:1217, 1997.

[102] A. Damascelli, Z. Hussain, and Z. X. Shen. Angle-resolved photoemission studies of the cuprate superconductors. *Rev. Mod. Phys.*, 75:473, 2003.

[103] F. Reinert and S. Hüfner. Photoemission spectroscopyfrom early days to recent applications. *New J. Phys.*, 7:97, 2007.

[104] B. W. Batterman. The effect of dynamical diffraction in x-ray flourescence scattering. *Phys. Rev.*, 133:A759, 1964.

[105] D. P. Woodruff. Normal incidence x-ray standing wave determination of adsorbate strutures. *Prof. Sur. Sci.*, 57:1, 1998.

[106] J. Zegenhagen. Surface structure determination with x-ray standing waves. *Sur. Sci. Rep.*, 18:199, 1993.

[107] S. Thieß. Interface structure and electronic properties of $SrTiO_3$ and $YBa_2Cu_3O_7$ crystals and thin films. *PhD thesis, Univeristy of Hamburg*, 2007.

[108] P. Fenter, M. Rivers, N. C. Sturchio, and S. Sutton. X-ray standing wave studies of minerals and mineral surfaces: Principles and applications. *Reviews in Mineralogy and Geochemistry*, 49:221–266, 2002.

[109] D. P. Woodruff, D. L. Seymour, C. F. McConville, C. E. Riley, M. D. Crapper, N. P. Prince, and R. G. Jones. Simple x-ray standing-wave technique and its application to the investigation of the Cu(111) ($\sqrt{3} \times \sqrt{3}$)R30°- Cl structure. *Phys.Rev.Lett.*, 58:1460, 1987.

[110] DARE software is developed by J. Zegenhagen, ESRF, France.

[111] H. Vázquez, R. Oszwaldowski, P. Pou, J. Ortega, R. Prez, F. Flores, and A. Kahn. Dipole formation at metal/PTCDA interfaces: Role of the charge neutrality level. *Euro. Phys. Lett.*, 65:802, 2004.

[112] We have performed the XAS experiments by tilting the sample such that the surface normal is at 50° w.r.t. the photon beam. The polarization of the photon beam can vary continuously from horizontal (0° from plane, i.e., in the sample plane) to vertical (50° from the sample plane). The out of plane sensitivity is acheived by performing the XAS with polarization at 50° from the sample plane. The spectra thus obtained also have some contribution coming from N 1s $\rightarrow \sigma^*$ transitions. This contribution is removed by subtracting the N 1s $\rightarrow \sigma^*$ XAS spectra acquired with polarization at 0°, from those acquired at 50°.

[113] S. Schmaus, A. Bagrets, Y. Nahas, T. K. Yamada, A. Bork, M. Bowen, E. Beau-repaire, F. Evers, and W. Wulfhekel. Giant magnetoresistance through a single molecule. *Nat. Nanotech.*, 6:185, 2011.

[114] G. Heimel, L. Romaner, J.-L. Bredas, and E. Zojer. Interface energetics and level alignment at covalent metal-molecule junctions: π-conjugated thiols on gold. *Phys. Rev. Lett.*, 196806:96, 2006.

[115] M. Weinelt. Time-resolved two-photon photoemission from metal surfaces. *J. Phys.: Condens. Matter*, 14:R1099, 2002.

[116] M. Aeschlimann, M. Bauer, S. Pawlik, W. Weber, R. Burgermeister, D. Oberli, and H. C. Siegmann. Ultrafast spin-dependent electron dynamics in fcc Co. *Phys. Rev. Lett.*, 79:5158, 1997.

[117] P. S. Bagus, V. Staemmler, and C. Wöll. Exchangelike effects for closed-shell adsorbates: Interface dipole and work function. *Phys. Rev. Lett.*, 89:096104, 2003.

[118] T. U. Kampen. Electronic structure of organic interfaces a case study on perylene derivatives. *App. Phys. A*, 82:457, 2006.

[119] J. J. Yeh and I. Lindau. Atomic subshell photoionization cross sections and asymmetry parameters: $1 \leq Z \leq 103$. *Atomic data and nuclear tables*, 113:1, 1985.

[120] C. Sorg, N. Ponpandian, M. Bernien, K. Baberschke, H. Wende, and R. Q. Wu. Induced magnetism of oxygen in surfactant-grown Fe, Co, and Ni monolayers. *Phys. Rev. B*, 73:064409, 2006.

[121] Due to the optics pass energy spectrum, we observed an undesired absorption due to Co. This contribution was removed to calculate the XMCD signal of N.

[122] N. Atodiresei, J. Brede, P. Lazic, V. Caciuc, G. Hoffmann, R. Wiesendanger, and S. Blugel. Design of the local spin polarization at the organic-ferromagnetic interface. *Phys. Rev. Lett.*, 105:066601, 2010.